HIERARCHICAL CONTROL AND STABILITY ANALYSIS OF AC MICROGRIDS WITH VIRTUAL-OSCILLATOR CONTROLLED SOURCES

by

Mohammad Mahdavyfakhr

B.Sc. Shahid Beheshti University, 2014

M.Sc, Shahid Beheshti University, 2016

A THESIS SUBMITTED IN PARTIAL FULFILLMENT OF

THE REQUIREMENTS FOR THE DEGREE OF

MASTER OF APPLIED SCIENCE

in

THE FACULTY OF GRADUATE AND POSTDOCTORAL STUDIES

(ELECTRICAL AND COMPUTER ENGINEERING)

THE UNIVERSITY OF BRITISH COLUMBIA

(Vancouver)

October 2020

The following individuals certify that they have read, and recommend to the Faculty of Graduate and Postdoctoral Studies for acceptance, the thesis entitled:

Hierarchical Control and Stability Analysis of AC Microgrids with Virtual-oscillator controlled Sources

submitted by Mohammad Mahdavyfakhr in partial fulfillment of the requirements for

the degree of Master of Applied Science

in Electrical and Computer Engineering

Examining Committee:

Dr. Juri Jatskevich, Professor, Department of Electrical and Computer Engineering, UBC

Supervisor

Dr. Ryozo Nagamune, Associate Professor, Department of Mechanical Engineering, UBC

Supervisory Committee Member

Dr. Y. Christine Chen, Assistant Professor, Department of Electrical and Computer Engineering, UBC

Additional Examiner

Abstract

Microgrids are envisioned as building blocks of evolving power systems, where they have a potential for improved resiliency, higher energy efficiency, and integration of renewable resources on a smaller scale. At the same time, the increased complexity of integrating new and distributed energy resources (DERs) presents several control-related challenges for the safe and optimal operation of AC microgrids. The new challenges also include the increasing number of power-electronically interfaced loads and sources that behave as constant power loads (CPLs) or constant power sources (CPS), and are known to have destabilizing effect on the system. All of this necessitates research for better analysis tools, control schemes, and technological solutions that ensure proper coordination of all components within a microgrid. To improve the operation of envisioned AC microgrids, this thesis proposes an economical hierarchical control scheme that incorporates control levels with different dynamics. This scheme not only ensures proper voltage and frequency regulation and power sharing among different resources, but it also minimizes the operational costs considering the price of available energy resources. At the next level, this thesis investigates dynamic interactions between the DERs and CPLs within a microgrid. A recently proposed virtual oscillator controlled source (VOS) is investigated and compared against the traditional/generic control used with DERs. It is demonstrated that impedance-based analysis can accurately predict the instability and sideband oscillations resulted from the interaction with the CPL, as well as used to tune the controllers. It is also shown that while the VOS has a faster dynamic response, its stability boundaries may actually be smaller. It is envisioned that the presented research will contribute to the development of AC microgrids with high penetration of renewables, energy storage systems, as well as various types of electronic loads.

Lay Summary

Microgrids are envisioned as building blocks of evolving power systems, where they have a potential for improved resiliency, higher energy efficiency, and integration of renewable resources. At the same time, the increased complexity also presents some new challenges. To improve the operation of envisioned AC microgrids, this thesis proposes an economical hierarchical control scheme that ensures voltage/frequency regulation and power sharing among different resources, and also minimizes the operational costs. This thesis also investigates interactions between various energy sources and fast power electronic loads. The developed methodology is shown to accurately predict the instability and oscillations that may appear in microgrids, as well as proposes a better way for tuning controllers. It is envisioned that the presented research will contribute to the development of AC microgrids with high penetration of renewables, energy storage systems, as well as various types of electronic loads.

Preface

I am writing this preface to confirm that I am the main contributor and author of this thesis. I am responsible for formulating mathematical models, implementing and running computer simulations, analyzing approaches and solutions, verifying findings, as well as writing papers that came out of my thesis. Some content of this thesis has been published, some are under review. My supervisor, Dr. Juri Jatskevich, has provided constructive feedback and comments throughout my studies, and his supervision has contributed to my papers and the thesis. The co-authors of my publications, Dr. Navid Amiri, Dr. Seyyedmilad Ebrahimi, and Mr. H. Lin have also helped me revising the manuscripts of my papers and provided constructive feedback and comments. It should be mention that

1- Chapter **2** is based on the following published paper:

   M. Mahdavyfakhr, S. Ebrahimi, H. Lin and J. Jatskevich, "An Effective Economical Hierarchical Control Scheme for Low-Voltage AC Microgrids," 2019 *IEEE 10th Annual Information Technology, Electronics and Mobile Communication Conference* (IEMCON), Vancouver, BC, Canada, 2019, pp. 0255-0261.

2- Chapter **3**, **4**, **5** are based on the following paper.

   M. Mahdavyfakhr, J.Jatskevich, and H. Lin, "Stability Analysis of AC Microgrids with Virtual-Oscillator-Controlled Sources and Constant Power Loads," (Under review) submitted on Sep. 30, 2020.

Table of Contents

List of Tables

List of Figures

List of Abbreviations

AC	Alternating Current
CPL	Constant Power Load
CPS	Constant Power Source
DC	Direct Current
DER	Distributed Energy Resources
DL	Distributed Loads
ESS	Energy Storage Systems
EV	Electric Vehicles
GCS	Generic-Controller Source
GHG	Green House Gases
PLL	Phase-locked Loop
RER	Renewable Energy Resources
SCR	Short Circuit Ratio
VOS	Virtual-oscillator Controlled Source

Acknowledgements

I am very grateful to my supervisor Dr. Juri Jatskevich who has provided me unique research experience in UBC. His constructive comments have improved my papers and thesis significantly. His advice is always invaluable to me, my academic career, and professional development. I highly appreciate my supervisor's consideration of the limitation posed by unprecedented pandemic situation. I am also very thankful to thank Dr. Y. Christine Chen and Dr. Ryozo Nagamune for accepting to participate in my thesis defense examination during these hardship times of virtual only meetings, and for all their constructive comments and questions that contributed to deepening my understanding. Special thanks to our research group members Dr. Navid Amiri, Dr. Milad Ebrahimi, and Mr. H. Lin for sharing research ideas and for proof reading my papers.

Dedication

I dedicate wholeheartedly this work to my *beloved mother*, *father*, and *family* whose support and passion helped me to stand strong in challenging situations. I also dedicate this to my *gorgeous mate*.

Chapter 1: Introduction

Global warming and many natural disasters around the world are attributed to the effects of greenhouse gases (GHG) emission, and they pose extreme financial stress on countries' economies. Energy sector is one of the key contributors to GHG emission [1]. To reduce environmental impact, many countries are investing in the development of new and clean energy technologies, including hybrid and electric vehicles (EV), energy storage systems (ESS), integration of renewable energy resources (RER), etc. Aside from these technologies, the microgrids have emerged as additional building blocks that can co-exist with the conventional large-scale power systems.

Microgrids are small-scale power systems that may typically include components such as distributed energy resources (DER), distributed loads (DL), and ESS. Microgrids can be connected to make a cluster of microgrids, or they can be integrated into a large power grid. In case of emergencies, they may be disconnected from power grids to continue operation in an islanded mode. In some cases, microgrids can provide higher reliability of service, a better quality of power supply, and higher efficiency of energy utilization. Unlike conventional power systems, microgrids often possess the following properties:

I) Connecting lines have a high resistive characteristic (higher ratio of R/X),

II) The system capacity is limited by the capacity of DERs,

III) The fault current is low [i.e. low, short circuit ratio (SCR)],

IV) Loads can be highly unbalanced,

V) The system inertia is low,

VI) Energy supply is prone to higher uncertainties, which is due to the intermittent nature of RER [2], [3].

These features pose additional challenges for the operation of microgrids, and therefore represent active research areas.

1.1 Operational Challenges

Since DERs have limited capacities, it is a common approach to share loads among multiple DERs. Power-sharing among DERs can be generally categorized into centralized and decentralized approaches [4]. Centralized approaches as master-slave [5], [6], or average current sharing [7], [8] have a good power-sharing accuracy; however, since they are dependent on communication links, they are not highly reliable [4].

Decentralized power-sharing approaches [9]–[11] do not require communication links, and hence, benefit from higher reliability as well as plug-and-play feature. These approaches tend to mimic the behavior of synchronous generators by frequency-dependent active power and voltage-dependent reactive power characteristics. These approaches, however, can suffer from poor reactive power-sharing or decrease stability margins of microgrids [12]–[14].

Another problem in microgrids is related to current and voltage harmonics. Non-linear loads in microgrids produce current harmonics and distort the terminal voltage of DERs [15]. The discussed power-sharing approaches are ineffective to address non-linear load sharing and voltage harmonics compensation [15]. One solution to this problem is to add different control loops in parallel, with the fundamental power-sharing loop droop-type control [16]. Also, virtual impedances at the terminal of DERs can be synthesized at different frequencies to impact the distribution of harmonics among DERs [17], [18].

Synchronization of DERs in microgrids is another challenge that can be dealt with by different approaches. The first type of approaches is based on the phase-locked loop (PLL) scheme. With these schemes, the operating frequency of microgrids can be recognized and used to determine the control reference of DERs. The synchronous reference frame PLL (SRF-PLL), is the basic PLL scheme, and other PLL-derived schemes with improved characteristics can also be used for synchronization [19], [20].

Recently, a group of synchronization approaches based on virtual oscillators has been proposed. In these approaches, a non-linear circuit is used to produce modulation signals [21]–[23]. The circuit is implemented on a digital controller and it includes a resonant tank as well as a non-linear dependent voltage/current source. It has been shown that if the parameters are properly designed, the steady-state voltage can follow a pure sine wave [24]. These approaches can also be modified to mimic droop characteristics and provide power-sharing among multiple DERs [25].

Apart from synchronization and power-sharing issues, the microgrids' voltage and frequency should always be regulated. For this purpose, hierarchical control schemes have been developed. A hierarchical control scheme can incorporate different control levels. In the first stage, inner control loops with feedback and/or feedforward are designed to control currents and/or voltages of DERs [26]. This control level ensures that each DER demonstrates a stable and desirable fast dynamic behavior and characteristic.

Next, the so-called primary control is designed to satisfy the power-sharing requirements among the DERs [2]. For instance, active-power/frequency and reactive-power/voltage droop characteristics [27], [28] for AC microgrids are aimed to provide proper power-sharing among DERs and storages at the primary control level. The so-called secondary control level is responsible for maintaining the voltage magnitude and frequency of AC microgrid to their nominal values, which is achieved by adjusting the reference signals of the DERs [2]. Finally, the tertiary control level manages the desired power flow from/to microgrids during slower time periods.

Stability of microgrids is another topic that is receiving noticeable attention in the literature [3], [29], [30]. Microgrids can demonstrate different stability-related problems in islanded mode rather than in grid-connected operation. This is because in grid-connected mode, the frequency and voltage are imposed by the grid, and stability issues can only be triggered by a failure of individual components. In islanded mode, more stability issues can occur since the voltage and frequency regulation are performed by limited resources within microgrids [3]. Stability issues in islanded microgrids can be categorized, based on the cause, in two general groups: power-balance stability issues; and control stability issues [3].

Power-balance stability issues can happen when the balance of power consumption and generation is lost. This is a critical problem in microgrids since a high share of intermittent RES can be connected to microgrids, and microgrids inertia is typically very low compared to conventional power systems. Therefore, in case of disturbances, for example, loss of a generation unit or a load, large voltage and frequency oscillations can be observed, sensitive loads can perform volunteer tripping, and further exacerbate the power imbalance in the system [3].

Control stability issues refer to stability problems which can be addressed by modifying the control systems of the power electronic converters in the microgrid [3]. These issues are also known as harmonic instability and can lead to sustained or increasing oscillations in a wide range of frequencies, from low sub-synchronous frequencies all the way to the switching frequencies [31], [32]. Harmonic instability can happen due to various reasons. It has been shown that power electronic converters can interact with passive filters [33], [34]. Harmonic instability can also be triggered in parallel operation of power electronic converters with filters. The interaction can happen in high-frequency and often result from fast control loops of power electronic converters [35], [29]. Moreover, the time delay produced by modulation and digital sampling process can also present negative damping in high frequency and consequently destabilize the power electronics [31], [36].

The harmonic instability in low frequency can be attributed to low bandwidth control loops of the droop power-sharing approach [37], [13], dc-link voltage control [38], [39], and phase-lock loop (PLL) synchronization [40], [41]. It also has been shown that constant power loads possess negative incremental input impedance, and thus reducing the stability margin in microgrids [42], [43].

The harmonic instability is often pronounced as a pair of coupled frequencies, also known as sideband oscillations. The sideband oscillations can be around the fundamental frequency of the microgrid [31] ($\mathrm{f_1} \pm \mathrm{f_b}$), which are often caused by non-symmetric control loops such as the PLL control loops [41], or the DC-link voltage control loops. It should also be mentioned that the frequency component $\mathrm{f_1} - \mathrm{f_b}$ is sub-synchronous when the fundamental frequency $\mathrm{f_1}$ is greater than the band frequency f_b, and it would be in the negative sequence when $f_1 < f_b$. The sideband oscillations can also happen around the switching frequency due to modulation and sampling process [31], [44].

Stability analysis of microgrids can be performed using two general approaches. The first approach is to develop a state-space model of a microgrid in time-domain and then analyze the stability based on the system's eigenvalues. This approach is not suitable for systems with a large number of states, which makes it very difficult to trace a specific eigenvalue to a specific microgrid component and its controller parameters. The second approach is based on the impedance as seen from the terminals of a component. The impedances of components are expressed in frequency-domain transfer functions, and the stability is assessed by analyzing the equivalent impedance of the system. This approach has the benefit of scalability and reduced computation effort [31], and is widely used to analyze the stability of power-electronic-based systems [20], [30], [45], [46].

1.2 Thesis Objectives

1.2.1 Economical Hierarchical Control Scheme for Low-Voltage AC Microgrids

Several hierarchical control schemes [26], [47] have been proposed in the literature with different objectives. In [26], a three-layer control scheme is presented to endow smartness and flexibility of microgrids. Another approach is proposed in [47] that can provide robust microgrid operation and smooth transition between islanded and grid-connected operation modes. In [12], [48]–[50] hierarchical control schemes, which can improve the reliability and performance of microgrids, have been discussed. One key aspect of microgrids which has not received adequate attention is the fact that microgrids should supply loads with minimum operation costs so that the revenue is maximized. This aspect has not been fully considered in prior hierarchical control schemes. Therefore, in Chapter 2, a hierarchical control scheme is proposed that can provide both reliable and economical operation of AC microgrids.

1.2.2 Stability Analysis with Constant Power Loads/Sources

Constant power loads/sources (CPL/CPS) demonstrate negative incremental impedance characteristics at their terminals. This characteristic can decrease damping in AC microgrids and in the worst case they can be destabilized [42]. Different studies are performed to assess the destabilizing effect of CPLs [51]–[54]. The negative impedance characteristic of CPLs has also been observed in automotive power systems [51], wherein the design criteria for the control systems of other power electronic converter has been investigated. In [53], it is shown that the low-frequency mode of microgrids can be attributed to voltage controllers of constant power loads.

The CPLs dynamic characteristics have been studied based on impedances in *dq* frame with a modified Nyquist stability criterion [54]. It has been shown that if the bandwidth of connected power electronic converters decreases, the CPL can interact with converters and the combined system can be destabilized. More studies, however, are needed to diagnose and characterize the side-band oscillation in CPL/CPS-connected systems. In particular, the effects of power consumption/generation of CPLs/CPSs on the stability of interconnected systems represents a further challenge. Therefore, Chapter 3, investigates the CPL/CPS-connected systems and the effect of power consumption/generation on the stability, and reveals that the side-band oscillations can occur.

1.2.3 Dynamic Characteristic of Virtual Oscillator-Based Control Schemes

The virtual-oscillator (VO) based control schemes have been recently receiving great attention in the research literature. These control schemes provide promising features such as: a) fast system synchronization; b) good voltage regulation; c) droop-type power-sharing among multiple DERs; and d) improved resiliency during disturbances [23], [24]. The dynamic characteristics of VO-based control schemes, however, have not been sufficiently investigated under a wide range of possible electronic loads. More specifically, it would be of significant practical significance to assess their dynamic behavior when such sources are connecting to the CPLs. In this regard, Chapter 4 investigates the VO-based control scheme of a source and its dynamic characteristics while feeding AC microgrid with CPL.

1.2.4 Dynamic Behavior of CPL/CPS when Connected to Different Energy Resources

The CPLs/CPSs can be connected to different types of DERs and their dynamic characteristics can be different in each case, which also has not been sufficiently analyzed in the previous literature. Chapter 5 presents a comparison of CPL/CPS dynamic characteristics when connected to different types of sources and finally, and confirms that the sideband oscillations and instability can be predicted using the impedance-based methods.

Chapter 2: Hierarchical Control of Low-Voltage AC Microgrids Considering Economical Benefits

In this chapter, a hierarchical control scheme is proposed that can provide both reliable and economical operation of AC microgrids. To realize this control scheme, a representative AC microgrid, which includes DERs and distributed loads, is considered. The power electronic circuits of the DERs are designed based on specified criteria and then modelled based on their structure. Using the obtained models, a multi-loop control scheme is developed for each DER. Then, the principles of power-sharing algorithm among DERs are discussed, and the related control loops are designed. Next, the secondary and tertiary levels of the hierarchical control scheme are presented. It is then demonstrated how the proposed control scheme can provide economical operation of the microgrid, which is verified by simulation results. It should be noted that since the focus of this chapter is on the control scheme of distributed energy resources, the loads are modeled as pure impedances. In fact, the loads are not modeled as constant power loads since they can interact with distributed energy resources and they can destabilize the AC microgrid. The instability resulted from the interaction of constant power loads and distributed energy resources will be studied in the following chapters.

2.1 AC Microgrid

2.1.1 Structure and Modeling

The considered structure of a representative AC microgrid is shown in Figure 2-1**.** The AC microgrid is a low-voltage three-phase distribution system. The AC microgrid can work in either grid-connected or islanded mode. It has three buses: bus_1, bus_3, and bus_2. The loads and DERs are connected to each bus. To satisfy the voltage and frequency regulation requirements, the DERs are connected to the grid with power electronic converters. Since the *LLC* filters can better attenuate the injected harmonics, compared to just *L* and *LC* filters, the power converters are equipped with the *LLC* filters. The DER_1 is connected to an energy storage system, the DER_2 is connected to photovoltaic panels, and the DER_3 is connected to a DC microgrid. With the help of DER_3, the power can either be absorbed from or injected to the DC microgrid.

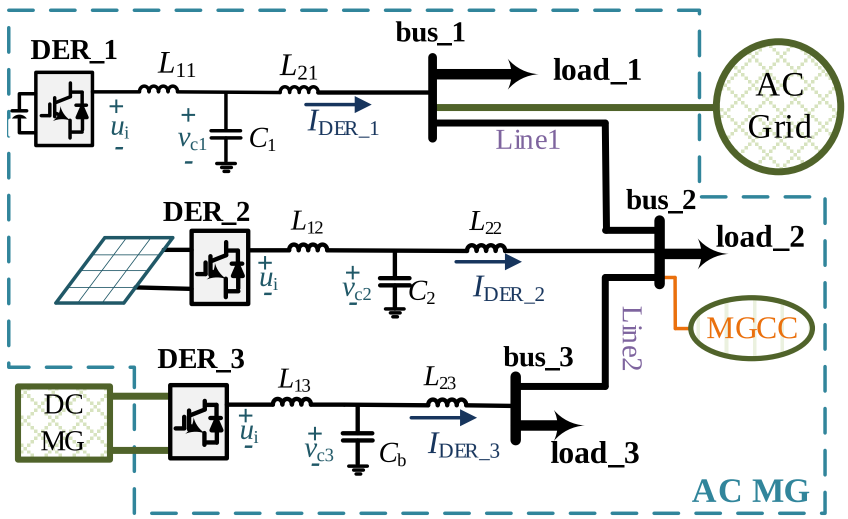

Figure 2-1 Simplified diagram depicting the considered AC microgrid with three DERs.

Different power electronic converters can be utilized for integrating DERs into power grids [55], [56]. In this chapter, for simplicity, three-phase conventional two-level inverters are used to connect DERs to the AC microgrid. The next step is to design *LLC* filters which are responsible for mitigating harmonics produced by the three-phase inverters. Several approaches can be adopted for designing *LLC* filters [57], [58]. This paper uses the technique described in [57] which is a design approach based on current ripple, filter size, switching ripple attenuation, as well as passive resonance damping.

2.1.2 Small-Signal Modeling of DERs

In this subsection small-signal models of DERs are derived and the obtained models are used in the following section to design a hierarchical control system. Assuming that the modulated voltage of an inverter can be modeled by a sinusoidal voltage source, the equivalent circuit of DERs can be represented as Figure 2-2. The small-signal transfer function of inverter side current and capacitor voltage to modulation index *m* can be obtained by applying KVL principle in Figure 2-2 as:

$$G_{\mathrm{ui}} = \frac{\hat{i}_{\mathrm{L1}}}{\hat{m}V_{\mathrm{dc}}} = \frac{Z_{\mathrm{c}} + Z_{\mathrm{Load}} + Z_{\mathrm{L2}}}{(Z_{\mathrm{L2}} + Z_{\mathrm{Load}})(Z_{\mathrm{c}} + Z_{\mathrm{L1}}) + Z_{\mathrm{L1}}Z_{\mathrm{c}}}, \tag{2.1}$$

$$G_{\mathrm{vc}} = \frac{\hat{v}_{\mathrm{C}}}{\hat{m}V_{\mathrm{dc}}} = \frac{Z_{\mathrm{c}}(Z_{\mathrm{Load}} + Z_{\mathrm{L2}})}{(Z_{\mathrm{L2}} + Z_{\mathrm{Load}})(Z_{\mathrm{c}} + Z_{\mathrm{L1}}) + Z_{\mathrm{L1}}Z_{c}}, \tag{2.2}$$

where, Z_{L1}, Z_{L2}, Z_{C} and Z_{Load}, in (2.1) and (2.2) are impedance of inverter side inductor, grid side inductor, capacitor and load, respectively.

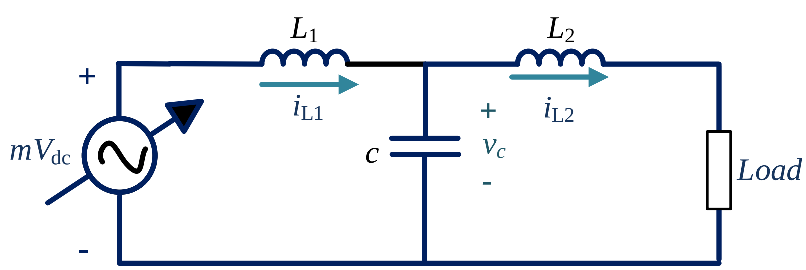

Figure 2-2 Equivalent circuits of DERs with LLC filter.

2.2 Hierarchical Control Scheme

The hierarchical control scheme has four coordinated control levels and each level is dependent on lower level control systems. Hence, this control scheme will be discussed from the lowest level (i.e., zero level control) to the highest level (i.e., tertiary level control).

2.2.1 Zero Level Control

In this part, the zero level control scheme is designed to properly regulate the currents and/or voltages of DERs. The zero level control scheme for DER_1 is shown in Figure 2-3. Since the AC microgrid should operate in both grid-connected and islanded modes, the designed scheme has two control loops. When the AC microgrid is operating in the islanded mode, DER_1 operates in voltage-controlled mode, and the selector switch in Figure 2-3 is connected to position 2. In this switch position, the reference of the inner current loop is determined by the outer voltage control loop. When the AC microgrid is operating in grid-connected mode, the DER_1 is working in current-controlled mode and the selector switch is connected to position 1. In this switch position, the reference of the inner loop is determined by the reference value of the active and reactive power of the generator unit.

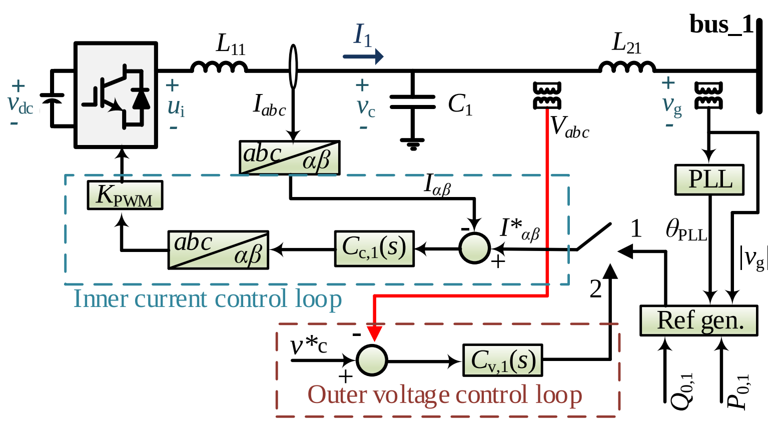

Figure 2-3 Zero level control scheme for DER_1.

The inner current control loop is responsible for regulating the inverter side current I_1. The controller for the inner current loop $C_{c,1}(s)$ should be designed in a way that the inner loop gain defined by (2.3) should have a positive phase margin. Since in current-controlled mode DER_1 should be synchronized with the main grid, the control scheme is equipped with a PLL unit. After designing the inner control loops, the outer voltage control loop can be designed. The controller of the outer loop, $C_{v,1}(s)$ should be designed in a way that the open-loop gain of the outer loop defined by (2.5) should have a positive phase margin. This control scheme can be implemented in dq or $\alpha\beta$ frames. Here, the control scheme is implemented in $\alpha\beta$ frame.

$$T_{\mathrm{si}} = G_{\mathrm{ui}} C_{\mathrm{c},1} \tag{2.3}$$

$$G_{\mathrm{uv}} = \frac{T_{\mathrm{si}}}{1+T_{\mathrm{si}}} G_{\mathrm{vc}} \tag{2.4}$$

$$T_{\mathrm{sv}} = G_{\mathrm{uv}} \times C_{\mathrm{v},1} \tag{2.5}$$

The control scheme for DER_2 is shown in Figure 2-4. As mentioned earlier, DER_2 is connected to photovoltaic panels. Since photovoltaic panels are non-dispatchable resources and it is essential to regulate the DC link voltage of the inverter, DER_2 can only operate in current-controlled mode. The controller $C_{c,2}(s)$ can be designed in the same way as the inner current controller of DER_1.

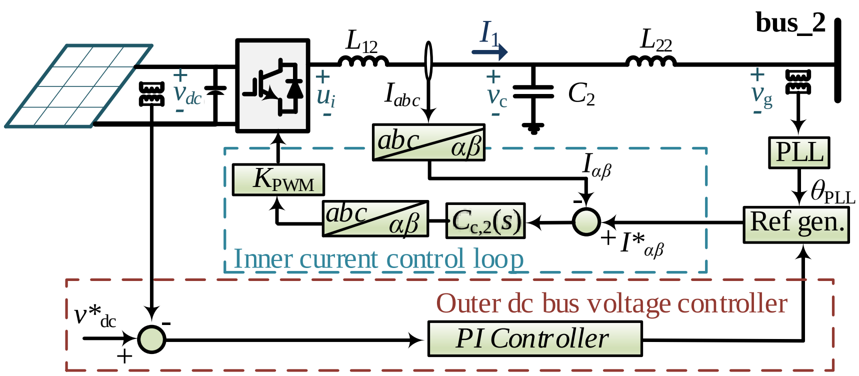

Figure 2-4 Zero level control scheme for DER_2.

The control scheme for DER_3 is shown in Figure 2-5, which is similar to the control scheme of the DER_1. As mentioned earlier, the DER_3 is connected to a DC microgrid and it can either absorb or inject power to the DC microgrid. If power is injected into the DC microgrid, the DER_3 acts as a source and it can regulate the voltage of DC microgrid. If DER_3 absorbs power from DC microgrid, it acts as a load there. The selector switch in Figure 2-5 is in position 2 when the AC microgrid is operating in an islanded mode, and it is in the other position 1 when the AC microgrid is connected to the main grid. DER_3 can operate in either current-controlled mode or voltage-controlled mode depending on the power-sharing scheme or operation mode of AC microgrid. The design procedure for inner controller $C_{c,3}(s)$ and outer controller $C_{v,3}(s)$ is the same as discussed for DER_1.

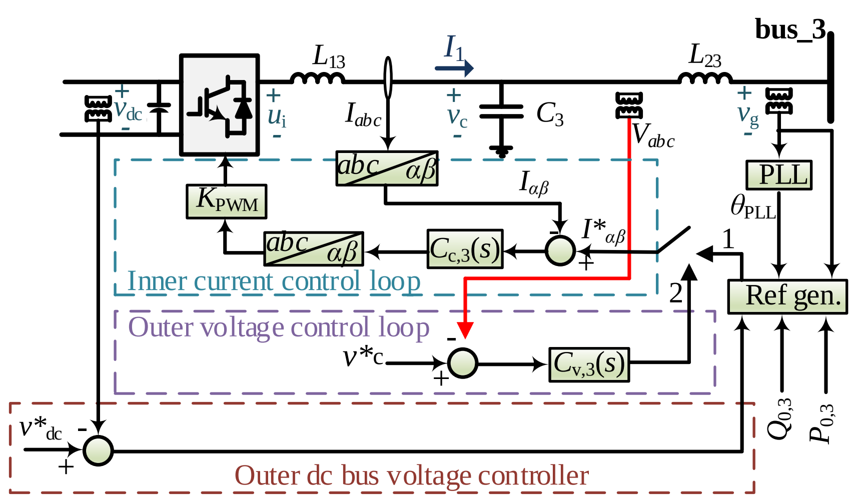

Figure 2-5 Zero level control scheme for DER_3.

2.2.2 Primary Level Control

For improving the reliability of microgrids, it is desired to share the power of loads among different DERs. The power-sharing between DERs can differ and may be specified by different requirements. It should be mentioned that DER_2 cannot participate in power-sharing scheme. This is due to the fact that DER_2 connects none-dispatchable photovoltaic panels to the grid, and it should inject all generated power of PVs into the microgrid. Therefore, it acts as a current source for the AC microgrid. The power-sharing algorithms can be grouped into two categories, i.e., centralized and decentralized. Since decentralized approaches benefit from the plug-and-play feature as well as higher reliability [4], they are of great interest.

The conventional droop algorithm [4] is a decentralized power-sharing approach. This approach tends to emulate the behavior of synchronous generators by reducing the frequency in proportional to active power demand. However, it cannot be used as an effective method in low-voltage distribution systems [4]. This is due to the fact that low-voltage distribution systems possess resistive characteristics rather than inductive characteristics, and unlike inductive grids, the active power distribution can be related to the magnitude of voltage [4]. In this case, the inverse droop characteristic is used, which is formulated as

$$f = f^* + m_\mathrm{i}\left(Q_\mathrm{i}\right)k_{\mathrm{q,i}}\,,\;\; E = E^* - n_\mathrm{i}\left(P_\mathrm{i}\right)k_{\mathrm{p,i}}, \forall \mathrm{i} \in \{1,3\}, \tag{2.6}$$

where f^* and E^* are the nominal frequency and voltage magnitude of the microgrid, respectively; m_i and n_i are droop coefficients of the i$^{\text{th}}$ source defined by maximum permissible deviation from nominal parameters in (2.7); and k_i is a correction term discussed later. The variables Q_i and P_i are obtained by passing the instantaneous reactive and active power of i$^{\text{th}}$ source through a low pass filter as in (2.8).

$$m_\mathrm{i} = \frac{\Delta f_{\max}}{Q_{\mathrm{max,DER\_i}}}\,,\;\; n_\mathrm{i} = \frac{\Delta E_{\max}}{P_{\mathrm{max,DER\_i}}}, \forall \mathrm{i} \in \{1,3\} \tag{2.7}$$

$$Q_{\mathrm{i}} = \frac{\omega_{\mathrm{c}}}{s+\omega_{\mathrm{c}}} Q_{\mathrm{i,inst}}(t)\,,\;\; P_{\mathrm{i}} = \frac{\omega_{\mathrm{c}}}{s+\omega_{\mathrm{c}}} P_{\mathrm{i,inst}}(t),\; \forall \mathrm{i} \in \{1,3\} \tag{2.8}$$

Assuming that $k_{p,i}$= $k_{q,i}$=1, the resistive droop characteristic for two DERs are depicted in Figure 2-6. Assuming that the maximum active and reactive power of DER_1 is two times of those parameters for DER_3, according to equations (2.7), the slopes of lines associated with DER_1 are half of the slopes of lines associated with DER_3, and consequently, the share of active and reactive power of DER_1 in equilibrium point (P_1, Q_1) are two times of those for DER_3, (P_3, Q_3).

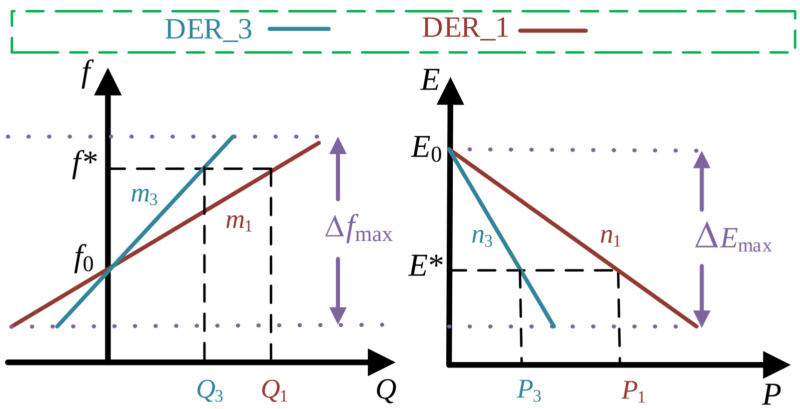

Figure 2-6 Qualitative resistive droop characteristic for DER_1 and DER_3.

2.2.3 Secondary Level Control

The purpose of this level of the hierarchical control is to compensate for the voltage drop and frequency deviation from their nominal values. This control level is typically slower than the primary control. Herein, the voltage magnitude set point E_0 and frequency set point f_0 of DERs are modified to account for the voltage and frequency deviations. This is equivalent to shifting up/down the droop characteristic lines in Figure 2-6. The schematic of the secondary control level is illustrated in Figure 2-7. To realize this control layer, a Microgrid Control Center (MGCC) unit is placed on the bus_2, as depicted in Figure 2-7. First, this unit measures the voltage magnitude E_2 and frequency f_2 on bus_2 by using a signal processor. Then, with the help of PI controllers, the voltage magnitude and frequency set points (E_0 and f_0) are regulated.

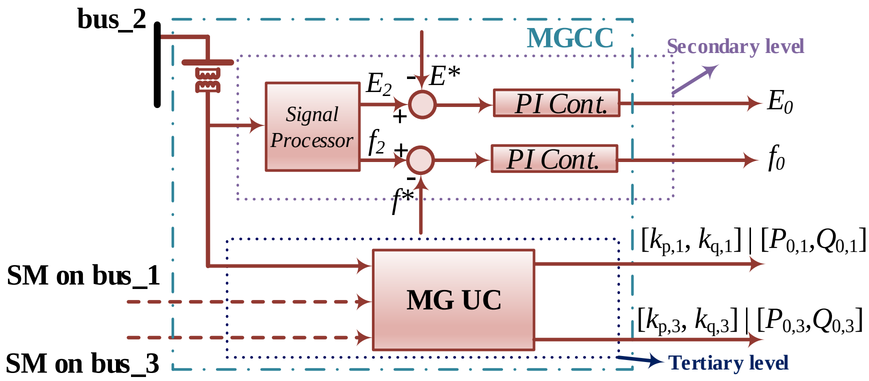

Figure 2-7 Schematic of the control function of MGCC unit.

2.2.4 Tertiary Level Control

This control level is responsible for controlling the power exchange between the microgrid and the main grid. Hence, this control is generally operational only in the grid-connected mode of the microgrid. However, in this section, the role of the tertiary level is modified to achieve the economical operation of microgrids in either grid-connected or islanded operation.

With the advances made in smart meter (SM) technology, development of smart grids with self-healing, high reliability, the real-time pricing are also become possible [59]. With the real-time pricing feature, the grid operators can decide wisely about the economical operation of the power grid, which is conventionally known as the Economic Dispatch (ED) problem in power systems. With the help of real-time pricing in microgrids, the ED problem can be addressed for shorter time intervals, which in return leads to more economical operation. Moreover, the ED problem in microgrids results in less computational complexity, since in microgrids the numbers of resources are often limited, and the constraints (e.g., ramping rate, minimum up/down time) do not exist. This means that the tertiary control level can be implemented more easily.

In this chapter, the tertiary control level is designed for addressing the ED problem in AC microgrids. The schematic of this function is depicted in Figure 2-7. The smart meters on bus_1 and bus_3 send power measurement data to the MGCC unit. Based on these data and the real-time price of electricity, the microgrid Economic Dispatch (MG ED) agent tends to minimize the operation cost of microgrid in real-time. At the tertiary level, we assume that power losses in connecting lines of microgrids are negligible, which can be the case in all small microgrids with short connecting cables. This problem can be expressed as

$$\begin{aligned} &\text{minimize } F = \sum_{i=1}^{n} (C_{\mathrm{p,i}} P_{0,\mathrm{i}}) \\ &\text{subject to} \begin{cases} \sum_{i=1}^{n} P_{0,\mathrm{i}} = P_{\mathrm{Load}} \\ P_{\mathrm{i,min}} \le P_{0,\mathrm{i}} \le P_{\mathrm{i,max}} \end{cases}, \end{aligned} \tag{2.9}$$

where $C_{\mathrm{p,i}}$ is real-time price of active power of i$^{\mathrm{th}}$ DER, respectively. After obtaining the solutions to the above optimization problem ($P_{0,\mathrm{i}}$), command signals are sent to the DERs to achieve the economical operation of the microgrid. In the proposed technique, in the islanded operation mode, the command signals $k_{\mathrm{p},1}$, $k_{\mathrm{p},3}$, are computed as

$$k_{\mathrm{p,i}} = \frac{P_{\mathrm{max,DER\_i}}}{P_{0,\mathrm{i}}}, \forall \mathrm{i} \in \{1,3\} \tag{2.10}$$

and sent to the DERs. The command signals $k_{p,1}$, $k_{p,3}$ modify the performance of primary level control, and by changing the slope of the droop lines in Figure 2-6, the most economical operation of the microgrid can be attained.

2.3 Simulation Studies

In this section, the effective performance of the proposed hierarchical scheme is validated with simulations studies. The AC microgrid nominal phase voltage and frequency are V_{ph}=120[vrms], and f=60 Hz. The capacity of DERs and the designed *LLC* filters are summarized in Table 2.1. The line impedances of the AC microgrid (line 1 and line 2) are considered to be 0.04+0.12jΩ.

	L_1 [mH]	r_{L1} [Ω]	L_2 [μH]	r_{L2} [Ω]	C [μF]	r_c [Ω]	S [kVA]	f_s [kHz]
DER_1	1	0.1	57	0.05	24	0.3	8	60
DER_2	2.8	0.1	10	0.05	9	0.6	3	60
DER_3	2	0.1	11	0.05	12	0.5	4	60

Table 2.1 Parameters of the DERs considered in simulation studies.

The controllers of DER_1, DER_2, DER_3 are assumed to have the form $C(s)=(a_2s^2+a_1s+a_0)/(b_2s^2+b_1s+b_0)$, where s represents the Laplace variable, and their respective coefficients are also summarized in Table 2.2.

	a_0	a_1	a_2	b_0	b_1	b_2
$C_{c,1}(s)$	7.2×10^4	511.9	0.5	1.42×10^5	6	1
$C_{v,1}(s)$	7.5×10^4	2658	0.53	1.42×10^5	6	1
$C_{c,2}(s)$	0.6×10^4	6116	0.6	1.42×10^5	6	1
$C_{c,3}(s)$	3.6×10^4	255.7	0.25	1.42×10^5	6	1
$C_{v,3}(s)$	3.7×10^4	1495	0.26	1.42×10^5	6	1

Table 2.2 Controllers coefficient for DER_1, DER_2, and DER_3.

It is also desired to derive the small-signal model of DERs based on the parameters provided in Table 2.1 and equations (2.1)-(2.2). The bode diagram of G_{ui} (the open-loop gain of inner current loop of DER_1) is shown in Figure 2-8 with a solid blue line. As it can be seen, the open-loop gain G_{ui} has a phase margin of 98.6 degrees at 141Hz, hence it has good phase characteristic. The bandwidth of the inner current control loop should be designed between 5% and 10% of switching frequency (60 kHz). To increase the bandwidth, a simple proportional controller can be used since G_{ui} has good phase characteristics and it is already stable.

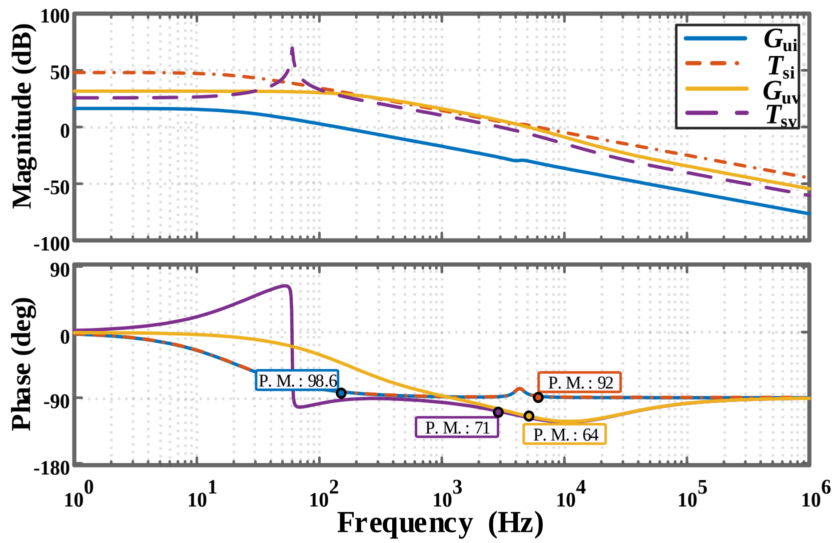

Figure 2-8 Bode diagram of the inner- and outer-control loops of DER_1 before and after compensation.

The bode diagram of T_{si} (open-loop gain of the inner-current control after compensation) is shown in Figure 2-8 with a dash-dotted red line. As it can be seen, this gain has a phase margin of 92 degrees at 6 kHz. Therefore, the inner-control loop has a good phase margin and bandwidth. The bode diagram of G_{uv} for DER_1 (open-loop gain of outer loop) is shown in Figure 2-8 with a yellow line. It is observed that this gain has a phase margin of 64 degrees at 5 kHz. This gain has a fairly good phase characteristic but two problems should be addressed.

The first problem is that the bandwidth of the outer-control loop should be adequately less than the inner-current control loop. Otherwise, the multi-loop control scheme may not work properly. Secondly, for proper tracking of a sinusoidal reference signal and attenuation of disturbances, the bode diagram of the outer-voltage loop should have a high gain around the frequency of reference signal, following the Internal Model principle [60]. To this aim, proportional resonant controllers have been proposed in the literature [61], [62]. The general form of this type of controller is shown in (**2.11**), where ω_c and ω_0 are the cutoff frequency and the fundamental frequency, respectively [61]. The cutoff frequency of the resonant filter is dependent on the application, and by decreasing this parameter the controller becomes more selective. Here, it is considered that ω_c =3 rad/sec.

$$C_{v,i}(s) = k_P + \frac{k_I s}{s^2 + 2\omega_c s + \omega_0^2} \tag{2.11}$$

The bode diagram of T_{sv} for the DER_1 (i.e., the open-loop gain of the outer loop after compensation) is shown in Figure 2-8 with a purple dashed line. As it can be seen, the bandwidth of the outer-voltage loop (3kHz) is decreased to half of the bandwidth of the inner-current loop (6kHz). Moreover, it has a good phase margin of 71 degrees and a gain of approximately 70 dB at 60Hz. Therefore, the system has good dynamic characteristics, and the reference signal can be precisely tracked. The same approach can be used for designing the controllers for the DER_3 and DER_2. The parameters of the designed droop power-sharing method are provided in Table 2.3. Moreover, since the low voltage AC microgrid is resistive, the virtual impedance concept is used to improve the transient characteristic of the reactive power-sharing among the DERs [63].

m_1	n_1	m_3	n_3	$k_{p,1}$, $k_{p,3}$ $k_{q,1}$,$k_{q,3}$
1.25×10^{-4}	1×10^{-4}	2.5×10^{-4}	2×10^{-4}	1

Table 2.3 Designed droop power sharing coefficients for DER_1 and DER_3.

Figure 2-9 shows the profile of the active and reactive power of the loads during the 1.5s simulation scenario. The simulation starts with an initial loading condition (P_{load}=5.5kW and Q_{load}=1.6kVar) Then, the load_1 and load_2 increase at t=0.3 s. and t=0.9 s, respectively. The other small load changes at t=0.6 and t=1.2 s are caused by changes occurred in the voltage magnitude of AC microgrid because loads are modelled as impedances.

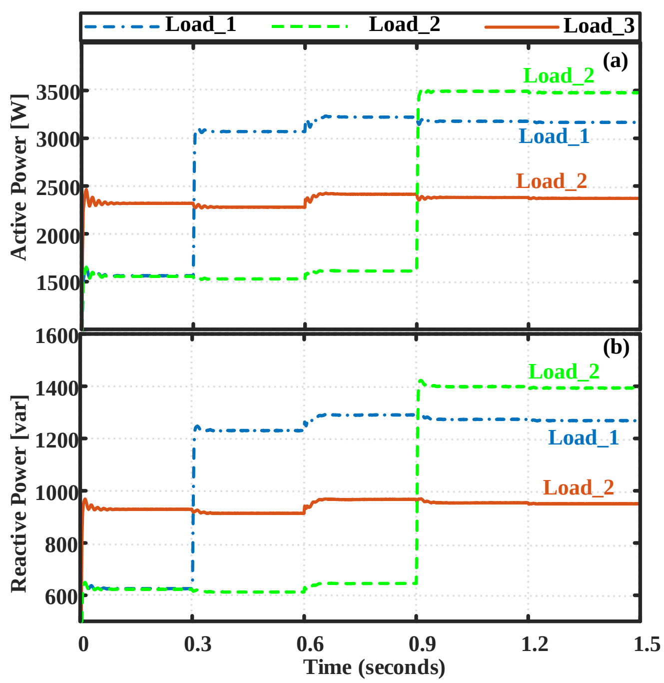

Figure 2-9 Profile of considered loads during simulation time interval of [0-1.5]s: (a) active power, and (b) reactive power.

The power generation profiles of DERs are also shown in Figure 2-10. The AC microgrid starts up at t=0s. Initially, the power is injected to the DC microgrid, and hence, the active power of DER_3 is negative. During the time period [0-0.3]s, all the loads in AC microgrids are supplied from DER_1 and DER_2. At t=0.3s, the load_1 increases, and consequently this increase is compensated by an increase of DER_1 power output. During the time interval [0.3-0.6]s, it is realized that DER_1 is close to overload condition. Consequently, at t=0.6s, the MGCC unit sends a command signal to the DER_3 to inject power from the DC microgrid to the AC microgrid. Therefore, the DER_3 output power becomes positive during the time interval [0.6-0.9]s. During this time interval, the power of the DER_1 decreases since the DER_3 is participating in power-sharing. It should be mentioned that the power-sharing is performed based on the capacity of the DERs, k_a=k_b=1, since the tertiary control level is not yet activated.

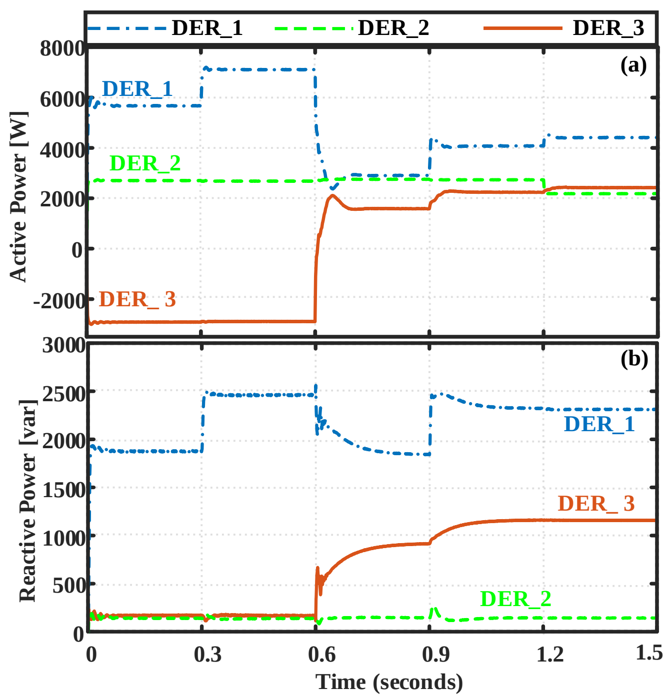

Figure 2-10 Generation profile of the DERs during time interval [0-1.5]s: (a) active power, and (b) reactive power.

At t = 0.9s, the load_2 increases, and the added load in bus_2 is shared between the DER_1 and the DER_3. At t=1.2s, the power generated by PV panels (i.e., the DER_2) is decreased, and it is compensated by increasing power output from the DER_1 and the DER_3. The profile of loads within AC microgrid is kept fairly constants the rest of the simulation scenarios during the time interval [1.5-2.7]s, and it is shown in Figure 2-11.

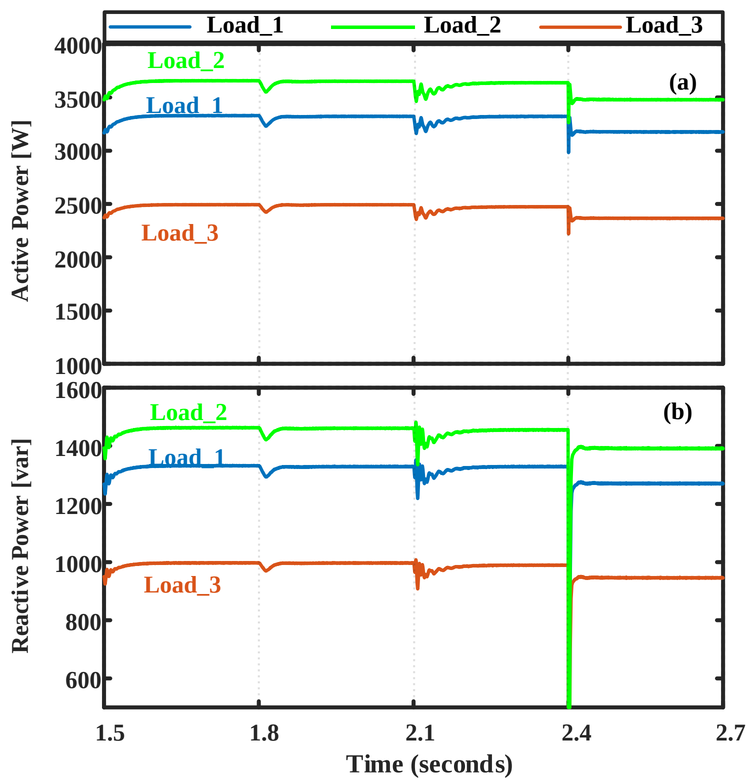

Figure 2-11 Profile of considered loads during simulation time interval of [1.5-2.7]s: (a) active power, and (b) reactive power.

Figure 2-12 depicts the generation profile of DERs during the simulation interval [1.5-2.7]s. At t=1.5s, the secondary control level is activated. Based on this control, the voltage magnitude and frequency on bus_2 are measured, and then the voltage and frequency set points are modified to return the voltage magnitude and frequency to their nominal values. Moreover, since with activating the secondary control level the voltage magnitude is increased to its nominal value, the power of loads are also increased (Figure 2-11).

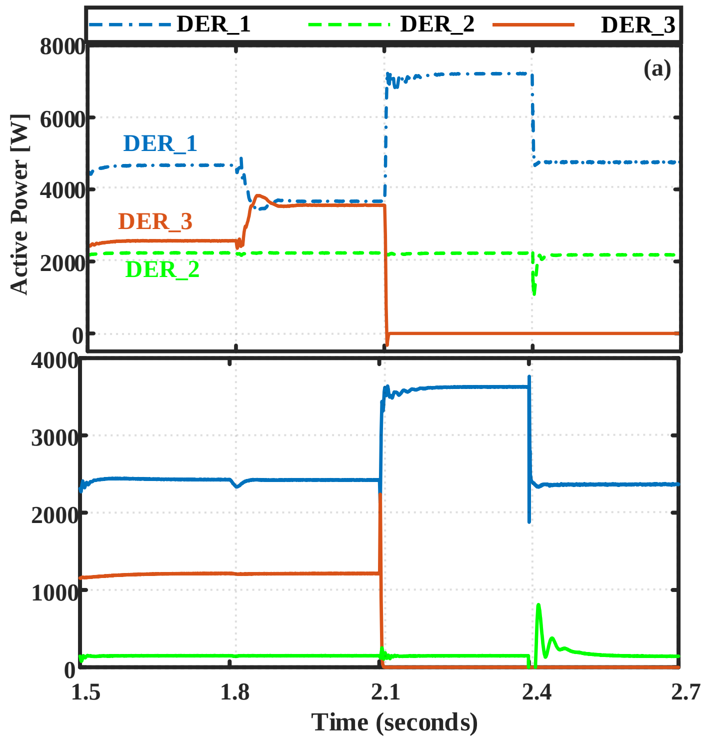

Figure 2-12 Generation profile of DERs during time interval [1.5-27] s: (a) active power, and (b) reactive power.

At t=1.8s, the tertiary control level is activated. Assuming that the real-time prices for the DERs are as $C_{p,1}$=0.8[p.u/kW], and $C_{q,3}$=0.4[p.u/kW] the command signals [$k_{p,1}$], and [$k_{p,3}$] are sent to DERs. Figure 2-12 demonstrates that during the interval [1.8-2.1]s, the power generation of the DERs changes as a result of tertiary level control. At t=2.1s, a fault occurs in the DC microgrid, and consequently, the power of DER_3 goes to zero and all the loads are supplied by the DER_1. It is also noted that since the DER_2 is composed of PV cells, it is not picking up the excess load due to being non-dispatchable. During the time interval [2.1-2.4]s, the MGCC unit detects that the DER_1 is overloaded. To reduce this power stress, at t =2.4s, the MGCC sends a command to connect to the main grid and operate in the grid-connected mode. The MGCC unit also sends a signal to the DER_1 to change its operation from islanded to grid-connected mode, and the new power reference [$P_{0,1}$, $Q_{0,1}$] is computed by solving the UC problem.

It is interesting to assess the performance of each control level. To this aim, Figure 2-13 shows bus_1 voltage as well as current of the DER_1. As it can be seen, the voltage and current have low harmonic distortion and good dynamic characteristic, which is achieved by the proper design of inverters in zero level control. Figure 2-14 depicts the power-sharing error during the time interval when both DER_1 and DER_3 are participating in the algorithm. It can be observed that the proposed power-sharing algorithm has very high accuracy for active (the error is less than 7%) and reactive power (the error is less than 1%) in the steady-state condition. Therefore, the primary level control demonstrates decent performance.

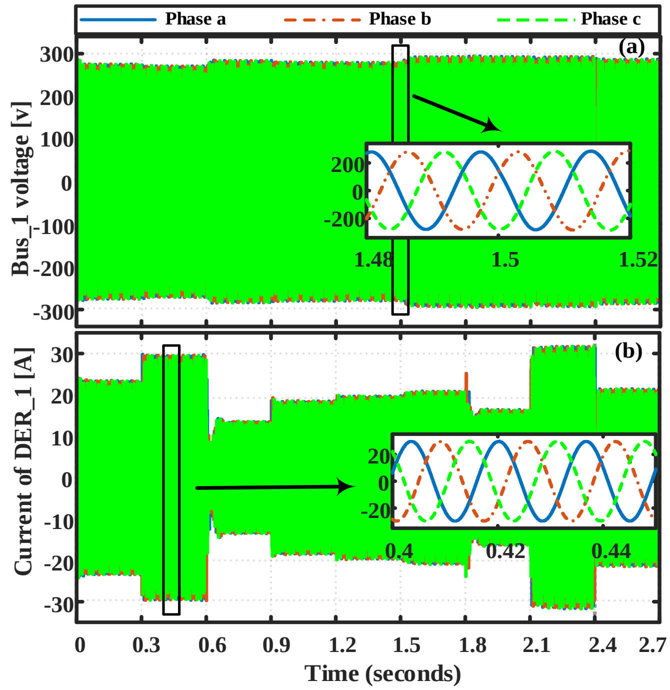

Figure 2-13 Voltages at bus_1 and currents of the DER_1 during the operation of AC microgrid: (a) voltage profile of bus_1, and (b) current profile of DER_1.

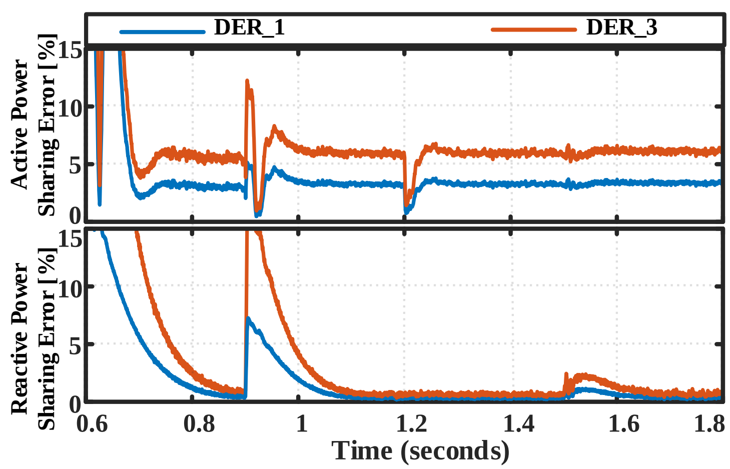

Figure 2-14 Power sharing error of the two DERs: (a) active power, (b) reactive power.

Figure 2-15 shows the profile of voltage magnitude and frequency of bus_2. It can be observed that the drop in voltage magnitude and increase in frequency are within permissible limits (i.e., 5%

of nominal voltage and 0.5 Hz). Moreover, it can be seen that the voltage magnitude and frequency are returned to their nominal value at t=1.5s when secondary level control is activated. Figure 2-16 verifies that the average cost of active power for DER_1 and DER_3 is decreased when the tertiary level control is activated at t=1.8s. Therefore, the tertiary level control is capable of minimizing the operation cost of the AC microgrid.

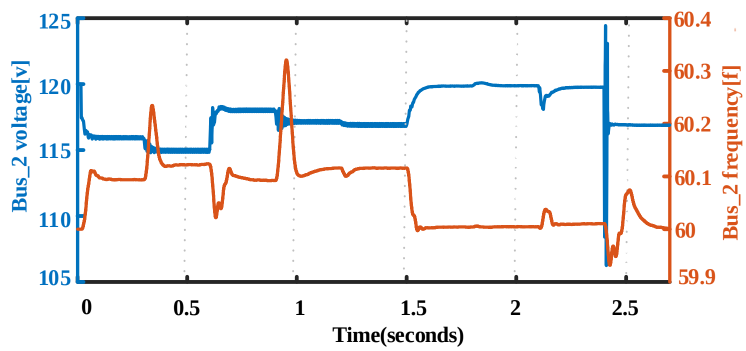

Figure 2-15 The profile of voltage magnitude and frequency at bus_2.

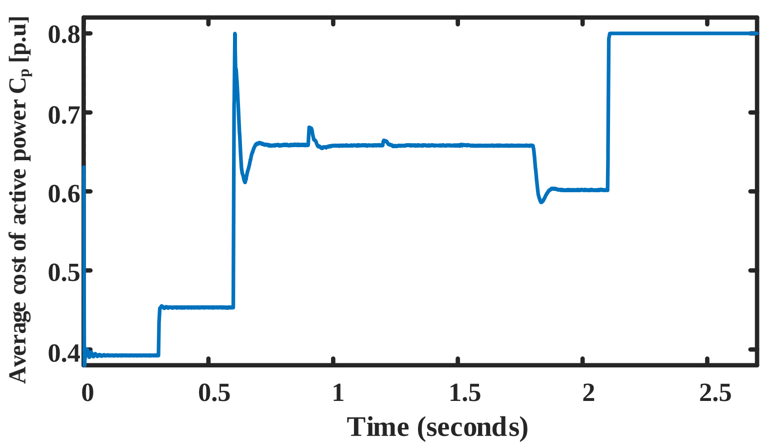

Figure 2-16 Average cost of active power of DER_1 and DER_3.

2.4 Summary

In this chapter, an effective hierarchical control method has been presented for low voltage AC microgrids. The proposed scheme has improved the regulation of AC microgrid voltage and frequency while providing a proper power-sharing among multiple DERs within the AC microgrid. The presented scheme is also demonstrated to minimize the operational cost of the microgrid by solving the optimization problem among multiple DERs in real-time.

Chapter 3: Dynamic Assessment of AC Power Load and Source

In this chapter, the dynamic characteristics of a Constant Power Load and Constant Power Source (CPL/CPS) are assessed while they are connected to an AC grid or a generic-controlled source. These dynamic characteristics can help to predict the behavior of the system in different operating points. In case the dynamic behavior of an AC system is not following a set of requirements, passive or active components can be redesigned [42], [41] or proper approaches can be adopted to improve the dynamic behavior of the system [34], [64], [65].

First, small-signal models of interconnected systems are mathematically developed. Based on these small-signal models, the closed-loop output impedances of CPL/CPS are obtained. Then, the closed-loop impedances of CPL/CPS and the sources are used to analyze the dynamic behavior of the system in different operation modes of CPL/CPS.

3.1 AC Grid-CPL/CPS System

In this subsection, we investigate the dynamic characteristic of a CPL/CPS connected to an AC system. The structure of the considered system is shown in Figure 3-1(a) and its parameters are provided in Table 3.1. This is a single bus three-phase AC system connecting an AC grid to a DC microgrid (DCMG). The CPL/CPS is responsible for regulating power transfer between DCMG and the AC source. As shown in Figure 3-1 (b), the AC grid is represented with a *LC* filter denoting an aggregated impedance of lines, transformers, and other components in a three-phase power system.

Figure 3-1(c) shows CPL/CPS and its control system. It works in a current-controlled mode implemented in $\alpha\beta$ frame. The reference for the current loop is calculated based on $\alpha\beta$ component of grid voltage. The circuit includes a power electronic converter and a *LLC* filter to attenuate switching harmonics.

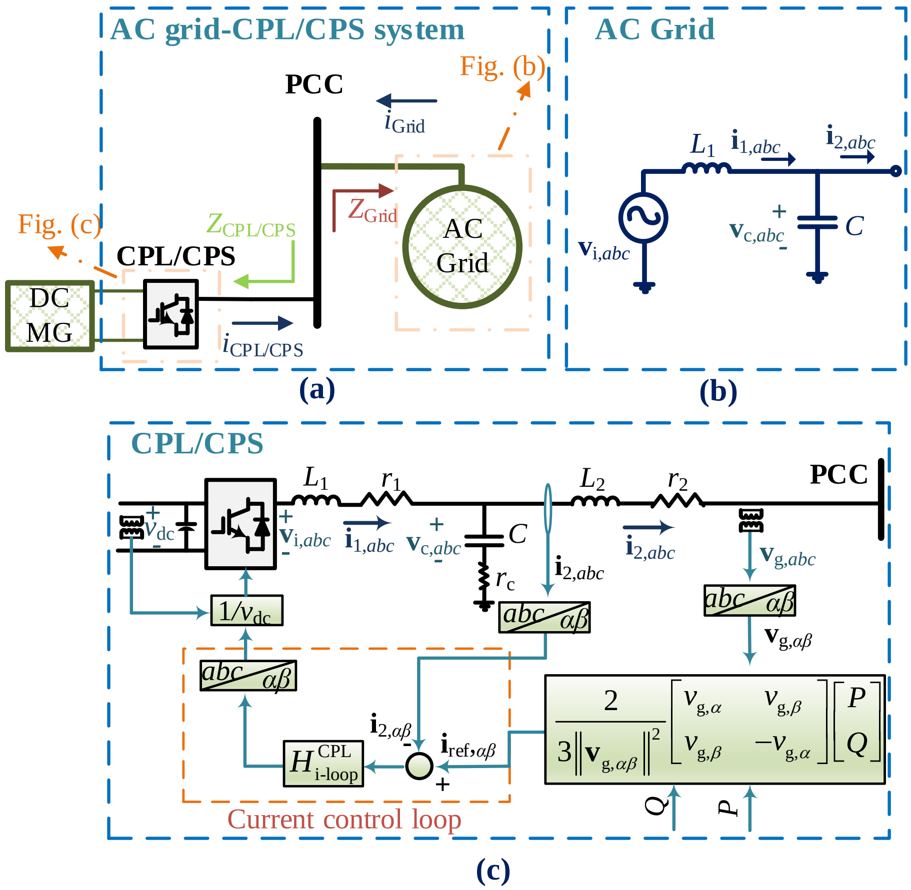

Figure 3-1 Considered AC system and its components: (a) high-level architecture AC grid-CPL/CPS system, (b) AC grid, and (c) CPL/CPS and its control system.

Components	*Parameters & values*
CPL/CPS	L_1 =3mH, r_{L1}=0.1Ω, L_2 =1mH, r_{L2}=0.05Ω, C=30μF, r_c =0.25Ω
AC Grid	L_1 =3mH, r_{L1}=0.1Ω, C=30μF, r_c=0.3Ω

Table 3.1 Parameters of CPL/CPS and AC grid.

3.1.1 Small-Signal Modeling of AC Grid-CPL/CPS System

In this subsection small-signal model of open-loop CPL/CPS is derived first. This model is useful for designing the controller $H_{\text{i-loop}}^{\text{CPL}}$ which regulates output current $\mathbf{i}_{2,abc}$. Moreover, with the help of small-signal modeling, the output closed-loop impedance of the converter can be obtained which will be later used for stability analysis. For the purpose on notations in this thesis, real vectors are denoted by lower-case bold letters, as $\boldsymbol{f}_{x,\alpha\beta}=[f_{x,\alpha}\ \ f_{x,\beta}]^{\mathrm{T}}$; and matrices are denoted by upper-case bold letters. In addition, the subscripts abc, $\alpha\beta$, and dq denote the coordinates in which the respective variables are expressed. Considering the parameters shown in Figure 3-2, the state-space model of CPL/CPS can be expressed as

$$
\begin{aligned}
&\dot{\mathbf{x}}_{\mathrm{LLC},\alpha\beta} = \mathbf{A}_{\mathrm{LLC},\alpha\beta}\mathbf{x}_{\mathrm{LLC},\alpha\beta} + \mathbf{B}_{\mathrm{i}}\mathbf{v}_{\mathrm{i},\alpha\beta} + \mathbf{B}_{\mathrm{g}}\mathbf{v}_{\mathrm{g},\alpha\beta},\ \mathbf{x}_{\mathrm{LLC},\alpha\beta} = [\,\mathbf{i}_{1,\alpha\beta}\quad \mathbf{v}_{\mathrm{c},\alpha\beta}\quad \mathbf{i}_{2,\alpha\beta}\,]^{\mathrm{T}},\\
&\mathbf{A}_{\mathrm{LLC},\alpha\beta} = \begin{bmatrix} a_{11} & 0 & a_{13} & 0 & a_{15} & 0\\ 0 & a_{21} & 0 & a_{24} & 0 & a_{26}\\ a_{31} & 0 & 0 & 0 & a_{35} & 0\\ 0 & a_{42} & 0 & 0 & 0 & a_{46}\\ a_{51} & 0 & a_{53} & 0 & a_{55} & 0\\ 0 & a_{62} & 0 & a_{64} & 0 & a_{66} \end{bmatrix},\\
&\Rightarrow \begin{cases} a_{11} = a_{21} = -\dfrac{r_{\mathrm{c}}+r_1}{L_1},\ a_{13} = a_{24} = -\dfrac{1}{L_1}, a_{15} = a_{26} = \dfrac{r_{\mathrm{c}}}{L_1}\\ a_{31} = a_{42} = \dfrac{1}{C},\ a_{35} = a_{46} = -\dfrac{1}{C}\\ a_{51} = a_{62} = \dfrac{r_{\mathrm{c}}}{L_2},\ a_{53} = a_{64} = -\dfrac{1}{L_2}, a_{55} = a_{66} = -\dfrac{r_{\mathrm{c}}+r_1}{L_2} \end{cases},\\
&\mathbf{B}_{\mathrm{i}} = \begin{bmatrix} 1/L_1 & 0 & 0 & 0 & 0 & 0\\ 0 & 1/L_1 & 0 & 0 & 0 & 0 \end{bmatrix}^{\mathrm{T}},\ \mathbf{B}_{\mathrm{g}} = \begin{bmatrix} 0 & 0 & 0 & 0 & -1/L_2 & 0\\ 0 & 0 & 0 & 0 & 0 & -1/L_2 \end{bmatrix}^{\mathrm{T}}.
\end{aligned}
\tag{3.1}
$$

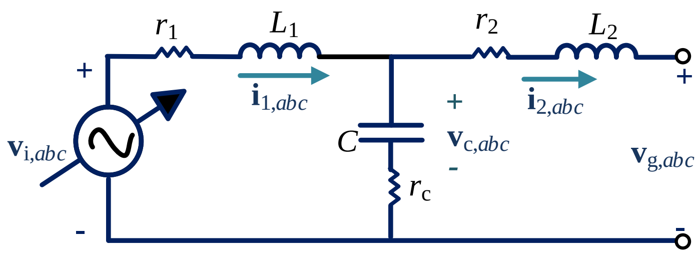

Figure 3-2 Small signal model of LLC filter.

This state-space model can be used to derive a matrix transfer function from modulated voltages $\hat{\mathbf{v}}_{i,\alpha\beta}$ to output currents $\hat{\mathbf{i}}_{2,\alpha\beta}$ as

$$\mathbf{G}_{vi}(s)=\begin{bmatrix}\dfrac{\hat{i}_{2,\alpha}}{\hat{v}_{i,\alpha}} & \dfrac{\hat{i}_{2,\alpha}}{\hat{v}_{i,\beta}}\\ \dfrac{\hat{i}_{2,\beta}}{\hat{v}_{i,\beta}} & \dfrac{\hat{i}_{2,\beta}}{\hat{v}_{i,\beta}}\end{bmatrix}=\begin{bmatrix}G_{vi,\alpha\alpha}(s) & 0\\ 0 & G_{vi,\beta\beta}(s)\end{bmatrix}. \tag{3.2}$$

Since there is no coupling between $\alpha\beta$ components in the developed state-space model, the matrix impedance $\mathbf{G}_{vi}(s)$ is diagonal and symmetric. The diagonal elements are high-order transfer functions in the form of $G_{vi,\alpha\alpha}(s)=G_{vi,\beta\beta}(s)=N(s)/M(s),$ which are obtained using a numerical approach. Therefore, the CPL/CPS output current can be independently controlled using one controller $H_{\text{i-loop}}^{\text{CPL}}$ in each axis. The controller $H_{\text{i-loop}}^{\text{CPL}}$ is designed in a way that the open-loop gain of the CPL/CPS defined as

$$T_{si,\alpha\alpha}=T_{si,\beta\beta}=G_{ui,\alpha\alpha}\times H_{\text{i-loop}}^{\text{CPL}}\times K_{pwm}, \tag{3.3}$$

should have a positive phase margin, where K_{pwm} represents the pulse-width modulation gain. The coefficients of the designed controller $H_{\text{i-loop}}^{\text{CPL}}$ in form of $H=(a_2s^2+a_1s+a_0)/(b_2s^2+b_1s+b_0)$ are provided in Table 3.2.

	a_0	a_1	a_2	b_0	b_1	b_2
$H_{\text{i-loop}}^{\text{CPL}}$	6.5×10^5	4607	4.58	1.42×10^5	6	1

Table 3.2 Coefficients of CPL/CPS controller.

After designing the controller $H_{\text{i-loop}}^{\text{CPL}}$, the closed-loop state-space model of CPL/CPS can be derived. Assuming that the state-space model of the control system is expressed as

$$H_{\text{i-loop}}^{\text{CPL}} \rightarrow \begin{cases} \dot{\mathbf{x}}_{\text{i-loop},\alpha\beta} = \mathbf{A}_{\text{c}}\mathbf{x}_{\text{i-loop},\alpha\beta} + \mathbf{B}_{\text{c}}\mathbf{u}_{\text{i-loop},\alpha\beta} \\ \mathbf{y}_{\text{i-loop},\alpha\beta} = \mathbf{C}_{\text{c}}\mathbf{x}_{\text{i-loop},\alpha\beta} + \mathbf{D}_{\text{c}}\mathbf{u}_{\text{i-loop},\alpha\beta} \end{cases}, \tag{3.4}$$

the complete state-space model of CPL/CPS is as

$$\begin{aligned} &\dot{\mathbf{x}}_{\text{CPL},\alpha\beta} = \mathbf{A}_{\text{CPL},\alpha\beta}\mathbf{x}_{\text{CPL}} + \mathbf{B}_{\text{CPL}}\mathbf{i}_{\text{ref},\alpha\beta} + \mathbf{M}_{\text{CPL}}\mathbf{v}_{\text{g},\alpha\beta}, \ \mathbf{x}_{\text{CPL},\alpha\beta} = [\mathbf{x}_{\text{LLC},\alpha\beta} \quad \mathbf{x}_{\text{i-loop},\alpha\beta}]^{\text{T}} \\ &\mathbf{A}_{\text{CPL},\alpha\beta} = \begin{bmatrix} \mathbf{A}_{\text{LLC},\alpha\beta} - \mathbf{B}_{\text{i}}\mathbf{D}_{\text{c}}\mathbf{S}_1 & \mathbf{B}_{\text{i}}\mathbf{C}_{\text{c}} \\ \mathbf{-B}_{\text{c}}\mathbf{S}_1 & \mathbf{A}_{\text{c}} \end{bmatrix}, \mathbf{B}_{\text{CPL}} = \begin{bmatrix} \mathbf{B}_{\text{i}}\mathbf{D}_{\text{c}} & \mathbf{B}_{\text{c}} \end{bmatrix}^{\text{T}}, \\ &\mathbf{M}_{\text{CPL}} = \begin{bmatrix} \mathbf{B}_{\text{g}} & \mathbf{0} \end{bmatrix}^{\text{T}}, \ \mathbf{S}_1 = \begin{bmatrix} 0 & 0 & 0 & 0 & 1 & 0 \\ 0 & 0 & 0 & 0 & 0 & 1 \end{bmatrix}, \mathbf{i}_{\text{ref},\alpha\beta} = \frac{2}{3\|\mathbf{v}_{\text{g},\alpha\beta}\|^2}\begin{bmatrix} v_{\text{g},\alpha} & v_{\text{g},\beta} \\ v_{\text{g},\beta} & -v_{\text{g},\alpha} \end{bmatrix}\begin{bmatrix} P \\ Q \end{bmatrix}. \end{aligned} \tag{3.5}$$

The developed state-space model in (3.5) is non-linear and notation ||.|| denotes the Euclidean norm of the respective vector. Consequently, deriving the input closed-loop impedance may not be straight forward. To solve this issue, the developed state-space model is transformed into a time-invariant model by using Park transformation **T** as

$$\mathbf{T} = \begin{bmatrix} \cos(\omega_1 t) & \sin(\omega_1 t) \\ -\sin(\omega_1 t) & \cos(\omega_1 t) \end{bmatrix}, \tag{3.6}$$

where ω_1 is the fundamental angular frequency of the main AC grid. The resultant state-space model can be expressed as

$$\dot{\mathbf{x}}_{\text{CPL},dq} = \mathbf{A}_{\text{CPL},dq}\mathbf{x}_{\text{CPL},dq} + \mathbf{B}_{\text{CPL}}\mathbf{i}_{\text{ref},dq} + \mathbf{M}_{\text{CPL}}\mathbf{v}_{\text{g},dq}, \ \mathbf{x}_{\text{CPL},dq} = [\mathbf{x}_{\text{LLC},dq} \quad \mathbf{x}_{\text{i-loop},dq}]^{\text{T}},$$

$$\mathbf{A}_{\mathrm{CPL},dq} = \begin{bmatrix} \mathbf{A}_{\mathrm{LLC},\alpha\beta} + \mathbf{W}_1 - \mathbf{B}_{\mathrm{i}}\mathbf{D}_{\mathrm{c}}\mathbf{S}_1 & \mathbf{B}_{\mathrm{i}}\mathbf{C}_{\mathrm{c}} \\ -\mathbf{B}_{\mathrm{c}}\mathbf{S}_1 & \mathbf{A}_{\mathrm{c}} + \mathbf{W}_{\mathrm{c}} \end{bmatrix}, \mathbf{W}_{\mathrm{c}} = \begin{bmatrix} 0 & \omega_1 & 0 & 0 \\ -\omega_1 & 0 & 0 & 0 \\ 0 & 0 & 0 & \omega_1 \\ 0 & 0 & -\omega_1 & 0 \end{bmatrix},$$

$$\mathbf{W}_1 = \begin{bmatrix} 0 & \omega_1 & 0 & 0 & 0 & 0 \\ -\omega_1 & 0 & 0 & 0 & 0 & 0 \\ 0 & 0 & 0 & \omega_1 & 0 & 0 \\ 0 & 0 & -\omega_1 & 0 & 0 & 0 \\ 0 & 0 & 0 & 0 & 0 & \omega_1 \\ 0 & 0 & 0 & 0 & -\omega_1 & 0 \end{bmatrix}, \mathbf{i}_{\mathrm{ref},dq} = \frac{2}{3\|\mathbf{v}_{\mathrm{g},dq}\|^2} \begin{bmatrix} v_{\mathrm{g},d} & v_{\mathrm{g},q} \\ v_{\mathrm{g},q} & -v_{\mathrm{g},d} \end{bmatrix} \begin{bmatrix} P \\ Q \end{bmatrix}. \tag{3.7}$$

This state-space model includes non-linear terms and should be linearized around an operating point. The linear state-space model then can be expressed as

$$\dot{\hat{\mathbf{x}}}_{\mathrm{CPL},dq} = \mathbf{A}_{\mathrm{CPL},dq}\hat{\mathbf{x}}_{\mathrm{CPL},dq} + \mathbf{E}_{\mathrm{CPL},dq}\hat{\mathbf{v}}_{\mathrm{g},dq}, \hat{\mathbf{i}}_{\mathrm{ref},dq} = \frac{2}{3\bar{v}_{\mathrm{g},d}^2} \begin{bmatrix} -P & Q \\ Q & P \end{bmatrix} \begin{bmatrix} \hat{v}_{\mathrm{g},d} \\ \hat{v}_{\mathrm{g},q} \end{bmatrix} = \mathbf{N} \begin{bmatrix} \hat{v}_{\mathrm{g},d} \\ \hat{v}_{\mathrm{g},q} \end{bmatrix},$$
$$\mathbf{E}_{\mathrm{CPL},dq} = \begin{bmatrix} \mathbf{B}_{\mathrm{i}}\mathbf{D}_{\mathrm{c}}\mathbf{N} + \mathbf{B}_{\mathrm{g}} & \mathbf{B}_{\mathrm{c}}\mathbf{N} \end{bmatrix}^{\mathrm{T}}. \tag{3.8}$$

Based on the developed linear state-space model, the input admittance of the CPL/CPS in *dq* frame can be derived as

$$\mathbf{Y}_{\mathrm{CPL/CPS},dq}(s) = \begin{bmatrix} \frac{-\hat{i}_{2,d}}{\hat{v}_{\mathrm{g},d}} & \frac{-\hat{i}_{2,d}}{\hat{v}_{\mathrm{g},q}} \\ \frac{-\hat{i}_{2,q}}{\hat{v}_{\mathrm{g},d}} & \frac{-\hat{i}_{2,q}}{\hat{v}_{\mathrm{g},q}} \end{bmatrix} = \begin{bmatrix} y_{dd}(s) & y_{dq}(s) \\ y_{qd}(s) & y_{qq}(s) \end{bmatrix}, \tag{3.9}$$

which is a full matrix, and its individual transfer functions are constructed numerically. After obtaining the input admittance of CPL/CPS, we need to derive the output impedance of the AC grid to perform stability analysis. Considering the parameters shown in Figure 3-3, the state-space model of the AC grid is as

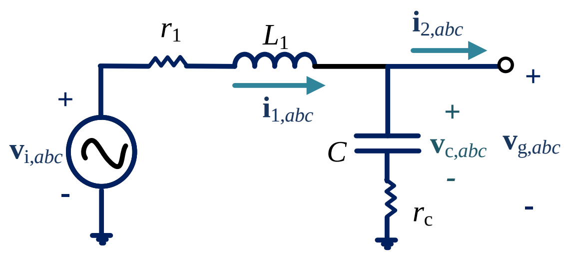

Figure 3-3 Structure of the equivalent AC grid representation.

$$\begin{gathered}
\dot{\mathbf{x}}_{\mathrm{LC},\alpha\beta} = \mathbf{A}_{\mathrm{LC},\alpha\beta}\mathbf{x}_{\mathrm{LC},\alpha\beta} + \mathbf{B}_{\mathrm{i}}\mathbf{v}_{\mathrm{i},\alpha\beta} + \mathbf{B}_{\mathrm{o}}\mathbf{i}_{2,\alpha\beta}, \mathbf{x}_{\mathrm{LC},\alpha\beta} = \begin{bmatrix} \mathbf{i}_{1,\alpha\beta} & \mathbf{v}_{\mathrm{c},\alpha\beta} \end{bmatrix}^{\mathrm{T}}, \\
\mathbf{A}_{\mathrm{LC},\alpha\beta} = \begin{bmatrix} a_{11} & 0 & a_{13} & 0 \\ 0 & a_{12} & 0 & a_{24} \\ a_{31} & 0 & 0 & 0 \\ 0 & a_{42} & 0 & 0 \end{bmatrix}, \begin{cases} a_{11} = a_{21} = -\dfrac{r_{\mathrm{c}} + r_1}{L_1}, \ a_{13} = a_{24} = -\dfrac{1}{L_1}, \\ a_{31} = a_{43} = \dfrac{1}{C} \end{cases} \\
\mathbf{B}_{\mathrm{i}} = \begin{bmatrix} 1/L_1 & 0 & 0 & 0 \\ 0 & 1/L_1 & 0 & 0 \end{bmatrix}^{\mathrm{T}}, \mathbf{B}_{\mathrm{o}} = \begin{bmatrix} r_{\mathrm{c}}/L_1 & 0 & -1/C & 0 \\ 0 & r_{\mathrm{c}}/L_1 & 0 & -1/C \end{bmatrix}^{\mathrm{T}}.
\end{gathered} \tag{3.10}$$

Since this state-space model is linear, we can obtain the output impedance of grid without using Park transformation. The impedance of the grid Z_{grid} can be obtained as

$$\mathbf{Z}_{\mathrm{grid},\alpha\beta}(s) = \begin{bmatrix} \dfrac{-\hat{v}_{\mathrm{g},\alpha}}{\hat{i}_{2,\alpha}} & \dfrac{-\hat{v}_{\mathrm{g},\alpha}}{\hat{i}_{2,\beta}} \\ \dfrac{-\hat{v}_{\mathrm{g},\beta}}{\hat{i}_{2,\alpha}} & \dfrac{-\hat{v}_{\mathrm{g},\beta}}{\hat{i}_{2,\beta}} \end{bmatrix} = \begin{bmatrix} Z_{\mathrm{grid},\alpha\alpha}(s) & 0 \\ 0 & Z_{\mathrm{grid},\beta\beta}(s) \end{bmatrix}. \tag{3.11}$$

After some manipulations, it can be shown that $\mathbf{Z}_{\mathrm{grid},\alpha\beta}(s)$ is a diagonal matrix, (as expected, a decoupled matrix impedance in *abc* frame is also a decoupled matrix impedance in stationary *αβ* frame). Furthermore, the diagonal elements of $\mathbf{Z}_{\mathrm{grid},\alpha\beta}(s)$ have the following form

$$Z_{\mathrm{grid},\alpha\alpha}(s) = Z_{\mathrm{grid},\beta\beta}(s) = \frac{s^2 L_1 C r_{\mathrm{c}} + s(L_1 + C r_{\mathrm{c}} r_1) + r_1}{s^2 L_1 C + sC(r_1 + r_{\mathrm{c}}) + 1}. \tag{3.12}$$

After obtaining the closed-loop admittance of CPL/CPS and the impedance of the AC grid, we can perform stability analysis which is provided in the following subsection.

3.1.2 Stability Analysis of AC Grid-CPL/CPS System

Stability analysis of the system shown in Figure 3-1(a) can be performed by adopting impedance-based stability analysis [66]. This approach, assess the stability of an AC system based on the impedance ratio of a source and a load. This approach requires impedances of source and load to be in the same coordinate. Since the developed admittance of CPL/CPS is in *dq* frame (equation (3.9)) and impedance of the AC grid is in *αβ* frame (equation (3.15)), we need to transfer both impedances to the same coordinate. In this chapter, the unifying approach is adopted to this aim.

The unifying approach transfers a 2×2 transfer matrix to two complex transfer functions. In this approach, the admittance of CPL/CPS is first transferred to a complex *dq* frame using

$$\mathbf{Y}^{\mathrm{c}}_{\mathrm{CPL/CPS},dq}(s)=\begin{bmatrix} y_{+,dq}(s) & y_{-,dq}(s) \\ y^{*}_{-,dq}(s) & y^{*}_{+,dq}(s)\end{bmatrix},\begin{cases} y_{+,dq}(s)=0.5\left[y_{dd}(s)+y_{qq}(s)+j(y_{qd}(s)\text{-}y_{dq}(s))\right] \\ y_{-,dq}(s)=0.5\left[y_{dd}(s)\text{-}y_{qq}(s)+j(y_{qd}(s)+y_{dq}(s))\right]\end{cases}, \tag{3.13}$$

where superscript ‘c’ in $\mathbf{Y}^{\mathrm{c}}_{\mathrm{CPL/CPS},dq}(s)$ denotes complex transfer function, $y^{*}_{+,dq}(s)$ and $y^{*}_{-,dq}(s)$ are complex conjugate of $y_{+,dq}(s)$ and $y_{-,dq}(s)$, respectively. Then, the equivalent impedance in complex *αβ* frame $\mathbf{Y}^{\mathrm{c}}_{\mathrm{CPL/CPS},\alpha\beta}(s)$ is obtained by a shift in the frequency as

$$\mathbf{Y}^{\mathrm{c}}_{\mathrm{CPL/CPS},\alpha\beta}(s)=\mathbf{Y}^{\mathrm{c}}_{\mathrm{CPL/CPS},dq}(s-j\omega_1). \tag{3.14}$$

It can be shown [41] that there could be a coupling between positive and negative sequence components of a three-phase system in case $\omega>2\omega_1$. Provided that $\omega<2\omega_1$, two positive frequency components present in the three-phase system [41]. Moreover, it can be shown [4] that the grid impedance matrix in $\alpha\beta$ frame $\mathbf{Z}_{\text{grid},\alpha\beta}(s)$ can be transferred to the complex $\alpha\beta$ frame using the following:

$$\mathbf{Z}^{\text{c}}_{\text{grid},\alpha\beta}(s)=\begin{bmatrix} Z_{\text{grid},\alpha\alpha}(s) & 0 \\ 0 & Z_{\text{grid},\beta\beta}(s-2j\omega_1) \end{bmatrix}. \tag{3.15}$$

Since now the impedance of the grid and admittance of CPL/CPS are in the same coordinate (complex $\alpha\beta$ frame), impedance-based stability analysis can be performed. According to Nyquist criteria, the stability can be determined by plotting the frequency responses of eigenvalues of impedance ratio [41]. Since we have source impedance and load admittance, we defined their product as

$$\mathbf{G}(s)=\mathbf{Z}^{\text{c}}_{\text{grid},\alpha\beta}(s)\mathbf{Y}^{\text{c}}_{\text{CPL},\alpha\beta}(s). \tag{3.16}$$

Investigating the eigenvalues of $\mathbf{G}(s)$, it becomes possible to identify the candidate frequencies for interaction between the AC grid and the CPL. These candidate frequencies are the ones at which phase of the eigenvalues reaches -180 degrees. If the magnitude of an eigenvalue is positive at a candidate frequency (gain margin is negative), an instability happens at that candidate frequency. It should be mentioned that candidate frequencies are in pairs meaning that if there is one candidate frequency at ω, there would be another candidate frequency at $2\omega_1$- ω.

Figure 3-4 shows the frequency responses of eigenvalues of impedance ratio matrix **G** for two different power consumption profiles. In the first scenario, CPL is consuming active power P=8kW and reactive power Q=1kVar (solid lines), and in the second scenario it is consuming P= 8.5kW, and the reactive power is kept constant at Q=1kVar (dashed lines). For both power consumption profiles, it can be seen that the phase reaches -180 degrees at different frequencies. These are candidate frequencies for the interaction between the grid and CPL. For example, for P=8kW, the candidate frequencies of λ_1 are around -164Hz and -20Hz, and the candidate frequencies of λ_2 are around 140Hz and 285Hz. The gain margins at all candidate frequencies are positive; therefore, instability cannot occur when the CPL operating point is {P=8.5kW, Q=1kVar}. Similarly for P=8.5kW, the gain margins at all candidate frequencies (λ_1:-173Hz, -20Hz, and λ_2:140Hz, 294Hz) are positive. Therefore, instability cannot occur when the power consumption of CPL is either {P=8.5kW, Q=1kVar}.

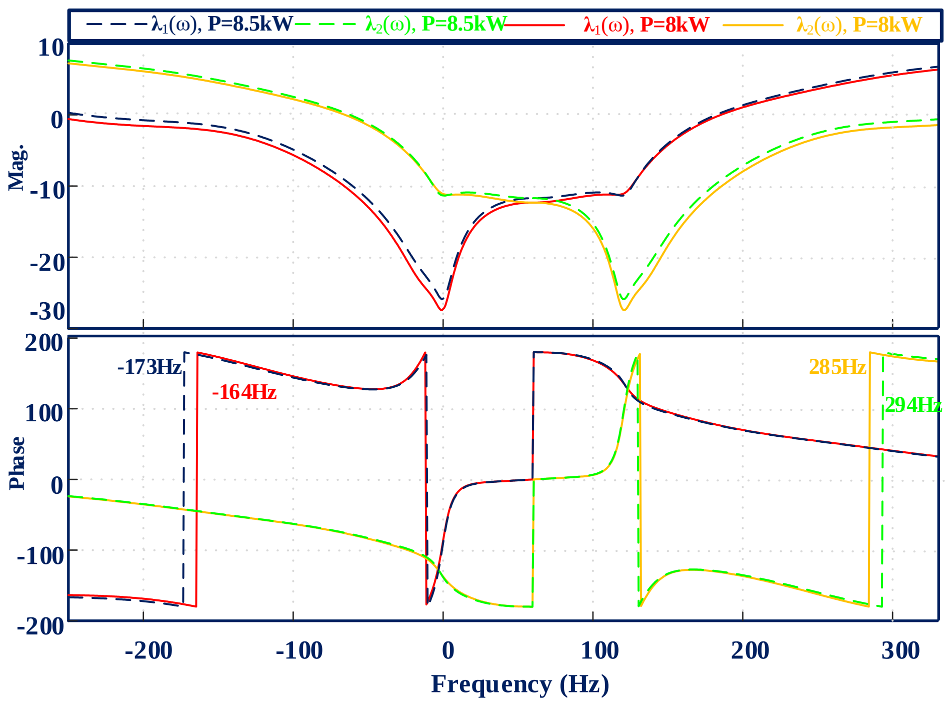

Figure 3-4 Frequency responses of eigenvalues of impedance ratio matrix G for AC grid-CPL system when CPL power consumption is {P=8kW, Q=1kVar}, and {P=8.5kW, Q=1kVar}.

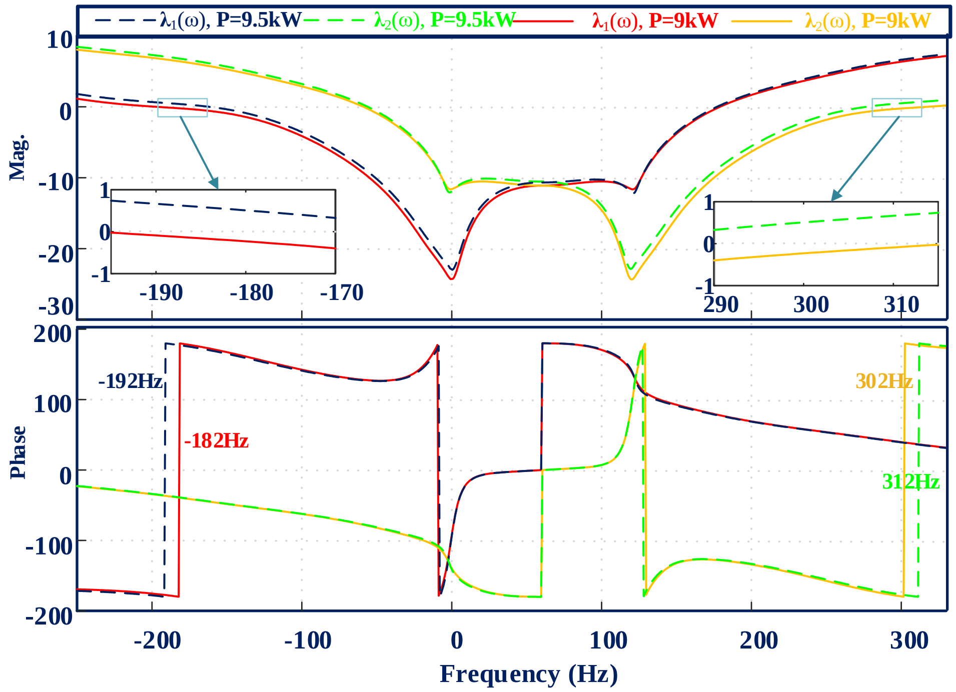

Figure 3-5 Frequency responses of eigenvalues of impedance ratio matrix G for AC grid-CPL system when CPL power consumption is {P=9kW, Q=1kVar}, and {P=9.5kW, Q=1kVar}.

Figure 3-5 shows the frequency responses of eigenvalues of impedance ratio matrix **G** when the power consumption of CPL are {P=9kW, Q=1kVar} (solid lines), and {P=9.5kW, Q=1kVar} (dashed lines). When CPL is consuming P=9kW, there are different frequencies at which phase reaches -180 degrees. Among these candidate frequencies, it can be seen that the gain margins are positive at candidate frequencies λ_1:-20Hz or λ_2:140Hz. The other candidate frequencies around -λ_1:-182Hz and λ_2:302Hz need further attention. The zoom-in plot shows the magnitude of eigenvalues around these candidate frequencies. It can be seen that the gain margin is still positive at the candidate frequencies λ_1:-182Hz and λ_2:302Hz. Therefore, no instability can happen when CPL is consuming P=9kW.

Similarly, there are different candidate frequencies when CPL is consuming P=9.5kW. The gain margins at candidate frequencies λ_1:-20Hz or λ_2:140Hz are positive. The zoom-in plot, however, shows that the gain margins at candidate frequencies λ_1:-192Hz and λ_2:312Hz are negative. Therefore, when CPL is consuming 9.5kW, an interaction happens between CPL and the AC grid, and the system shown in Figure 3-1(a) is destabilized.

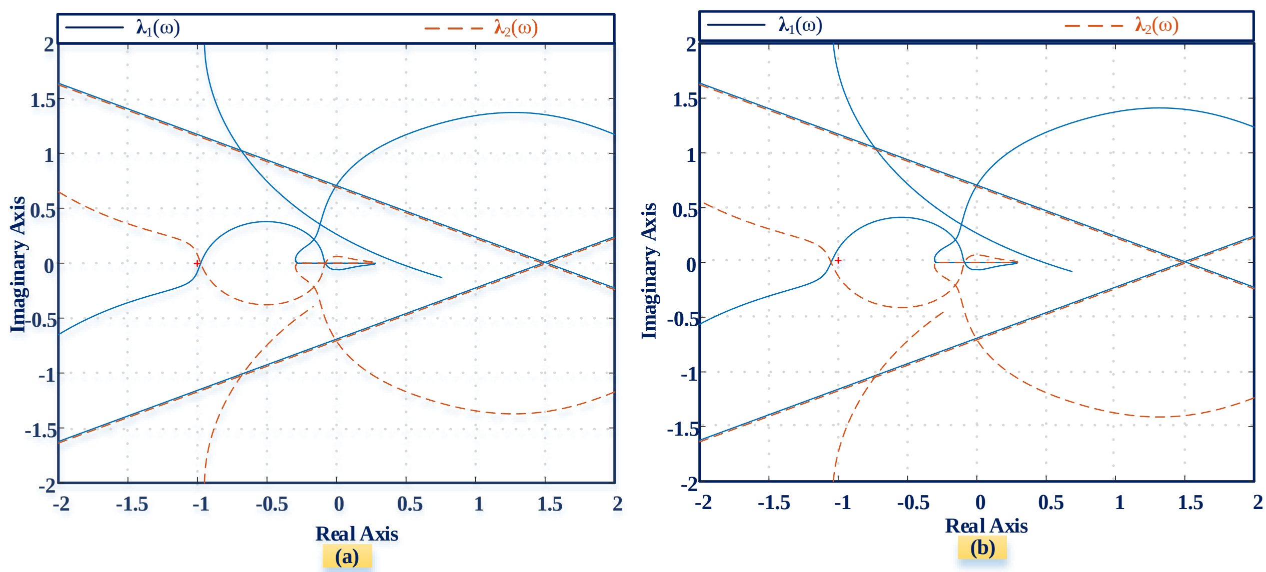

Figure 3-6 Nyquist plot of eigenvalues of matrix G for AC grid-CPL system: (a) CPL power consumption is P=9kW, Q=1kVar; and (b) CPL power consumption is P=9.5kW, Q=1kVar.

Nyquist plots of eigenvalues of matrix **G** are shown in Figure 3-6. It can be seen that when CPL is consuming P=9kW and Q=1kVar the Nyquist plot in Figure 3-6 (a) does not encircle the critical point (-1+0j). However, when CPL is consuming P=9.5kW and Q=1kVar the Nyquist plot in Figure 3-6 (b) encircles critical point, predicting instability of the considered AC grid-CPL system.

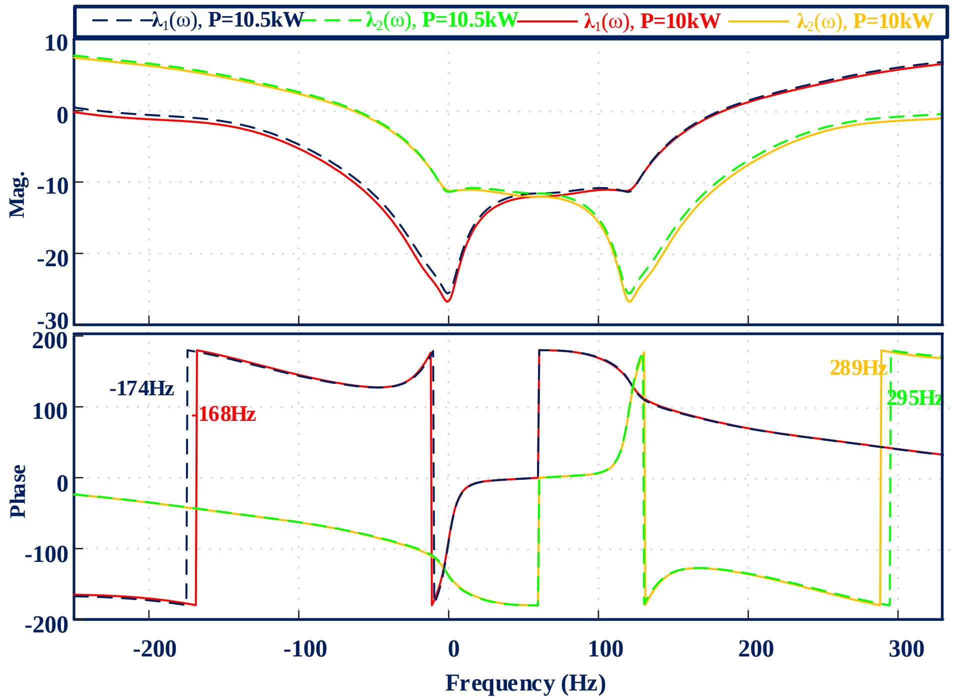

Figure 3-7 Frequency responses of eigenvalues of impedance ratio matrix G for AC grid-CPS system when CPS power generation is {P=10kW, Q=1kVar}, and {P=10.5kW, Q=1kVar}.

Figure 3-7 shows the frequency responses of eigenvalues of impedance ratio matrix **G** when CPS is generating active and reactive power as {P=10kW, Q=1kVar} and {P=10.5kW, Q=1kVar}. As it can be seen, for the two cases there are different candidate frequencies. However, the gain margins at none of these candidate frequencies are negative. Therefore, the considered AC grid-CPS system should be stable in these operating points.

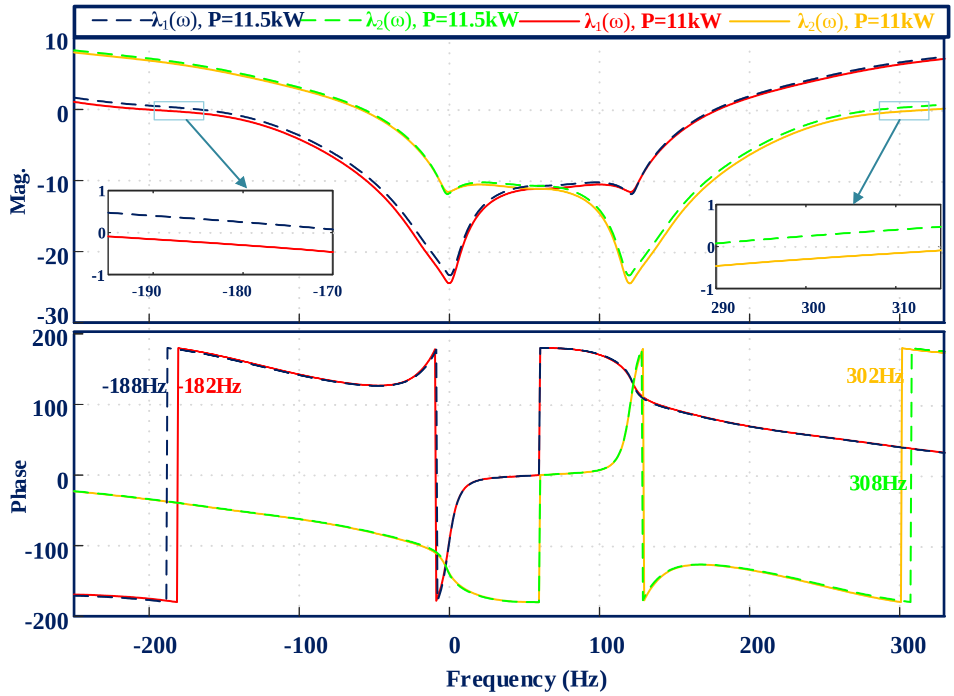

Figure 3-8 Frequency responses of eigenvalues of impedance ratio matrix G for AC grid-CPS system when CPS power generation is {P=11kW, Q=1kVar}, and {P=11.5kW, Q=1kVar}.

Figure 3-8 depicts frequency responses of eigenvalues of the matrix **G** for two other operating points of CPS which are {P=11kW, Q=1kVar} and {P=11.5kW, Q=1kVar}. Considering when CPS active power is P=11kW, the eigenvalues in candidate frequencies (λ_1:-182Hz or λ_2:302Hz) have a small positive gain margin. However, when CPS active power is P=11.5kW, the gain margins at the candidate frequencies (λ_1:-188Hz or λ_2:308Hz) become negative, which leads to instability of the AC grid-CPS system.

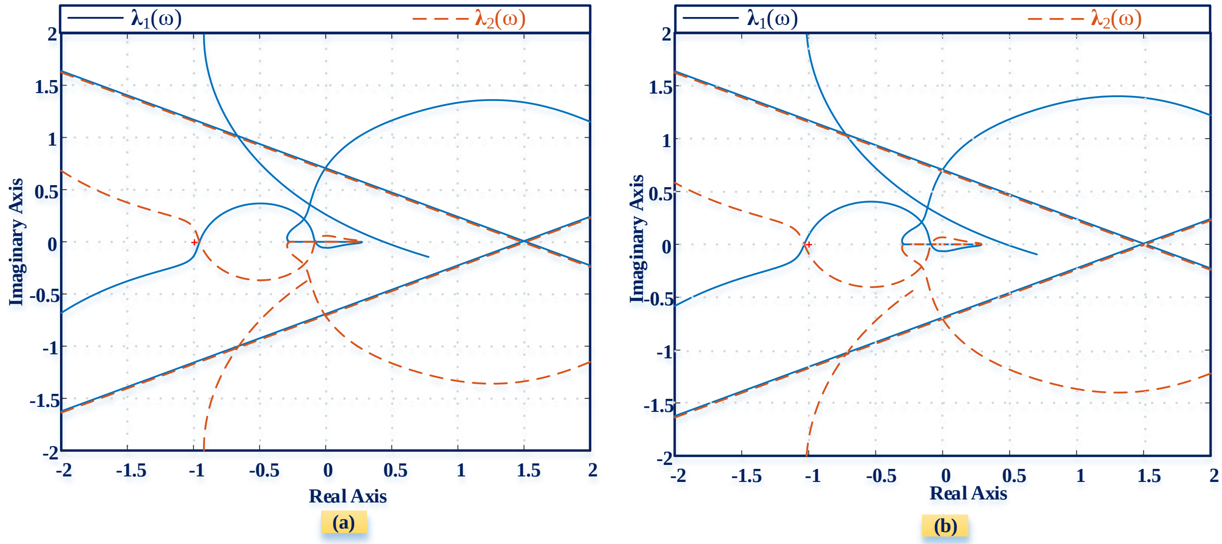

Figure 3-9 Nyquist plot of eigenvalues of matrix G for AC grid-CPS system: (a) CPS power generation is P=11kW, Q=1kVar; and (b) CPS power generation is P=11.5kW, Q=1kVar.

The Nyquist plots of eigenvalues of matrix **G** are shown in Figure 3-9 when CPS is operating at {P=11kW, Q=1kVar} and {P=11.5kW, Q=1kVar}. It can be observed that in the first operating point in Figure 3-9(a) the critical point is not encircled and the AC grid-CPS system is stable. In the second operating point in Figure 3-9(b) the critical point (-1+0j) is encircled, which follows with the analysis provided in Figure 3-8.

3.2 Simulation Studies of AC Grid-CPL/CPS System

In this subsection, the presented findings are validated by simulation studies. These studies are performed on the Opal-RT simulator, which closely emulates the experimental setup of the AC grid-CPL/CPS system by exploiting detailed switching models. Before discussing the operation of the AC grid-CPL/CPS system, the derived impedance of CPL is first validated. Figure 3-10 shows the frequency response of admittance of CPL obtained with two methods (modeling and frequency sweep) in the operating point {P=2kW, Q=0.5kVar}. It can be observed that both analyses have the same frequency responses. Therefore, the developed models for admittances of CPL/CPS are accurate.

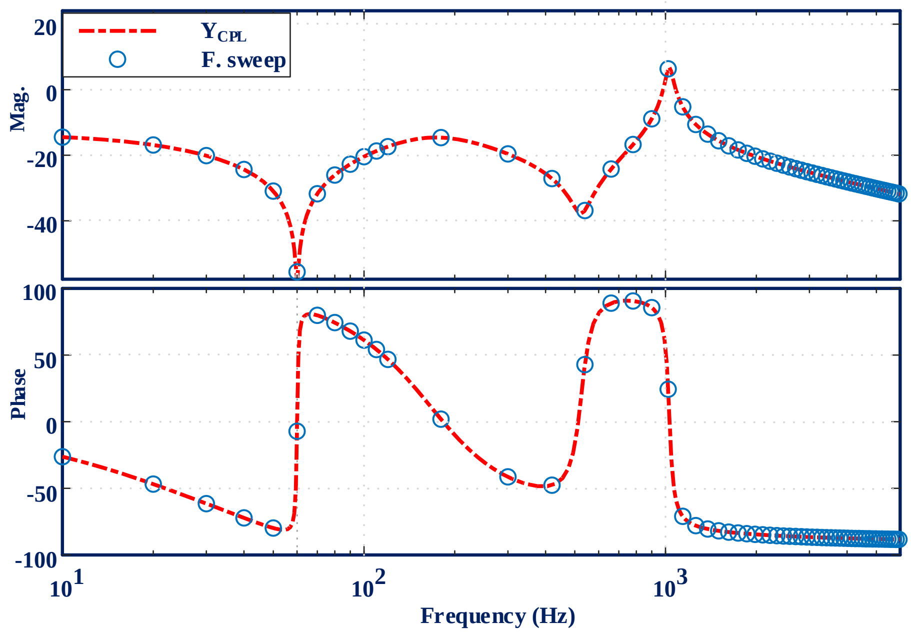

Figure 3-10 Frequency response of admittance of CPL.

In this subsection, the simulation results for the AC grid-CPL system in Figure 3-1(a) are presented. In the first simulation studies, CPL is consuming active and reactive power as provided in Figure 3-11, and the corresponding current and voltage of CPL are presented in Figure 3-12. The CPL starts up with consuming active power of P=2.5kW and reactive power of Q=1kVar from the AC grid. Then, at *t*= 0.2s, CPL active power is changed to P=6.5kW and small oscillations happen in the current and voltage of CPL, yet the system remains stable. Similarly, at *t*= 0.4s and *t*= 0.6s, the consumed active power from the AC grid is increased to 8kW and 9kW, respectively. It can be observed that the system response becomes more oscillatory and the damping takes a longer time. This dynamic behavior is due to small positive gain margins of eigenvalues at candidate frequencies which is reported in Figure 3-5. The FFT analysis of the CPL current is also presented in Figure 3-12(a), wherein it can be seen that the oscillations have components at the candidate frequencies (λ_1:-182Hz and λ_2:302Hz).

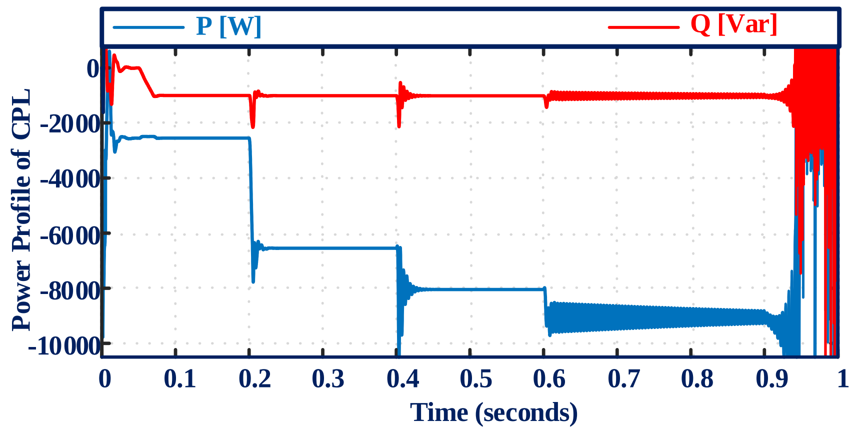

Figure 3-11 Active and reactive power consumption of CPL in AC grid-CPL system.

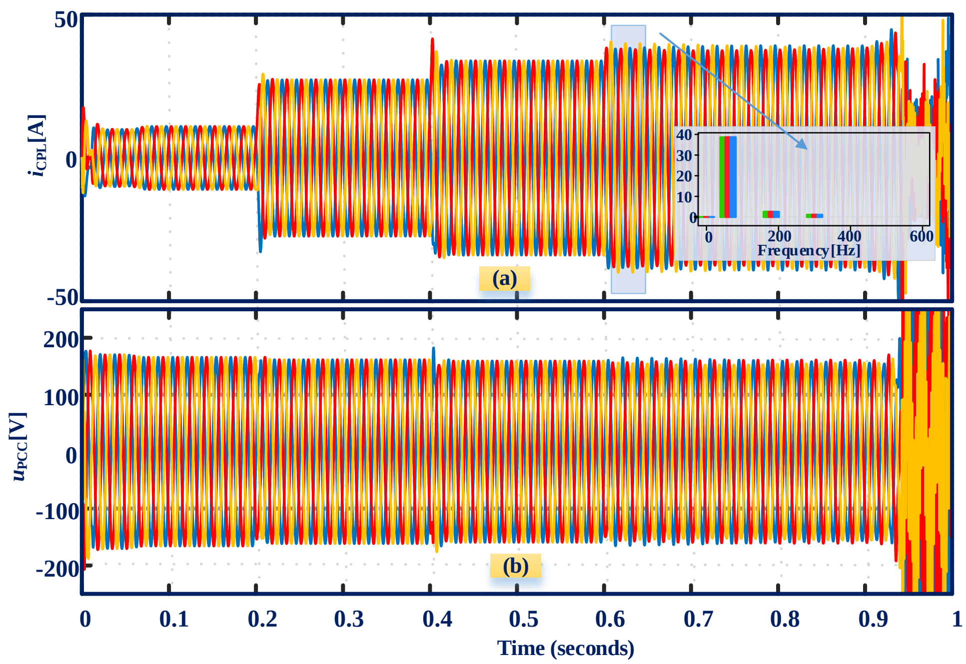

Figure 3-12 Voltage and current of CPL in AC grid-CPL system: (a) current of CPL; and (b) voltage of CPL.

At t= 0.9s, the CPL active power is increased to P= 9.5kW, and as predicted in Figure 3-5 and Figure 3-6(b), the AC grid-CPL system becomes destabilized. When the system is destabilized, large oscillations occur in the current and voltage at the PCC bus, as can be seen at the end of Figure 3-12.

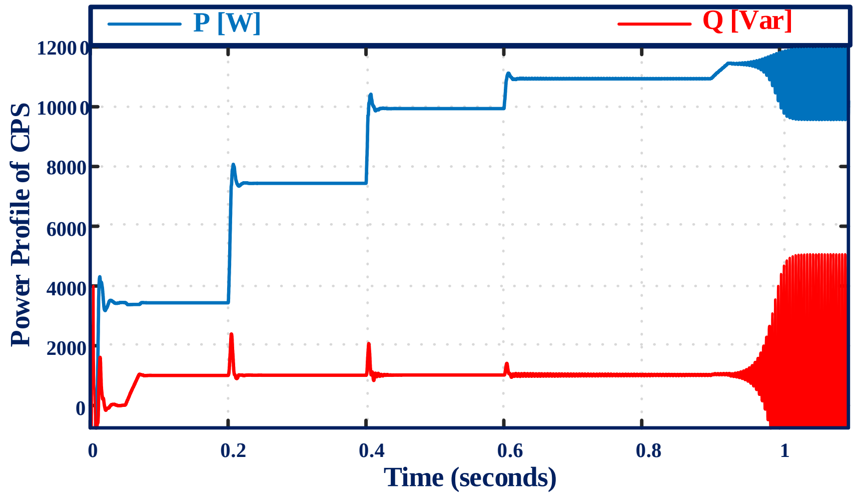

Figure 3-13 Active and reactive power consumption of CPS in AC grid-CPS system.

In the second simulation studies, CPS is generating active and reactive power as provided in Figure 3-13, and the respective current and voltage of CPS are presented in Figure 3-14. The CPS starts up with generating active power of P=3.5kW and reactive power of Q=1kVar. Then, at t= 0.2s, CPS active power is changed to P=7.5kW and the system remains stable. Similarly, at t= 0.4s and t= 0.6s, the generated active power of CPS is increased to 10kW and 11kW, respectively. At t= 0.9s CPS active power is increased to P=11.5kW and as predicted in Figure 3-8 and Figure 3-9(b) the AC grid-CPS system is destabilized. When the system is destabilized, sustained oscillations occur in the current and voltage of CPS and GCS. These oscillations, as provided in FFT analysis of the CPS current, have components specified as candidate frequencies (λ_1:-188Hz or λ_2:308Hz) in Figure 3-8.

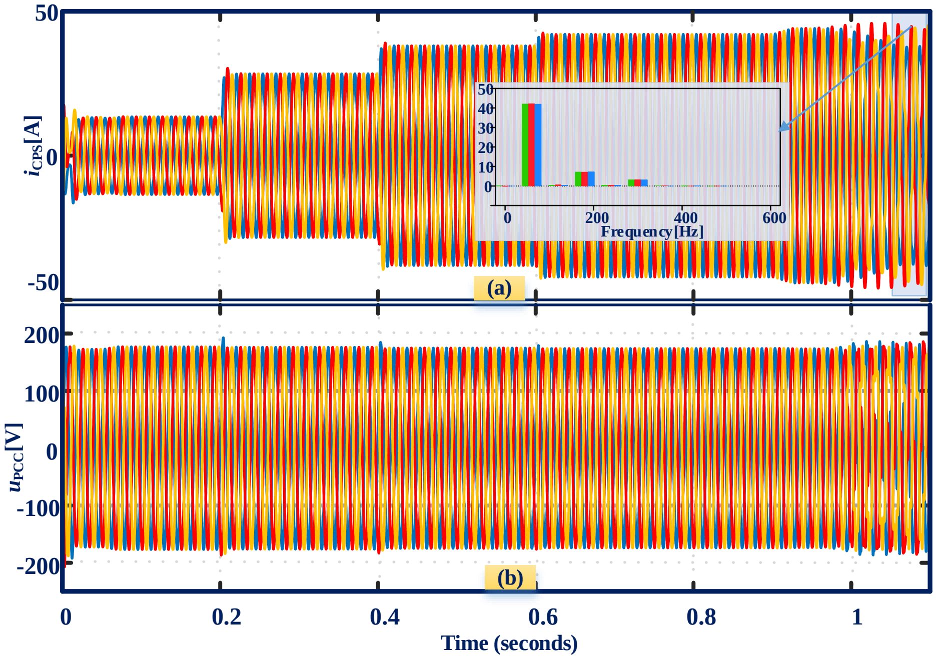

Figure 3-14 Voltage and current of CPS in AC grid-CPS system: (a) current of CPS; and (b) voltage of CPS.

3.3 Generic-controller Source-CPL/CPS System:

In this subsection, the dynamic characteristic of a CPL/CPS is investigated in different operating points while it is connected to a Generic-Controller-based Source (GCS). The structure of the considered three-phase AC system is shown in Figure 3-15. This architecture is similar to the one presented in Figure 3-1. The difference here is that CPL/CPS is connected to a GCS. The control system of GCS is shown in Figure 3-15(b). As it can be seen, a multi-loop approach is used to control the current and voltage of the inverter, and the control system is implemented in $\alpha\beta$ frame. GCS can work in both grid-connected and islanded operation of the considered system shown in Figure 3-15(a). Therein, we consider islanded operation mode in which inverter voltage $\mathbf{v}_{\mathrm{c},abc}$ is controlled with an outer control loop. The inner control loop is responsible for regulating the inverter's side current $\mathbf{i}_{1,abc}$. For the purpose of consistency in comparing different sources, the LC

filter of GCS is selected to be identical to LC filter of AC grid presented in Table 1.1. In what follows the small-signal modeling of GCS-CPL/CPS system is presented.

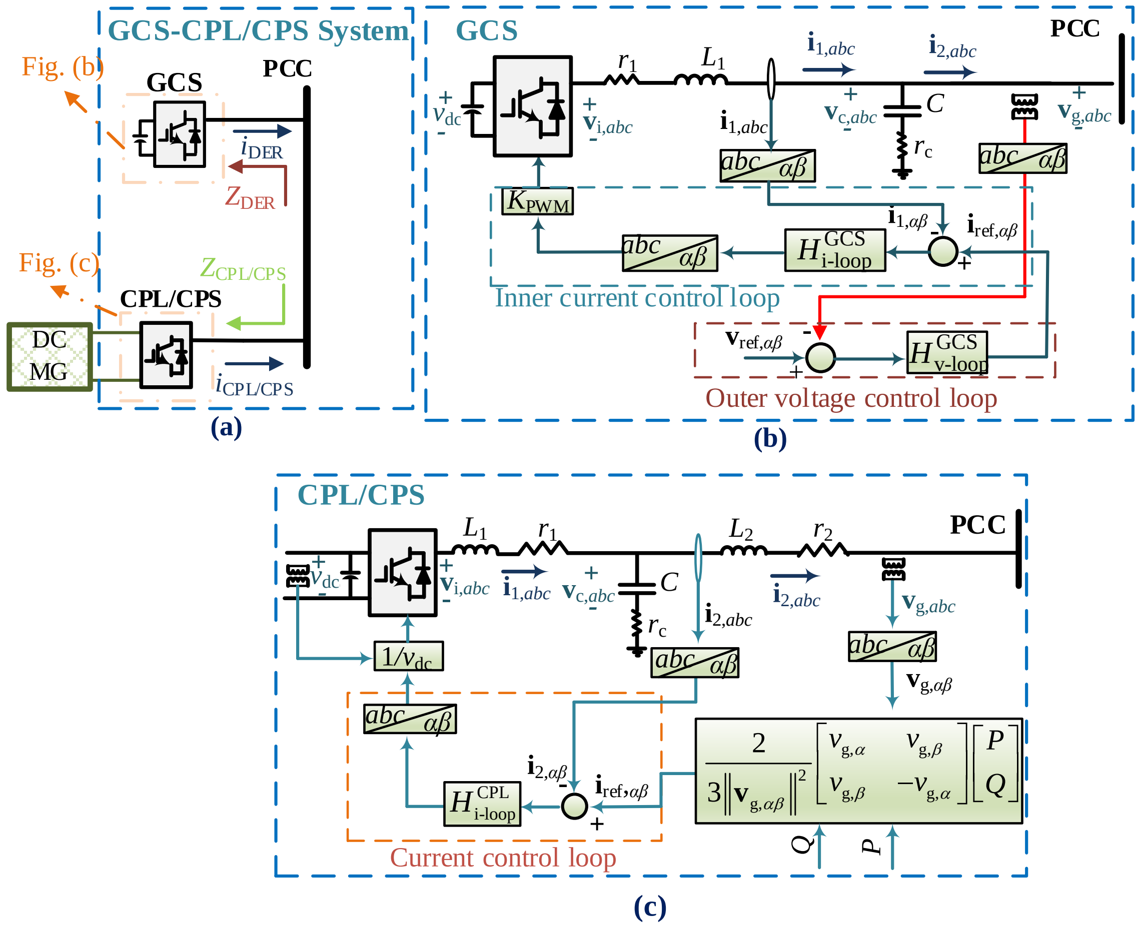

Figure 3-15 Considered AC system and its components: (a) high-level architecture of GCS-CPL/CPS system, (b) GCS and its control system, and (c) CPL/CPS and its control system.

3.3.1 Small-signal Modeling of GCS-CPL/CPS System Components

Since CPL/CPS circuit and its control circuit have not changed, the small-signal model developed for CPL/CPS in the previous subsection is still valid and can be used for stability analysis. Therein, we need to develop the small-signal model of GCS which is used for designing controllers $H^{GCS}_{i\text{-loop}}$

and $H_{\text{v-loop}}^{\text{GCS}}$. Assuming that the modulated voltage of the inverter can be represented by an average voltage $\mathbf{v}_{\text{i},abc}$, the open-loop circuit of GCS can be represented as Figure 3-16, and the state-space model of the open-loop GCS can be expressed as

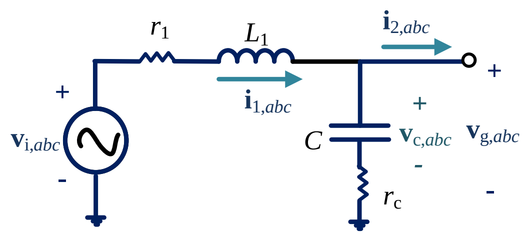

Figure 3-16 Open-loop circuit of GCS.

$$
\begin{aligned}
&\dot{\mathbf{x}}_{\text{LC},\alpha\beta} = \mathbf{A}_{\text{LC},\alpha\beta}\mathbf{x}_{\text{LC},\alpha\beta} + \mathbf{B}_{\text{i}}\mathbf{v}_{\text{i},\alpha\beta} + \mathbf{B}_{\text{o}}\mathbf{i}_{2,\alpha\beta}, \mathbf{x}_{\text{LC},\alpha\beta} = \begin{bmatrix} \mathbf{i}_{1,\alpha\beta} & \mathbf{v}_{\text{c},\alpha\beta} \end{bmatrix}^{\text{T}}, \\
&\mathbf{A}_{\text{LC},\alpha\beta} = \begin{bmatrix} a_{11} & 0 & a_{13} & 0 \\ 0 & a_{12} & 0 & a_{24} \\ a_{31} & 0 & 0 & 0 \\ 0 & a_{42} & 0 & 0 \end{bmatrix}, \begin{cases} a_{11} = a_{21} = -\dfrac{r_{\text{c}} + r_1}{L_1},\ a_{13} = a_{24} = -\dfrac{1}{L_1}, \\ a_{31} = a_{43} = \dfrac{1}{C} \end{cases}, \\
&\mathbf{B}_{\text{i}} = \begin{bmatrix} 1/L_1 & 0 & 0 & 0 \\ 0 & 1/L_1 & 0 & 0 \end{bmatrix}^{\text{T}}, \mathbf{B}_{\text{o}} = \begin{bmatrix} r_{\text{c}}/L_1 & 0 & -1/C & 0 \\ 0 & r_{\text{c}}/L_1 & 0 & -1/C \end{bmatrix}^{\text{T}}.
\end{aligned}
\tag{3.17}
$$

This state-space model can be used to derive transfer functions for the regulation of the inverter current $\mathbf{i}_{1,abc}$ and voltage $\mathbf{v}_{\text{c},abc}$. These transfer functions can be defined as,

$$\mathbf{G}_{\mathrm{vv}}(s)=\begin{bmatrix}\frac{\hat{v}_{\mathrm{c},\alpha}}{\hat{v}_{\mathrm{i},\alpha}} & \frac{\hat{v}_{\mathrm{c},\alpha}}{\hat{v}_{\mathrm{i},\beta}} \\ \frac{\hat{v}_{\mathrm{c},\beta}}{\hat{v}_{\mathrm{i},\alpha}} & \frac{\hat{v}_{\mathrm{c},\beta}}{\hat{v}_{\mathrm{i},\beta}}\end{bmatrix}=\begin{bmatrix}G_{\mathrm{vv},\alpha\alpha}(s) & 0 \\ 0 & G_{\mathrm{vv},\beta\beta}(s)\end{bmatrix},$$

$$\mathbf{G}_{\mathrm{vi}}(s)=\begin{bmatrix}\frac{\hat{i}_{1,\alpha}}{\hat{v}_{\mathrm{i},\alpha}} & \frac{\hat{i}_{1,\alpha}}{\hat{v}_{\mathrm{i},\beta}} \\ \frac{\hat{i}_{1,\beta}}{\hat{v}_{\mathrm{i},\alpha}} & \frac{\hat{i}_{1,\beta}}{\hat{v}_{\mathrm{i},\beta}}\end{bmatrix}=\begin{bmatrix}G_{\mathrm{vi},\alpha\alpha}(s) & 0 \\ 0 & G_{\mathrm{vi},\beta\beta}(s)\end{bmatrix}. \quad \textbf{(3.18)}$$

The matrices $\mathbf{G}_{\mathrm{vv}}(s)$ and $\mathbf{G}_{\mathrm{vi}}(s)$ will be diagonal and symmetric ($G_{\mathrm{vi},\alpha\alpha}(s)= G_{\mathrm{vi},\beta\beta}(s)$ and $G_{\mathrm{vv},\alpha\alpha}(s)=G_{\mathrm{vv},\beta\beta}(s)$), and the elements are obtained using a numerical approach. Similar to CPL/CPS control schemes, since there is no coupling between $\alpha\beta$ components in the developed state-space model, the inverter side current can be independently controlled using the same controller $H_{\text{i-loop}}^{\text{GCS}}$ in both axes. The controller $H_{\text{i-loop}}^{\text{GCS}}$ is designed in a way that the open-loop gain of the current loop defined as

$$T_{\mathrm{si},\alpha\alpha}=T_{\mathrm{si},\beta\beta}=G_{\mathrm{vi},\alpha\alpha}\times H_{\text{i-loop}}^{\text{GCS}}\times K_{\mathrm{pwm}}, \quad \textbf{(3.19)}$$

has a positive phase margin. After designing the current controller $H_{\text{i-loop}}^{\text{GCS}}$, the closed-loop model of the inverter $G_{\mathrm{vc},\alpha\beta}$ with the inner current controller can be obtained. This closed-loop model is as

$$G_{\mathrm{vc},\alpha\alpha}=G_{\mathrm{vc},\beta\beta}=\frac{T_{\mathrm{si},\alpha\alpha}}{1+T_{\mathrm{si},\alpha\alpha}}\times G_{\mathrm{vv},\alpha\alpha}, \quad \textbf{(3.20)}$$

and is used to design the controller $H_{\text{v-loop}}^{\text{GCS}}$ in the outer voltage control loop. The controller $H_{\text{v-loop}}^{\text{GCS}}$ should provide a positive phase margin for the open-loop gain of the outer loop defined as

$$T_{\mathrm{sv},\alpha\alpha}=T_{\mathrm{sv},\beta\beta}=G_{\mathrm{vc},\alpha\alpha}\times H_{\text{v-loop}}^{\text{GCS}}. \quad \textbf{(3.21)}$$

The coefficients of the designed controller $H_{\text{i-loop}}^{\text{GCS}}$ and $H_{\text{v-loop}}^{\text{GCS}}$ in form of $H=(a_2s^2+a_1s+a_0)/(b_2s^2+b_1s+b_0)$ are provided Table 3.3. The frequency responses of the current loop and voltage loop of GCS are shown in Figure 3-17. As it can be seen, both current loop and voltage loop ($T_{\text{si},\alpha\alpha}$, $T_{\text{sv},\alpha\alpha}$) have positive phase margins indicating the stability of GCS.

	a_0	a_1	a_2	b_0	b_1	b_2
$H_{\text{v-loop}}^{\text{GCS}}$	1.4×10^4	50.35	0.1	1.42×10^5	6	1
$H_{\text{i-loop}}^{\text{GCS}}$	7208	25.66	0.05	1.42×10^5	6	1

Table 3.3 Coefficients of GCS controllers.

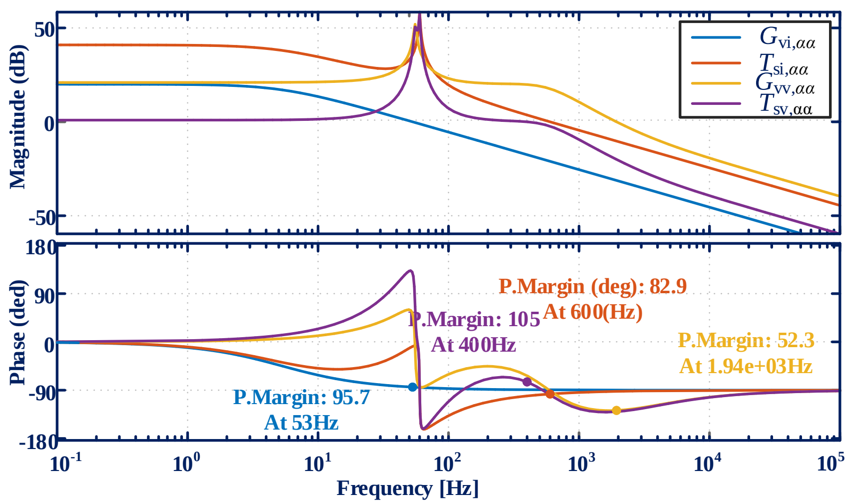

Figure 3-17. Frequency responses of the current loop and voltage loop of GCS.

After designing the outer voltage controlled-loop, the closed-loop state-space model of GCS can be obtained. Assuming that the state-space model of the current and voltage controller ($H_{\text{i-loop}}^{\text{GCS}}$ and $H_{\text{v-loop}}^{\text{GCS}}$) can be expressed as

$$H_{\text{i-loop}}^{\text{GCS}} \rightarrow \begin{cases} \dot{\mathbf{x}}_{\text{i-loop},\alpha\beta} = \mathbf{A}_{\text{c}}\mathbf{x}_{\text{i-loop},\alpha\beta} + \mathbf{B}_{\text{c}}\mathbf{u}_{\text{i-loop},\alpha\beta} \\ \mathbf{y}_{\text{i-loop},\alpha\beta} = \mathbf{C}_{\text{c}}\mathbf{x}_{\text{i-loop},\alpha\beta} + \mathbf{D}_{\text{c}}\mathbf{u}_{\text{i-loop},\alpha\beta} \end{cases}, \tag{3.22}$$

$$H_{\text{v-loop}}^{\text{GCS}} \rightarrow \begin{cases} \dot{\mathbf{x}}_{\text{v-loop},\alpha\beta} = \mathbf{A}_{\text{v}}\mathbf{x}_{\text{v-loop},\alpha\beta} + \mathbf{B}_{\text{v}}\mathbf{u}_{\text{v-loop},\alpha\beta} \\ \mathbf{y}_{\text{v-loop},\alpha\beta} = \mathbf{C}_{\text{v}}\mathbf{x}_{\text{v-loop},\alpha\beta} + \mathbf{D}_{\text{v}}\mathbf{u}_{\text{v-loop},\alpha\beta} \end{cases},$$

the complete state-space model of the GCS is as

$$\dot{\mathbf{x}}_{\text{GCS}} = \mathbf{A}_{\text{GCS}}\mathbf{x}_{\text{GCS}} + \mathbf{B}_{\text{GCS}}\mathbf{v}_{\text{ref},\alpha\beta} + \mathbf{M}_{\text{GCS}}\mathbf{i}_{2,\alpha\beta}, \ \mathbf{x}_{\text{GCS}} = [\mathbf{x}_{\text{LC},\alpha\beta} \quad \mathbf{x}_{\text{i-loop},\alpha\beta} \quad \mathbf{x}_{\text{v-loop},\alpha\beta}]^{\text{T}},$$

$$\mathbf{A}_{\text{GCS}} = \begin{bmatrix} \mathbf{A}_{\text{LC},\alpha\beta} - \mathbf{B}_{\text{i}}\mathbf{D}_{\text{c}}(\mathbf{D}_{\text{v}}\mathbf{S}_2 + \mathbf{S}_1) & \mathbf{B}_{\text{i}}\mathbf{C}_{\text{c}} & \mathbf{B}_{\text{i}}\mathbf{D}_{\text{c}}\mathbf{C}_{\text{v}} \\ -\mathbf{B}_{\text{c}}(\mathbf{D}_{\text{v}}\mathbf{S}_2 + \mathbf{S}_1) & \mathbf{A}_{\text{c}} & \mathbf{B}_{\text{c}}\mathbf{C}_{\text{v}} \\ -\mathbf{B}_{\text{v}}\mathbf{S}_2 & \mathbf{0} & \mathbf{A}_{\text{v}} \end{bmatrix}, \mathbf{B}_{\text{GCS}} = [\mathbf{B}_{\text{i}}\mathbf{D}_{\text{c}}\mathbf{D}_{\text{v}} \quad \mathbf{B}_{\text{c}}\mathbf{D}_{\text{v}} \quad \mathbf{B}_{\text{v}}]^{\text{T}}, \tag{3.23}$$

$$\mathbf{M}_{\text{GCS}} = [\mathbf{B}_{\text{o}} \quad \mathbf{0} \quad \mathbf{0}]^{\text{T}}, \ \mathbf{S}_1 = \begin{bmatrix} 1 & 0 & 0 & 0 & 0 & 0 \\ 0 & 1 & 0 & 0 & 0 & 0 \end{bmatrix}, \mathbf{S}_2 = \begin{bmatrix} 0 & 0 & 1 & 0 & 0 & 0 \\ 0 & 0 & 0 & 1 & 0 & 0 \end{bmatrix},$$

where, $\mathbf{v}_{\text{ref},\alpha\beta}$ is the reference of the outer voltage control loop. This developed state-space model can be used to derive the output closed-loop of impedance of the GCS, which will have the following generic form as

$$\mathbf{Z}_{\text{GCS},\alpha\beta}(s) = \begin{bmatrix} \dfrac{-\hat{v}_{\text{g},\alpha}}{\hat{i}_{2,\alpha}} & \dfrac{-\hat{v}_{\text{g},\alpha}}{\hat{i}_{2,\beta}} \\ \dfrac{-\hat{v}_{\text{g},\beta}}{\hat{i}_{2,\alpha}} & \dfrac{-\hat{v}_{\text{g},\beta}}{\hat{i}_{2,\beta}} \end{bmatrix} = \begin{bmatrix} Z_{\text{GCS},\alpha\alpha}(s) & 0 \\ 0 & Z_{\text{GCS},\beta\beta}(s) \end{bmatrix}. \tag{3.24}$$

Similarly, the matrix impedance $\mathbf{Z}_{\text{GCS},\alpha\beta}(s)$ is diagonal and symmetric. The diagonal elements are high-order transfer functions in the form of $Z_{\text{GCS},\alpha\alpha}(s) = Z_{\text{GCS},\beta\beta}(s) = N(s)/M(s),$ which are obtained using a numerical approach

3.3.2 Stability Analysis of GCS-CPL/CPS System

The stability of the GCS-CPL/CPS system in Figure 3-15 can be assessed by similar impedance-based stability analysis and before doing so, the impedances of GCS and CPL/CPS should be transformed to the same coordinate. Similar impedance-admittance product matrix **G**(*s*) can be defined as

$$\mathbf{G}(s) = \mathbf{Z}^{\mathrm{c}}_{\mathrm{GSC},\alpha\beta}(s)\mathbf{Y}^{\mathrm{c}}_{\mathrm{CPL},\alpha\beta}(s), \tag{3.25}$$

where $\mathbf{Z}^{\mathrm{c}}_{\mathrm{GSC},\alpha\beta}(s)$ is the complex impedance matrix of GCS in complex $\alpha\beta$ frame obtained from

$$\mathbf{Z}^{\mathrm{c}}_{\mathrm{GSC},\alpha\beta}(s) = \begin{bmatrix} Z_{\mathrm{GCS},\alpha\alpha}(s) & 0 \\ 0 & Z_{\mathrm{GCS},\beta\beta}(s-2j\omega_1) \end{bmatrix}. \tag{3.26}$$

The stability of GCS-CPL/CPS system can be assessed by plotting frequency responses of eigenvalues of impedance ratio matrix **G**. The frequency responses of impedance ration matrix **G** is shown in Figure 3-18 when CPL power consumption is as {P=6kW, Q=1kVar}, and {P=6.5kW, Q=1kVar}. Different candidate frequencies (λ_1:30Hz, 31Hz and λ_2:89Hz, 90Hz) can be found in both operating points. The gain margins in all candidate frequencies are positive, hence the considered system is stable in these two operation points of CPL.

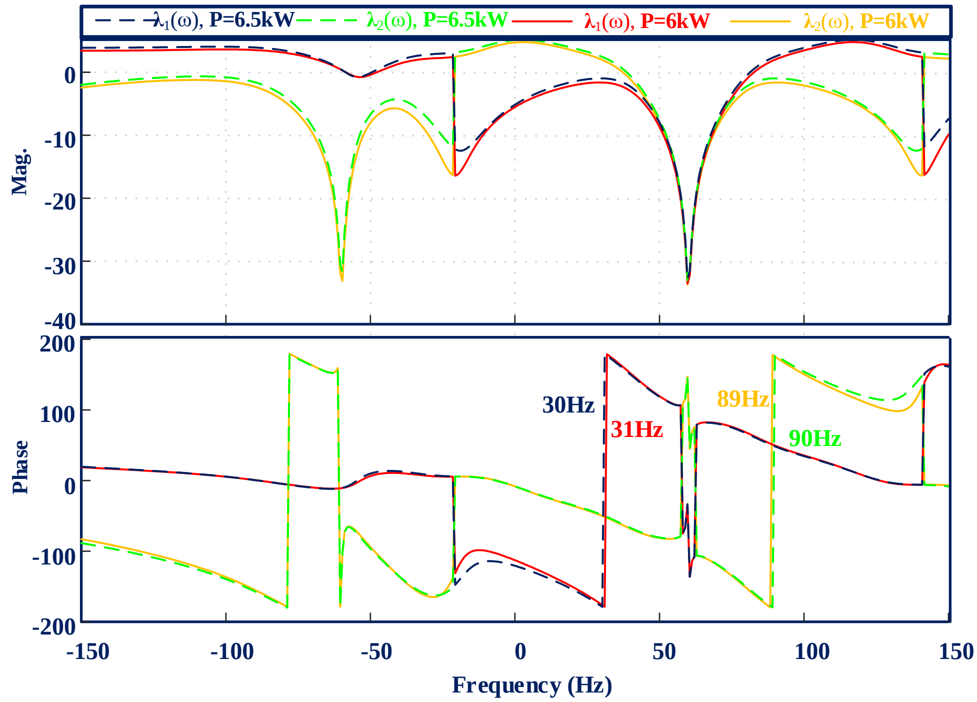

Figure 3-18 Frequency responses of eigenvalues of impedance ratio matrix G for GCS-CPL system when CPL power consumption is {P=6kW, Q=1kVar}, and {P=6.5kW, Q=1kVar}.

Figure 3-19 shows the frequency responses of impedance ratio matrix **G** when CPL power consumption is {P=7kW, Q=1kVar}, and {P=7.5kW, Q=1kVar}. When CPL is consuming P=7kW of active power, the frequency responses of eigenvalues have small positive gains margin at the candidate frequencies (λ_1:30Hz and λ_2:90Hz). Therefore, the considered GCS-CPL system is stable at this operating point. Nonetheless, the system becomes unstable when the active power consumption of CPL is increased to P=7.5kW. This is due to the negative gain margin of eigenvalues of matrix **G** at candidate frequencies (λ_1:29Hz and λ_2:91Hz).

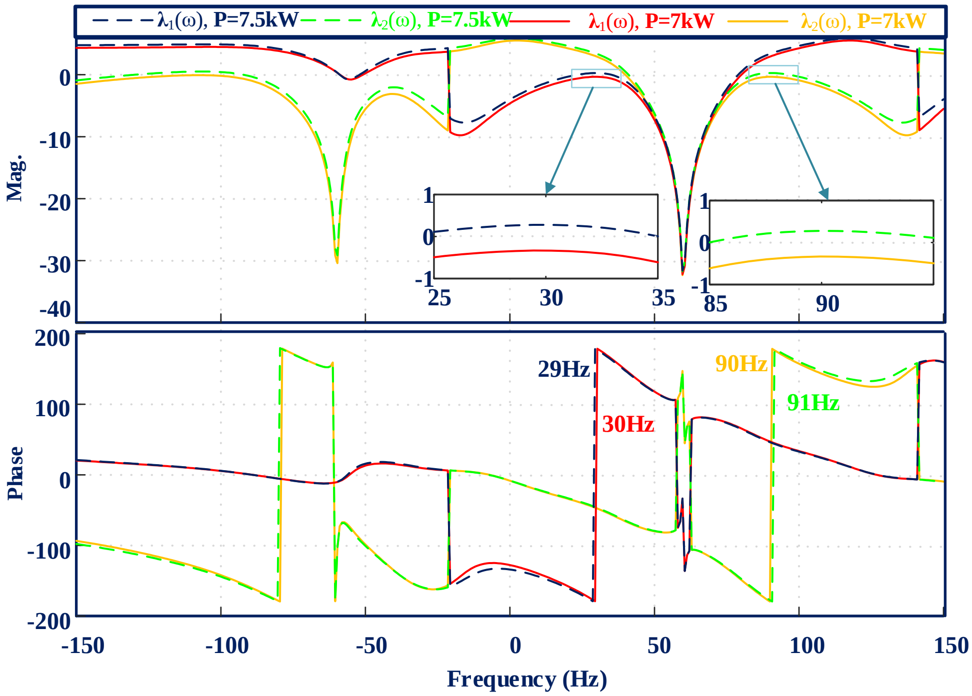

Figure 3-19 Frequency responses of eigenvalues of impedance ratio matrix G for GCS-CPL system when CPL power consumption is {P=7kW, Q=1kVar}, and {P=7.5kW, Q=1kVar}.

The Nyquist plots of eigenvalues of matrix **G** are shown in Figure 3-20. Unlike the operating point P=7kW, the Nyquist plot encircles the critical point when CPL is consuming P=7.5kW, which indicates the instability of the GCS-CPL system. This finding is independently reported in Figure 3-19.

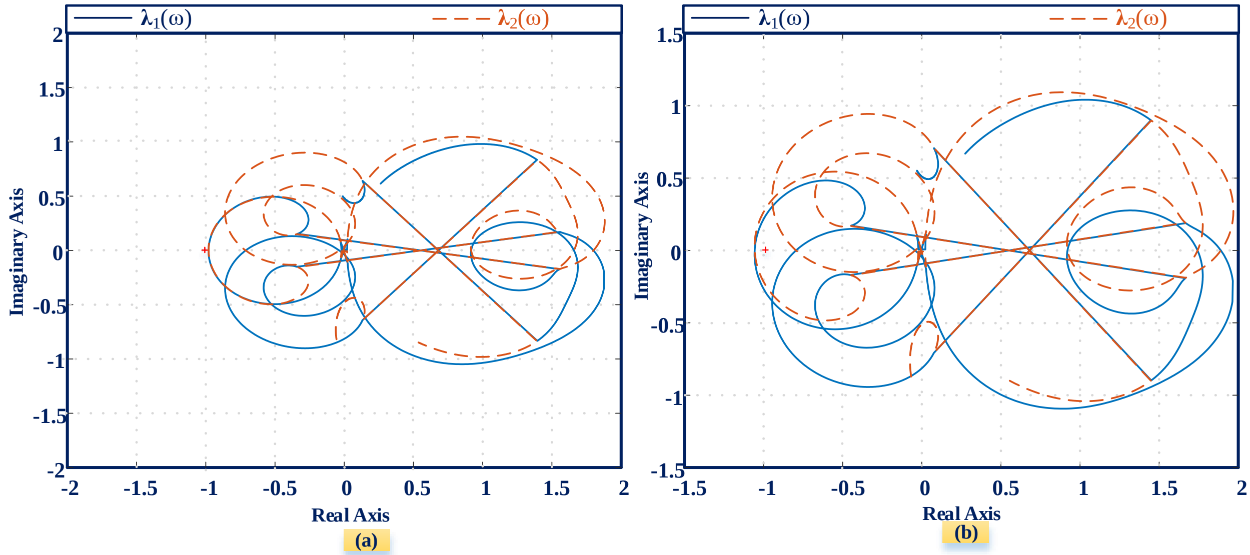

Figure 3-20 Nyquist plot of eigenvalues of matrix G for GCS-CPL system when: (a) CPL power consumption is {P=7kW, Q=1kVar}; and (b) CPL power consumption is {P=7.5kW, Q=1kVar}.

The frequency responses of eigenvalues of matrix **G** when CPS power generation is {P=7.5kW, Q=1kVar}, and {P=8kW, Q=1kVar} are shown in Figure 3-21. As it can be seen, the gain margins of eigenvalues at all candidate frequencies (λ_1:30Hz and λ_2:91Hz) are positive when CPS is generating active power P=7.5kW. Therefore, the considered GCS-CPS system is stable at this operating point. Nonetheless, the system becomes unstable when CPS active power is increased to P=8kW. This is due to the negative gain margin of eigenvalues at candidate frequencies (λ_1:29Hz and λ_2:91Hz). The Nyquist plots of eigenvalues of matrix **G** are shown in Figure 3-22 confirming that the GCS-CPS system becomes unstable when the active power generation of CPS is increased from P=7.5kW to P=8kW.

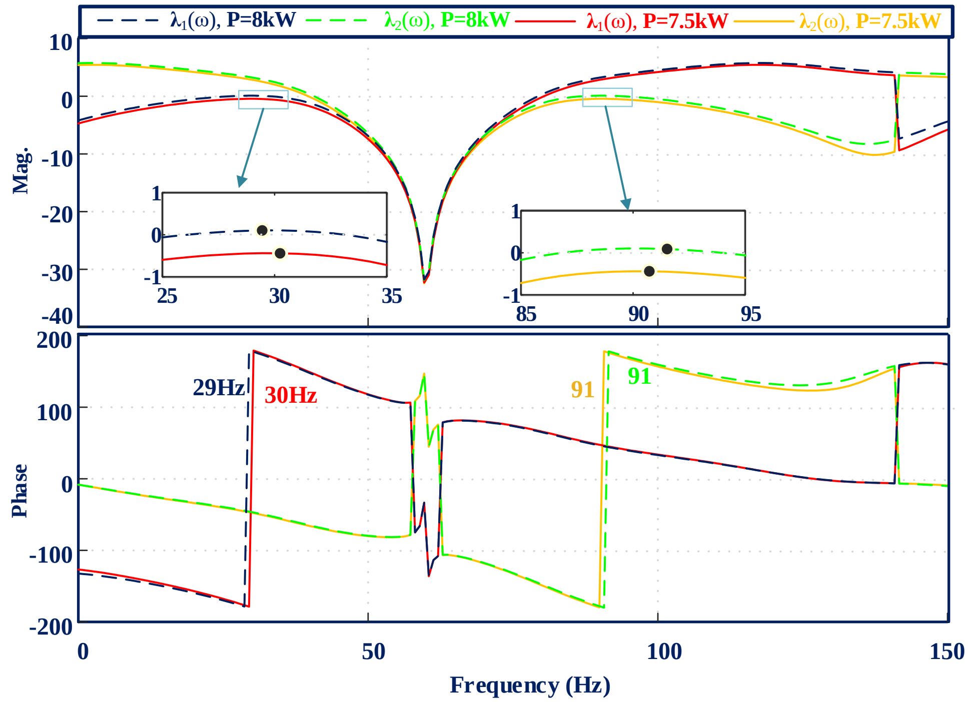

Figure 3-21 Frequency responses of eigenvalues of impedance ratio matrix G for GCS-CPS system when CPS power generation is {P=7.5kW, Q=1kVar}, and {P=8kW, Q=1kVar}.

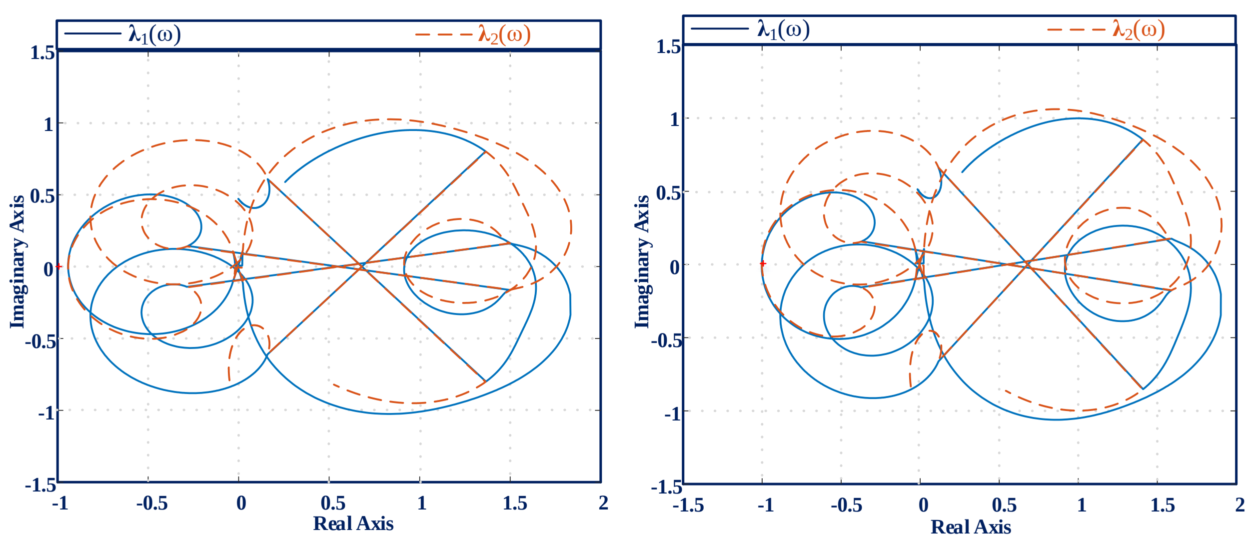

Figure 3-22 Nyquist plot of eigenvalues of matrix G for GCS-CPS system when: (a) CPS power generation is {P=7.5kW, Q=1kVar}; and (b) CPS power generation is {P=8kW, Q=1kVar}.

3.4 Simulation Studies

In this subsection, the presented findings are validated by real-time simulation studies on the Opal-RT simulator. First, the derived impedance of GCS is validated. Figure 3-23 shows the frequency responses of GCS admittances obtained with the developed model and frequency sweep analysis. It can be seen that the obtained admittance from frequency sweep analysis perfectly matches with developed admittance model. Therefore, the developed model for the admittance of GCS is accurate.

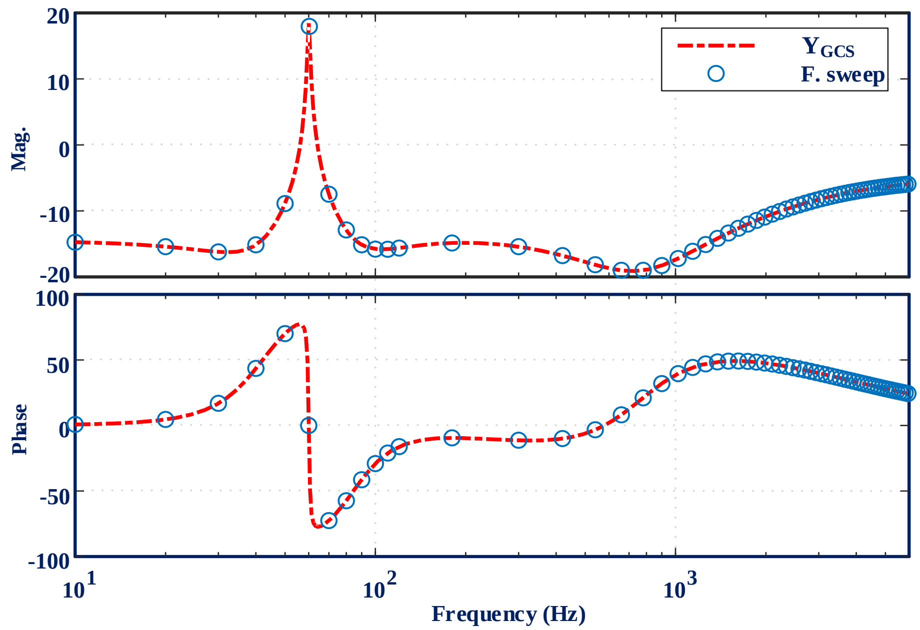

Figure 3-23 Frequency response of admittance of GCS.

Here, the simulation results for the GCS-CPL system in Figure 3-15 are presented. The CPL power consumption profile is shown in Figure 3-24, and the corresponding currents and voltages are presented in Figure 3-25. The CPL starts up with consuming active power of P=3kW and reactive power of Q=1kVar from the GCS. At t = 0.2s, the CPL active power is changed to P=5kW, which is followed by small oscillations. Next, the CPL real power consumption is further increased at *t*= 0.4s and *t*= 0.6s, to 6kW and 7kW, respectively. As it can be observed in Figure 3-24 and Figure 3-25, the dynamic response of GCS-CPL system becomes more oscillatory with less damping. This dynamic behavior is consistent with the small positive gain margins of eigenvalues at candidate frequencies (90Hz and 30 Hz) presented in Figure 3-19. The FFT analysis of the CPL current during the highlighted time window is presented in Figure 3-25(a). As it can be seen, the oscillations include the candidate frequencies (91Hz, 29Hz) identified in Figure 3-19.

At *t*= 0.9s, the CPL active power is further increased to P=7.5kW. As predicted in Figure 3-19 and Figure 3-20(b), at this power level, the GCS-CPL system becomes destabilized, which can be seen as in Figure 3-24 and Figure 3-25, and as a result, large and increasing oscillations of the current and voltage occur at the PCC bus where the CPL is connected.

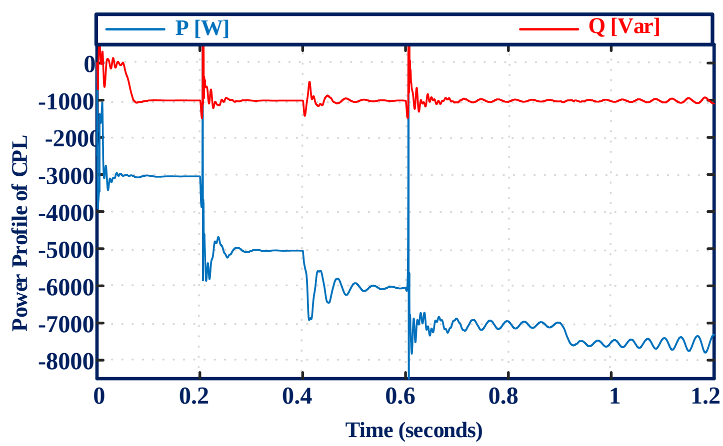

Figure 3-24 Active and reactive power consumption of CPL in GCS-CPL system.

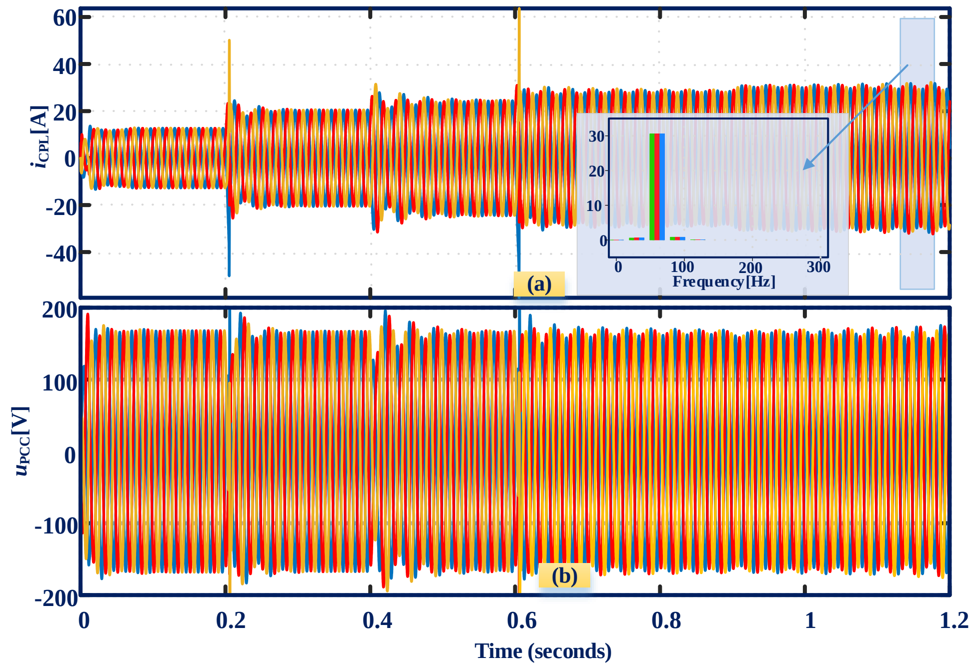

Figure 3-25 Voltage and current of CPL in GCS-CPL system: (a) current of CPL; and (b) voltage of CPL.

In the second simulation studies, CPS is generating active and reactive power as provided in Figure 3-26, and the corresponding current and voltage of CPS are presented in Figure 3-27. The CPS starts up with generating active power of P=3.5kW and reactive power of Q=1kVar. Then, at *t*= 0.2s, CPS active power is changed to P=5.5kW and the system remains stable. Similarly, at *t*= 0.4s and *t*= 0.6s, the generated active power of CPS is increased to 6.5kW and 7.5kW, respectively. At *t*= 0.9s CPS active power is increased to P=8kW and as predicted in Figure 3-21 and Figure 3-22(b) the GCS-CPS system is destabilized.

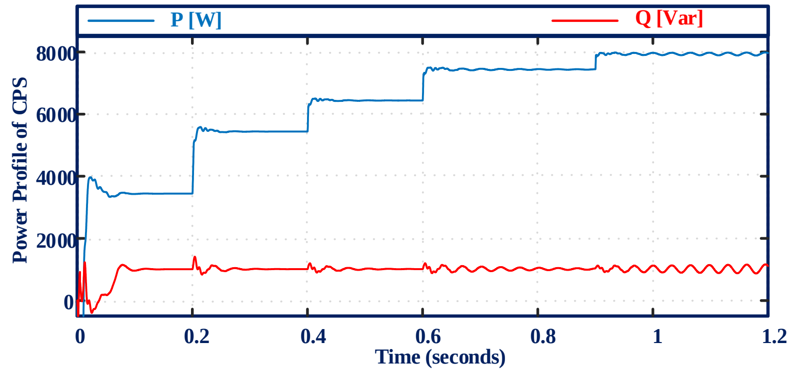

Figure 3-26 Active and reactive power generation of CPS in GCS-CPS system.

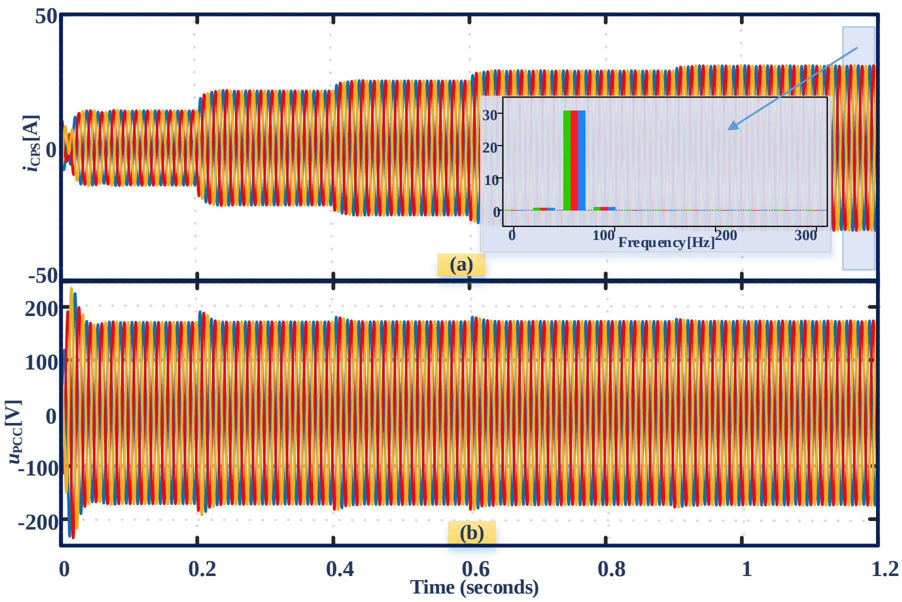

Figure 3-27 Voltage and current of CPS in GCS-CPS system: (a) current of CPS; and (b) voltage of CPS.

3.5 Summary

In this chapter, the dynamic characteristics of CPL/CPS are discussed thoroughly in two settings. In the first system, CPL/CPS is connected to an AC grid and in the second case, it is connected to a generic-controlled source (GCS). To compare the two cases, the *LC* filter parameters of the AC grid and GCS are kept identical. It was shown that for both cases, if the power consumption/generation of CPS/CPL is increased, the system dynamic behavior deteriorates and it can be destabilized. However, the AC grid-CPL/CPS the system is destabilized at higher power levels.

Chapter 4: Operation and Stability of Virtual Oscillator Based Resources

This chapter investigates the operation and stability of a newly proposed control scheme of resources in microgrids. This control scheme is known as “Virtual Oscillator” and mimics the conventional droop characteristic in synchronous generators [23], [24]. Virtual oscillator control schemes can be implemented into digital controllers to represent non-linear dynamics of dead-zone or Vanderpol oscillators[21], [24]. In the islanded operation of microgrids, it can synchronize resources and provide power-sharing among resources without communication links. The discussed virtual oscillator control scheme in this chapter can work in both grid-connected and islanded operation of microgrids [25]. Moreover, it provides lower harmonic distortion compared to similar schemes as [25]. In what follows the operation principles of this control scheme are discussed and then the stability characteristics of this control scheme are assessed while feeding a constant power load.

4.1 Operation Principles and Design of Virtual Oscillator Based Resources.

In this subsection, the design and operation of Virtual-Oscillator controlled Source (VOS) are discussed thoroughly. This can provide insight on stability analysis of VOS which is presented in the next subsection. Figure 4-1 shows the considered control scheme of VOS and its power electronics circuit. For simplicity, the conventional two-level three-phase inverter is considered here as the topology of power electronic circuit.

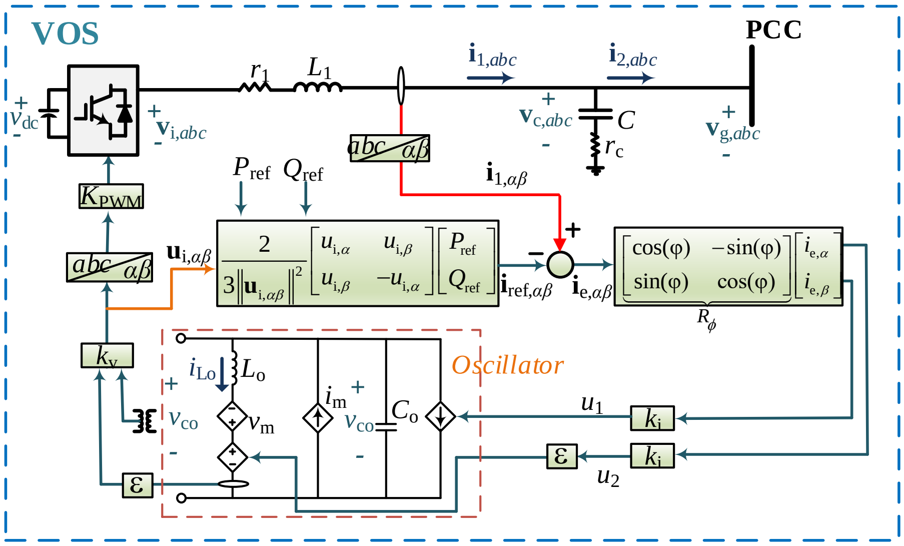

Figure 4-1 Circuit and control scheme of VOS.

An LC filter is equipped in the circuit to attenuate switching harmonics. The control scheme includes an outer loop that determines the reference current $i_{ref,\alpha\beta}$ for the inner loop. The matrix R_φ in the inner loops affects the VOS's active and reactive power regulation [25]. The oscillator circuit includes passive components L_o and C_o, a voltage source v_m and a current source i_m. These sources are dependent on the states of the oscillator $\mathbf{x}=[x_1, x_2]^T=[v_{co}, \varepsilon i_{Lo}]$, where ε is defined as $\varepsilon \coloneqq \sqrt{L_o/C_o}$. The controlled sources are expressed as

$$v_m = \frac{\zeta}{\omega_{nom}}(2X_{nom}^2 - v_{co}^2 - (\varepsilon i_{Lo})^2)\varepsilon i_{Lo}, i_m = \frac{\zeta}{\varepsilon\omega_{nom}}(2X_{nom}^2 - v_{co}^2 - (\varepsilon i_{Lo})^2)v_{co}, \tag{4.1}$$

where X_{nom} and ζ are the coefficients affecting the convergence to the steady-state point, and ω_{nom} is the nominal angular frequency. The circuit also includes voltage and current scaling factors k_v and k_i. It can be shown that for $\varphi = \pi/2$rad, the active and reactive power of VOS can be independently controlled by adjusting the frequency and voltage magnitude, respectively. Therefore, for $\varphi = \pi/2$rad, the steady-state voltage and frequency of VOS are derived from

$$V = \frac{V_{\text{nom}}}{\sqrt{2}}\left[1+\sqrt{1-\frac{2k_{\text{i}}k_{\text{v}}^3}{3C\zeta V_{\text{nom}}^4}(Q-Q_{\text{ref}})}\right]^{\frac{1}{2}},\ \omega = \omega_{\text{nom}} - \frac{k_{\text{i}}k_{\text{v}}}{3CV^2}(P-P_{\text{ref}}). \tag{4.2}$$

The above equation shows in grid-connected mode P=P_{ref} since VOS angular frequency ω is locked to grid angular frequency ω_{nom}. The considered control scheme of VOS has different parameters (k_{v}, k_{i}, L_{o}, etc.) which should be designed properly. These parameters are dependent on nominal phase voltage V_{nom}, minimum permissible per unit phase voltage $V_{\text{min,p.u}}$, nominal apparent power S_{nom}, power tracking time constant τ, as well as nominal angular frequency ω_{nom}. First, the voltage and current scaling factors k_{v} and k_{i} are selected as

$$k_{\text{v}} = V_{\text{nom}},\ k_{\text{i}} = 3\frac{V_{\text{nom}}}{S_{\text{nom}}}. \tag{4.3}$$

Then, the rest of the parameters are designed in a way that the following constraints

$$C\zeta = \frac{\sqrt{2}}{4(V_{\text{min,p.u}}^2 - V_{\text{min,p.u}}^4)},\ \frac{1}{\sqrt{2}V_{\text{min,p.u}}^2\left|\Delta\omega\right|_{\text{max}}} \le C \le 3\tau\frac{V_{\text{nom}}^2}{XS_{\text{nom}}},\ \omega = \frac{1}{\sqrt{L_{\text{o}}C_{\text{o}}}}, \tag{4.4}$$

where X represents the inductance of the output filter of VOS [25]. After designing VOS, we can analyze its dynamic characteristic in different systems. In what follows the dynamic characteristics of VOS are assessed while connecting to a CPL system.

4.2 VOS-CPL System

In this subsection, we investigate the dynamic characteristics of the proposed control scheme while feeding a CPL. The structure of a VOS-CPL system is shown in Figure 4-2 and the parameters of the system are provided in Table 4.1. It should be mentioned that the parameters of VOS are selected based on the design procedure discussed in the previous subsection. The circuit and control system of CPL is kept constant and explained in the previous chapter. Before performing stability analysis, small-signal models of the components in the VOS-CPL system in Figure 4-2(a) should be obtained.

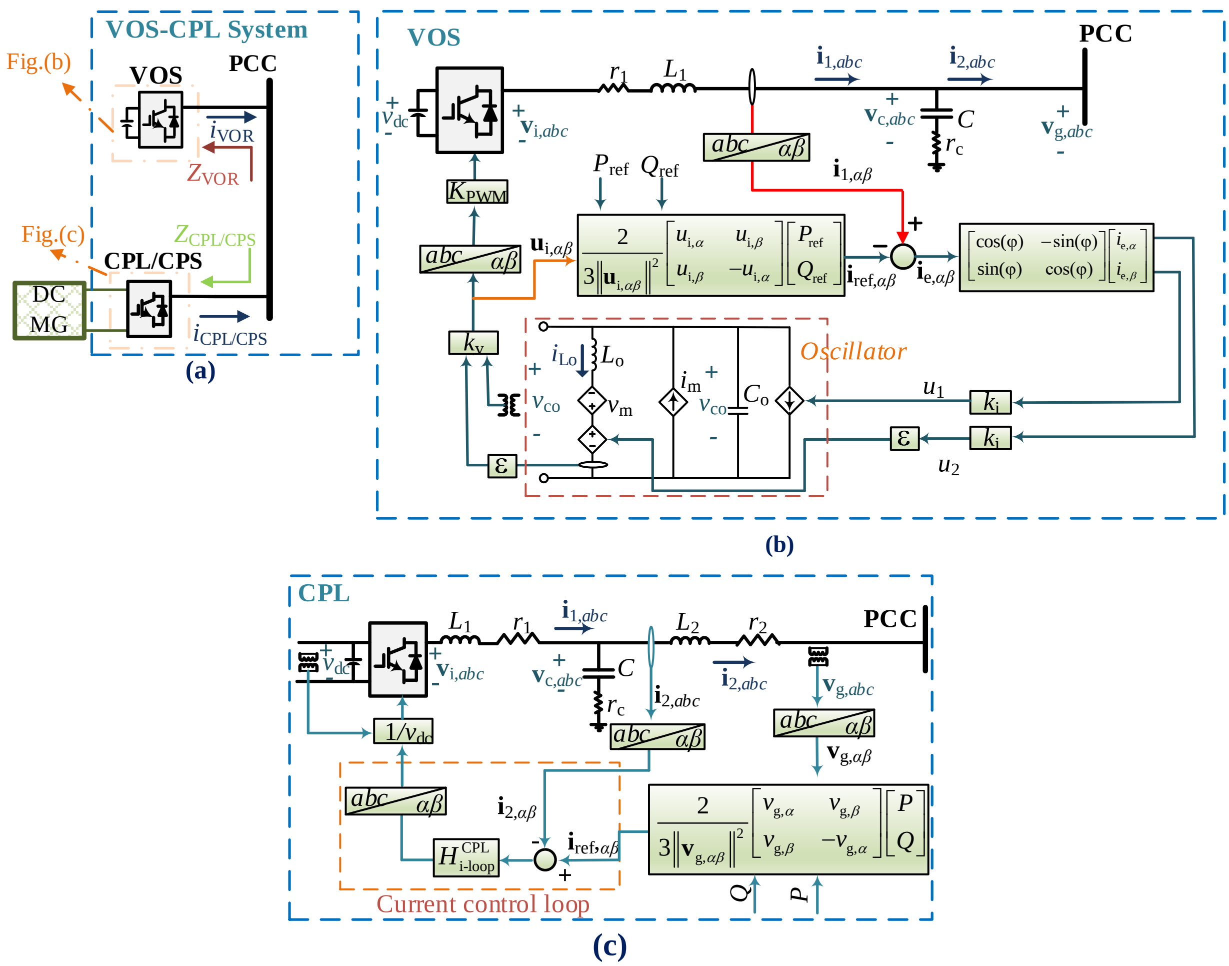

Figure 4-2 Considered AC system and its components: (a) high-level architecture of VOS-CPL system, (b) VOS and its control system, and (c) CPL and its control system.

Components	*Parameters & values*
CPL	L_1 =3mH, r_{L1}=0.1Ω, L_2 =1mH, r_{L2}=0.05Ω, C=30μF, r_c =0.25Ω
VOS	L_1 =3mH, r_1=0.1Ω, C=30μF, r_c=0.3Ω, S_{nom}=18kVA, V_{nom}=120V, $V_{min,p.u}$=0.95, ω_{nom}=120π rad/s, $\lvert\Delta\omega\rvert_{max}$=π rad/s, K_v=120, K_i=0.02, ζ=138.9/sV^2, τ=8ms, C_o=0.0289F, L_o=240 μH

Table 4.1 Parameters of CPL and VOS.

4.2.1 Small-Signal Modeling VOS-CPL System

For performing stability analysis, small-signal impedances are used. The small-signal impedance of CPL is developed in the previous chapter and will be used in the next subsection. The small-signal model of VOS is developed here. The state-space model of the oscillator shown in Figure 4-1 can be expressed as

$$\begin{bmatrix}\dot{v}_{\mathrm{i},\alpha}\\ \dot{v}_{\mathrm{i},\beta}\end{bmatrix} = \mathbf{A}_{\mathrm{o},\alpha\beta}\begin{bmatrix}v_{\mathrm{i},\alpha}\\ v_{\mathrm{i},\beta}\end{bmatrix} + \frac{k_{\mathrm{v}}k_i}{C_{\mathrm{o}}}\begin{bmatrix}i_\beta\\ -i_\alpha\end{bmatrix} + \frac{2k_{\mathrm{v}}k_i}{3C_{\mathrm{o}}\left\|\mathbf{v}_{\mathrm{i},\alpha\beta}\right\|^2}\begin{bmatrix}Q_{\mathrm{ref}} & -P_{\mathrm{ref}}\\ P_{\mathrm{ref}} & Q_{\mathrm{ref}}\end{bmatrix}\begin{bmatrix}v_{\mathrm{i},\alpha}\\ v_{\mathrm{i},\beta}\end{bmatrix},$$

$$\mathbf{A}_{\mathrm{o},\alpha\beta} = \begin{bmatrix}\frac{\zeta}{k_{\mathrm{v}}^2}(2V_{\mathrm{nom}}^2 - \left\|\mathbf{v}_{\mathrm{i},\alpha\beta}\right\|^2) & -\omega_{\mathrm{nom}}\\ \omega_{\mathrm{nom}} & \frac{\zeta}{k_{\mathrm{v}}^2}(2V_{\mathrm{nom}}^2 - \left\|\mathbf{v}_{\mathrm{i},\alpha\beta}\right\|^2)\end{bmatrix}. \quad \textbf{(4.5)}$$

This state-space model is non-linear and should be linearized around an operating point. To this aim, this model is first transferred to *dq* frame using park transformation

$$\mathbf{T} = \begin{bmatrix}\cos(\omega_1 t) & \sin(\omega_1 t)\\ -\sin(\omega_1 t) & \cos(\omega_1 t)\end{bmatrix}. \quad \textbf{(4.6)}$$

The transformed state-space model in *dq* frame can be expressed as

$$\begin{bmatrix}\dot{v}_{\mathrm{i},d}\\ \dot{v}_{\mathrm{i},q}\end{bmatrix} = \mathbf{A}_{\mathrm{o},dq}\begin{bmatrix}v_{\mathrm{i},d}\\ v_{\mathrm{i},q}\end{bmatrix} + \frac{k_{\mathrm{v}}k_{\mathrm{i}}}{C_{\mathrm{o}}}\begin{bmatrix}i_{1,q}\\ -i_{1,d}\end{bmatrix} + \frac{2k_{\mathrm{v}}k_{\mathrm{i}}}{3C_{\mathrm{o}}\left\|\mathbf{v}_{\mathrm{i},dq}\right\|^2}\begin{bmatrix}Q_{\mathrm{ref}} & -P_{\mathrm{ref}}\\ P_{\mathrm{ref}} & Q_{\mathrm{ref}}\end{bmatrix}\begin{bmatrix}v_{\mathrm{i},d}\\ v_{\mathrm{i},q}\end{bmatrix},$$

$$\mathbf{A}_{\mathrm{o},dq} = \begin{bmatrix}\frac{\zeta}{k_{\mathrm{v}}^2}(2V_{\mathrm{nom}}^2 - \left\|\mathbf{v}_{\mathrm{i},dq}\right\|^2) & -(\omega_{\mathrm{nom}} - \omega)\\ (\omega_{\mathrm{nom}} - \omega) & \frac{\zeta}{k_{\mathrm{v}}^2}(2V_{\mathrm{nom}}^2 - \left\|\mathbf{v}_{\mathrm{i},dq}\right\|^2)\end{bmatrix}. \quad \textbf{(4.7)}$$

After doing linearization, the linear state-space model is expressed in the form of

$$\begin{bmatrix}\dot{\hat{v}}_{\mathrm{i},d}\\ \dot{\hat{v}}_{\mathrm{i},q}\end{bmatrix}=\begin{bmatrix}h_{11} & h_{12}\\ h_{21} & h_{22}\end{bmatrix}\begin{bmatrix}\hat{v}_{\mathrm{i},d}\\ \hat{v}_{\mathrm{i},q}\end{bmatrix}+1.5K_2\begin{bmatrix}\hat{i}_{1,q}\\ -\hat{i}_{1,d}\end{bmatrix},\ K_1=\frac{\zeta}{k_{\mathrm{v}}^2},\ K_2=\frac{2k_{\mathrm{v}}k_{\mathrm{i}}}{3C_{\mathrm{o}}},$$

$$\begin{cases} h_{11}=K_1(2V_{\mathrm{nom}}^2-3\overline{v}_{\mathrm{i},d}^2-\overline{v}_{\mathrm{i},q}^2)-\dfrac{2K_2}{3\|\overline{\mathbf{v}}_{\mathrm{i},dq}\|^2}\left[-2\overline{v}_{\mathrm{i},d}\overline{v}_{\mathrm{i},q}P_{\mathrm{ref}}+(\overline{v}_{\mathrm{i},d}^2-\overline{v}_{\mathrm{i},q}^2)Q_{\mathrm{ref}}\right]\\ h_{12}=-2K_1\overline{v}_{\mathrm{i},d}\overline{v}_{\mathrm{i},q}-(\omega_{\mathrm{nom}}-\omega)-\dfrac{2K_2}{3\|\overline{\mathbf{v}}_{\mathrm{i},dq}\|^2}\left[(\overline{v}_{\mathrm{i},d}^2-\overline{v}_{\mathrm{i},q}^2)P_{\mathrm{ref}}+2\overline{v}_{\mathrm{i},d}\overline{v}_{\mathrm{i},q}Q_{\mathrm{ref}}\right]\\ h_{21}=(\omega_{\mathrm{nom}}-\omega)-2K_1\overline{v}_{\mathrm{i},d}\overline{v}_{\mathrm{i},q}+\dfrac{2K_2}{3\|\overline{\mathbf{v}}_{\mathrm{i},dq}\|^2}\left[(\overline{v}_{\mathrm{i},q}^2-\overline{v}_{\mathrm{i},d}^2)P_{\mathrm{ref}}-2\overline{v}_{\mathrm{i},d}\overline{v}_{\mathrm{i},q}Q_{\mathrm{ref}}\right]\\ h_{22}=K_1(2V_{\mathrm{nom}}^2-\overline{v}_{\mathrm{i},d}^2-3\overline{v}_{\mathrm{i},q}^2)+\dfrac{2K_2}{3\|\overline{\mathbf{v}}_{\mathrm{i},dq}\|^2}\left[-2\overline{v}_{\mathrm{i},d}\overline{v}_{\mathrm{i},q}P_{\mathrm{ref}}-(\overline{v}_{\mathrm{i},d}^2-\overline{v}_{\mathrm{i},q}^2)Q_{\mathrm{ref}}\right]\end{cases}, \quad \textbf{(4.8)}$$

where ω, $\overline{v}_{\mathrm{i},d}$ and $\overline{v}_{\mathrm{i},q}$ represent the steady-state angular frequency, and *dq* components of oscillator output voltage which are obtained from equation (4.2). Then, the combined state-space model of the VOS, including AC LC filter, can be expressed as

$$\dot{\hat{\mathbf{x}}}_{\mathrm{VOS}}=\mathbf{A}_{\mathrm{VOS}}\hat{\mathbf{x}}_{\mathrm{VOS}}+\mathbf{B}_{\mathrm{VOS}}\hat{\mathbf{i}}_{2,dq},\ \hat{\mathbf{x}}_{\mathrm{VOS}}=[\hat{\mathbf{v}}_{\mathrm{i},dq}\quad \hat{\mathbf{x}}_{\mathrm{LC},dq}]^{\mathrm{T}},$$

$$\mathbf{A}_{\mathrm{VOS}}=\begin{bmatrix}h_{11} & h_{12} & 0 & 1.5K_2 & 0 & 0\\ h_{21} & h_{22} & -1.5K_2 & 0 & 0 & 0\\ -a_{13} & 0 & a_{11} & \omega_1 & a_{13} & 0\\ 0 & -a_{13} & -\omega_1 & a_{11} & 0 & a_{13}\\ 0 & 0 & a_{31} & 0 & 0 & \omega_1\\ 0 & 0 & 0 & a_{31} & -\omega_1 & 0\end{bmatrix}, \quad \textbf{(4.9)}$$

$$\mathbf{B}_{\mathrm{VOS}}=\begin{bmatrix}0 & 0 & r_{\mathrm{c}}/L_1 & 0 & -1/C & 0\\ 0 & 0 & 0 & r_{\mathrm{c}}/L_1 & 0 & -1/C\end{bmatrix}^{\mathrm{T}}.$$

This linear state-space model can be used to derive impedances of VOS in *dq* frame. This impedance can be obtained by considering the following equations.

$$\mathbf{Z}_{\mathrm{VOS},dq}(s)=\begin{bmatrix} \dfrac{\hat{v}_{\mathrm{g},d}}{\hat{i}_{2,d}} & \dfrac{\hat{v}_{\mathrm{g},d}}{\hat{i}_{2,q}} \\ \dfrac{\hat{v}_{\mathrm{g},q}}{\hat{i}_{2,d}} & \dfrac{\hat{v}_{\mathrm{g},q}}{\hat{i}_{2,q}} \end{bmatrix}=\begin{bmatrix} z_{dd}(s) & z_{dq}(s) \\ z_{qd}(s) & z_{qq}(s) \end{bmatrix},\begin{cases} z_{dd}\rightarrow \mathbf{C}_{\mathbf{t}}=\begin{bmatrix}0 & 0 & r_{\mathrm{c}} & 0 & 1 & 0\end{bmatrix}, D_{\mathrm{t}}=\begin{bmatrix}r_{\mathrm{c}}\end{bmatrix}, \\ z_{dq}\rightarrow \mathbf{C}_{\mathbf{t}}=\begin{bmatrix}0 & 0 & r_{\mathrm{c}} & 0 & 1 & 0\end{bmatrix}, D_{\mathrm{t}}=\begin{bmatrix}0\end{bmatrix}, \\ z_{qd}\rightarrow \mathbf{C}_{\mathrm{t}}=\begin{bmatrix}0 & 0 & 0 & r_{\mathrm{c}} & 0 & 1\end{bmatrix}, D_{\mathrm{t}}=\begin{bmatrix}0\end{bmatrix}, \\ z_{qq}\rightarrow \mathbf{C}_{\mathbf{t}}=\begin{bmatrix}0 & 0 & 0 & r_{\mathrm{c}} & 0 & 1\end{bmatrix}, D_{\mathrm{t}}=\begin{bmatrix}r_{\mathrm{c}}\end{bmatrix}. \end{cases} \quad \textbf{(4.10)}$$

$\mathbf{Z}_{\mathrm{VOS},dq}(s)$ is a full impedance matrix, where each entry high-order transfer function obtained numerically. Since the small-signal impedance of CPL and VOS are available, we can perform stability analysis which is provided in the next subsection.

4.2.2 Stability Analysis of VOS-CPL System

Since the impedances of both CPL and VOS are in the same coordinate, we can directly investigate the stability of the considered VOS-CPL system in *dq* frame. We call this method a "Direct Approach" versus the unifying approach which was introduced in the previous chapter. In what follows, we perform stability analysis based on both direct and unifying approach and their results will be compared.

The stability of VOS-CPL can be investigated by obtaining the frequency responses of impedance ratio matrix. The impedance ratio matrices **G** and $\mathbf{G}_{dq}$ are defined as

$$\begin{aligned} &\mathbf{G}\ \ (s)=\mathbf{Z}^{\mathrm{c}}_{\mathrm{VOS},\alpha\beta}(s)\mathbf{Y}^{\mathrm{c}}_{\mathrm{CPL},\alpha\beta}(s), \\ &\mathbf{G}_{dq}(s)=\mathbf{Z}_{\mathrm{VOS},dq}(s)\mathbf{Y}_{\mathrm{CPL},dq}(s). \end{aligned} \quad \textbf{(4.11)}$$

where **G** is in complex *αβ* frame (by using the unifying approach) and $\mathbf{G}_{dq}$ is in *dq* frame. According to the impedance-based stability analysis, if an eigenvalue of impedance ratio matrices **G** or $\mathbf{G}_{dq}$ has a positive magnitude at a candidate frequency (gain margin is negative) instability happens in that candidate frequency.

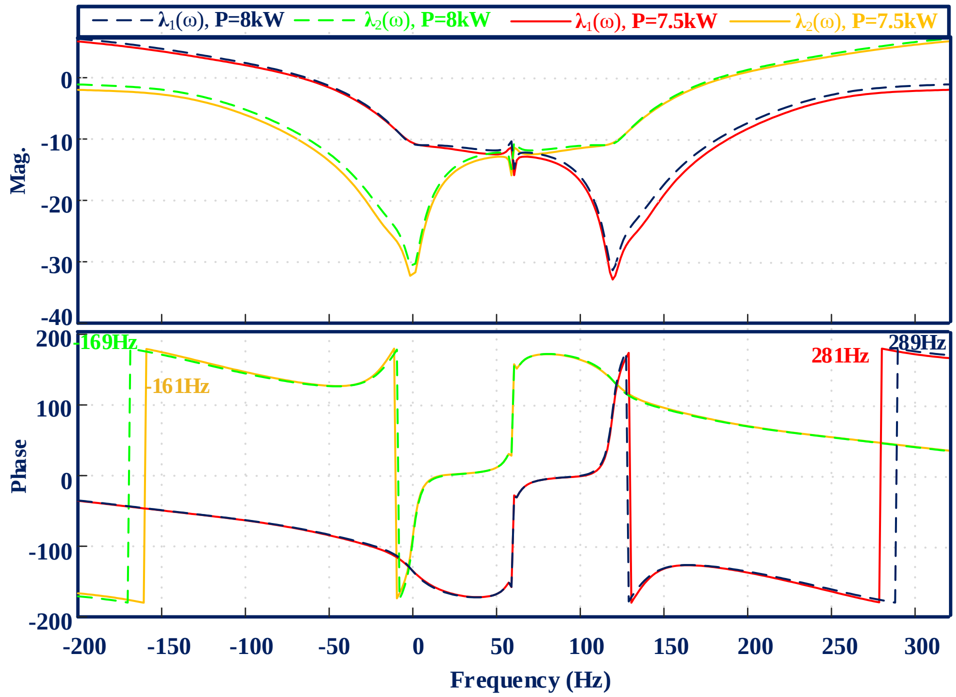

Figure 4-3 Frequency responses of eigenvalues of impedance ratio matrix G for VOS-CPL system when CPL power consumption is {P=7.5kW, Q=1kVar}, and {P=8kW, Q=1kVar}.

Figure 4-3 shows the frequency responses of eigenvalues of impedance ratio matrix **G** for two different power consumption profiles. In the first scenario, CPL is consuming active power P=7.5kW and reactive power Q=1kVar (solid lines), and in the second scenario it is consuming P= 8 kW, and the reactive power kept constant at Q=1kVar (dashed lines). It can be seen that for both operating points, there are some candidate frequencies for the instability of VOS-CPL system. However, at none of these candidate frequencies, the gain margin becomes negative, therefore the VOS-CPL system is stable in these two operating points.

Figure 4-4 depicts the frequency responses of impedance ratio matrix **G** for two operating points of CPL {P=8.5kW, Q=1kVar} and {P=9kW, Q=1kVar}. Similarly, for both operating points, there are some candidate frequencies. When CPL is working in the operating point {P=8.5kW, Q=1kVar}, the gain margins at all candidate frequencies (λ_2:-179Hz and λ_1:299Hz) have small positive values. However, when the CPL power consumption is increased to 9kW the gain margins at candidate frequencies λ_2:-190Hz and λ_1:310Hz become negative and the considered VOS-CPL system is destabilized.

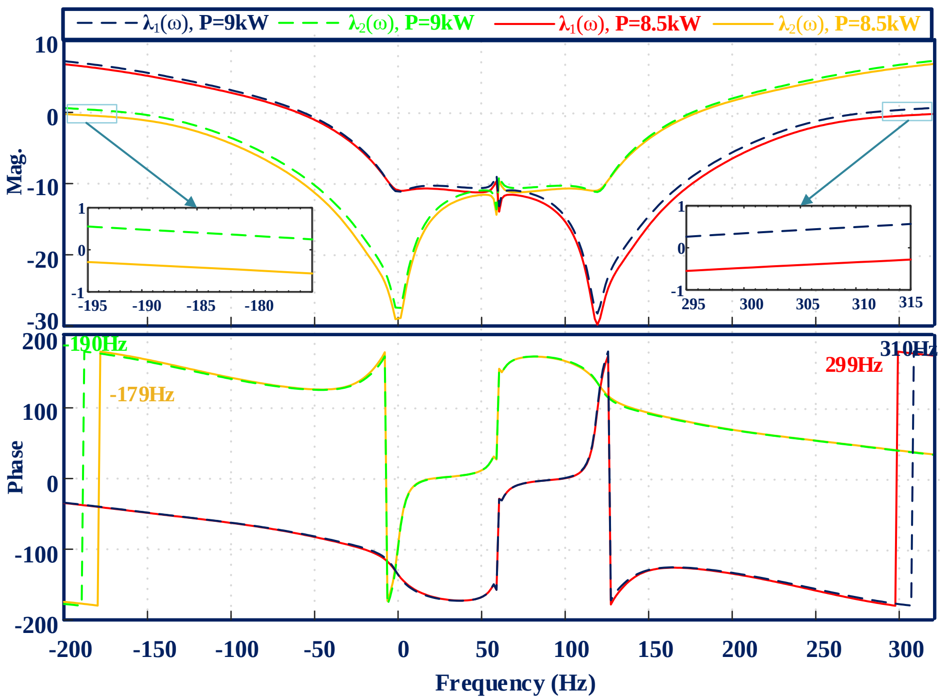

Figure 4-4 Frequency responses of eigenvalues of impedance ratio matrix G for VOS-CPL system when CPL power consumption is {P=8.5kW, Q=1kVar}, and {P=9kW, Q=1kVar}.

Figure 4-5 shows the frequency responses of eigenvalues of impedance ratio matrix $\mathbf{G}_{dq}$ for the two operating points of CPL {P=7kW, Q=1kVar} and {P=8kW, Q=1kVar}. It should be restated that the difference between impedance ratio matrices $\mathbf{G}_{dq}$ and **G** is in the way they are obtained. **G** represents the impedance ratio matrix in the complex $\alpha\beta$ frame after using the unifying approach.

$\mathbf{G}_{dq}$ represents the impedance ratio matrix which is directly obtained in *dq* frame. Similar to Figure 4-3, there are some candidate frequencies in Figure 4-5 and at none of them gain margin becomes negative. Comparing Figure 4-3 to Figure 4-5 it can be observed that the frequencies of candidate frequencies are different. This is because in *dq* frame all frequency components are shifted by nominal frequency 60Hz. In other words, if the candidate frequencies in Figure 4-5 are shifted 60 Hz back (to the right) the same candidate frequencies will be demonstrated in the stability analysis. Therefore, both stability analysis based direct approach or unifying approach have consistent findings.

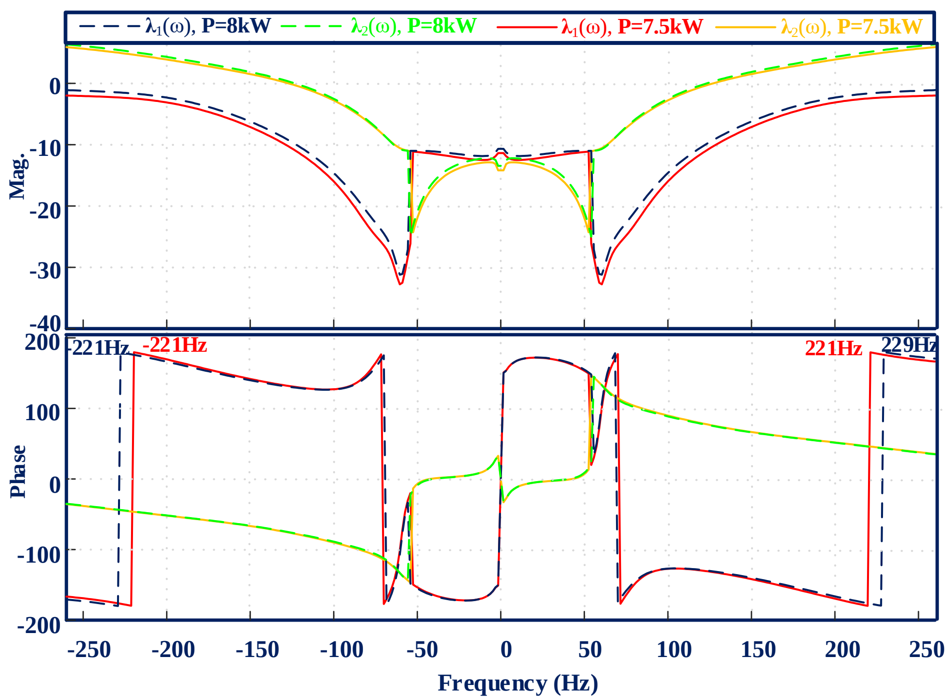

Figure 4-5 Frequency responses of eigenvalues of impedance ratio matrix $\mathbf{G}_{dq}$ for VOS-CPL system when CPL power consumption is {P=7.5kW, Q=1kVar}, and {P=8kW, Q=1kVar}.

Figure 4-6 shows the frequency responses of eigenvalues of impedance ratio matrix $\mathbf{G}_{dq}$ for the two operating points of CPL {P=8.5kW, Q=1kVar} and {P=9kW, Q=1kVar}. It shows that if the power consumption of CPL is increased to 9 kW the VOS-CPL system is destabilized. This finding is also shown in Figure 4-4. The Nyquist plots of eigenvalues of matrix $\mathbf{G}_{dq}$ are shown in Figure 4-7 for the two operating points of CPL {P=8.5kW, Q=1kVar} and {P=9kW, Q=1kVar}. It can be observed that when CPL power is increased to 9kW, the critical point (-1+0j) is encircled, and consequently, the system is destabilized.

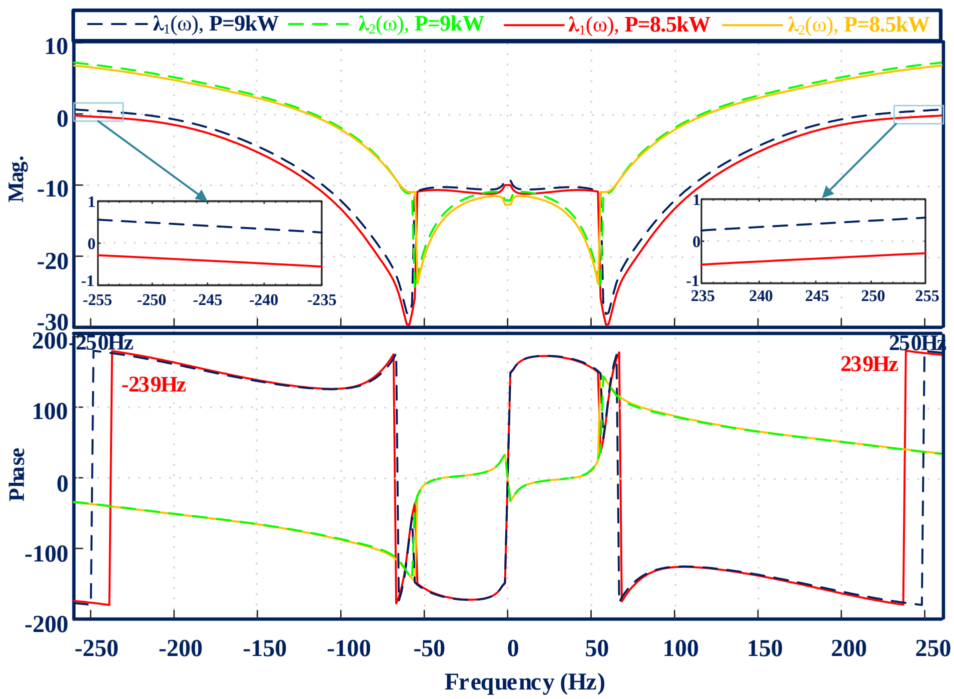

Figure 4-6 Frequency responses of eigenvalues of impedance ratio matrix G_{dq} for VOS-CPL system when CPL power consumption is {P=8.5kW, Q=1kVar}, and {P=9kW, Q=1kVar}.

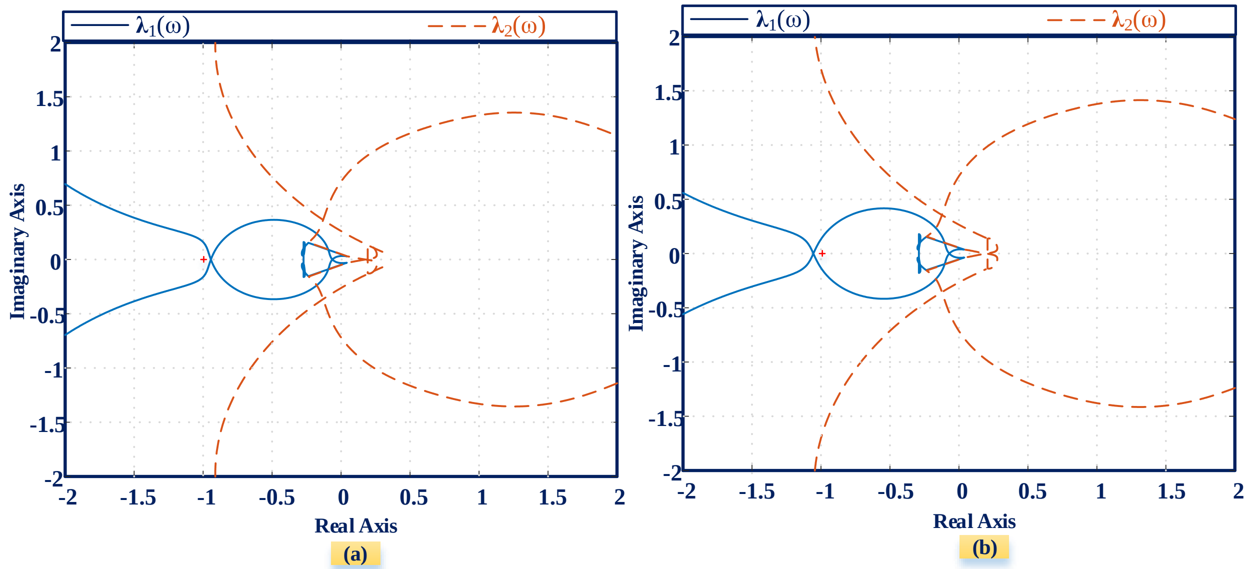

Figure 4-7 Nyquist plot of eigenvalues of matrix G for VOS-CPL system when: (a) CPL power consumption is {P=8.5kW, Q=1kVar}; and (b) CPL power consumption is {P=9kW, Q=1kVar}.

4.3 Simulation Studies

In this subsection, real-time simulation results are presented to validate the presented findings. Figure 4-8 shows the frequency responses of VOS impedance at the operating point {P=2kW, Q=0kVar} obtained with the developed models and frequency sweep analysis. It is observed that both approaches yield a consistent frequency response. Now, we can validate the stability analysis of the VOS-CPL system.

Figure 4-9 depicts the CPL power consumption profile for the VOS-CPL system, and the corresponding currents and voltages are shown in Figure 4-10. The system starts up with the CPL consuming active power P=2kW and reactive power Q=1kVar from the VOS. At *t*= 0.2s, the CPL active power is increased to P=6kW. Then, at *t*= 0.4s and *t*= 0.6s, the CPL active power demand is increased to 7.5kW and 8.5kW, respectively. In these two cases, larger oscillations are observed in the current and voltage, and yet the VOS-CPL system remains stable. As shown in the FFT analysis of the CPL current, the frequencies of oscillations are matching the candidate frequencies identified in Figure 4-4. Then, at t= 0.9s, the CPL active power is increased to P=9kW, and as predicted in Figure 4-4 and Figure 4-6, the VOS-CPL system becomes destabilized which is seen as fast-growing oscillations in Figure 4-9 and Figure 4-10.

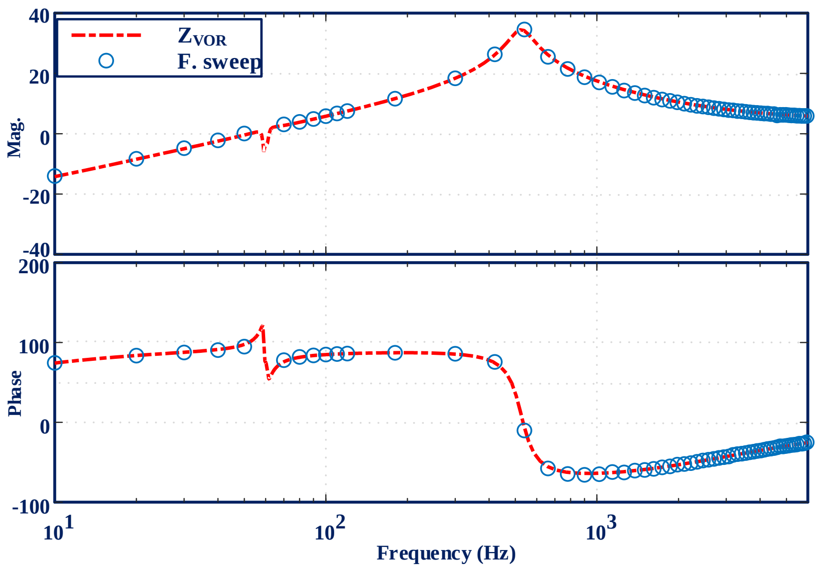

Figure 4-8 Frequency responses of VOS impedance.

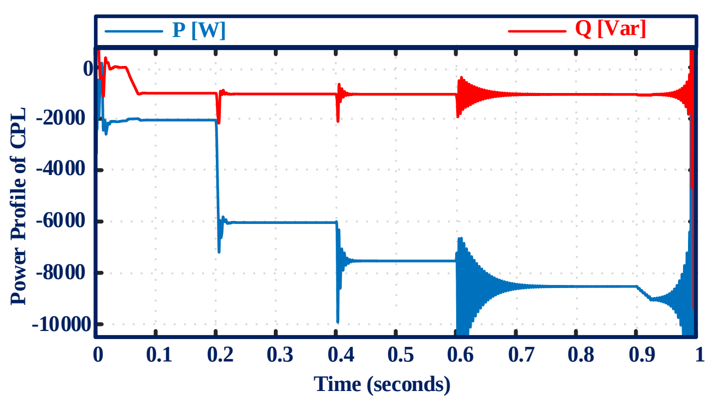

Figure 4-9 Active and reactive power consumption of CPL in VOS-CPL system.

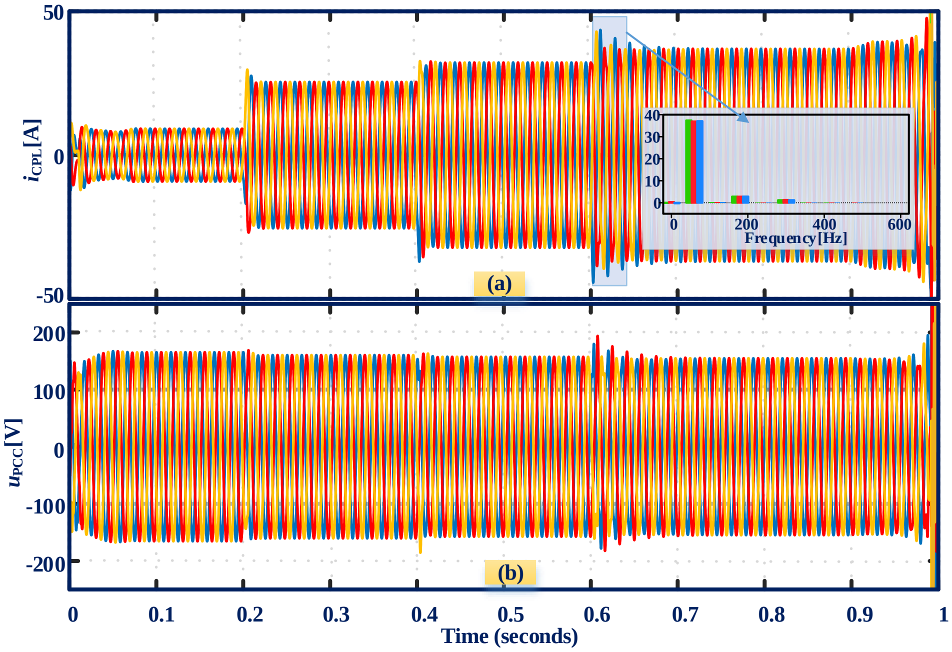

Figure 4-10 Voltage and current of CPL in VOS-CPL system: (a) current of CPL; and (b) voltage of CPL.

4.4 Summary

In this chapter, the design and operation of a virtual oscillator control scheme were discussed thoroughly. Moreover, the dynamic characteristic of this control scheme is assessed while feeding a constant power load. Two approaches for stability analysis, direct approach and unifying approach, were compared and it was shown that they yield consistent results. It was validated that as the power consumption of CPL increases, the dynamic behavior of this control scheme deteriorates.

Chapter 5: Stability Boundary Improvement

In the previous section, the stability of a CPL was investigated while it is supplied from three types of sources, AC grid, GCS, and VOS. It would be interesting to know if the stability boundaries of GCS-CPL system and VOS-CPL system can be further increased by manipulating the control schemes of the GCS and VOS.

5.1 Impedance Retuning of GCS

The closed-loop impedance of GCS is dependent on its control. A potential approach to reshape the GCS impedance is to consider a gain *K* in the outer voltage control loop of the GCS, which is shown in Figure 5-1. Changing the coefficient *K*, the closed-loop impedance of the GCS can be reshaped, as depicted in Figure 5-2. It can be seen that with increasing gain *K*, the impedance of GCS is made smaller. However, with increasing gain *K*, the crossover frequency of the voltage control loop is also increased, which is reported in Figure 5-3. To keep the crossover frequency around 800Hz, *K*=2 is selected here.

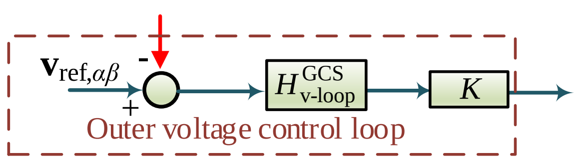

Figure 5-1. Modified control loop of GCS.

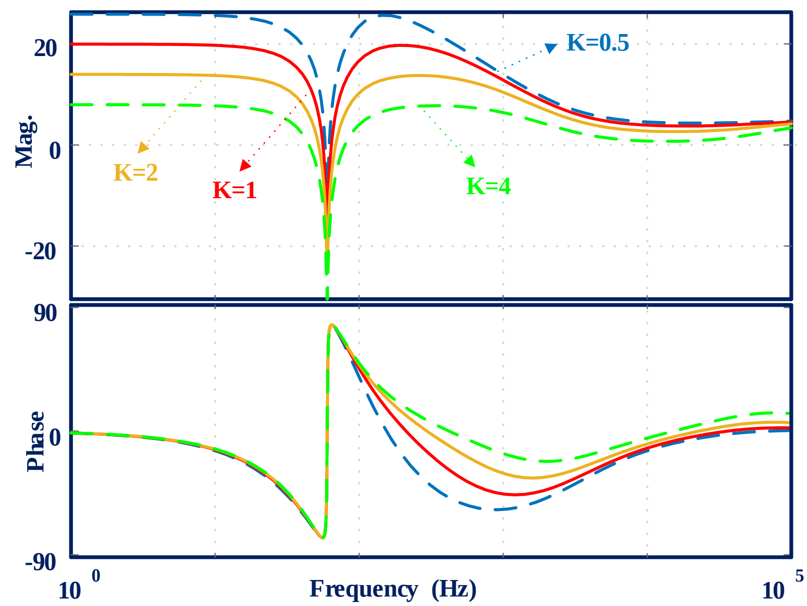

Figure 5-2. Impedance of GCS with different gain *K*.

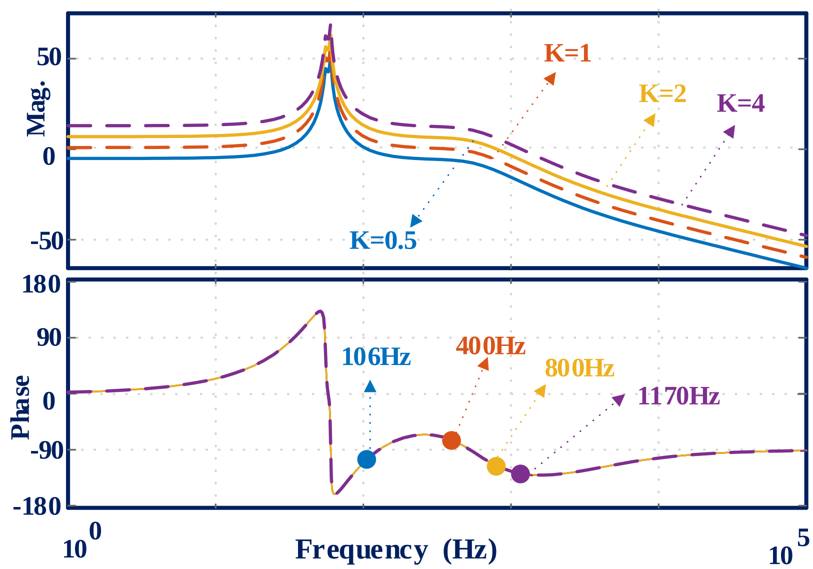

Figure 5-3. Frequency responses of the outer voltage control loop of GCS with different gain *K*.

5.2 Impedance Retuning of VOS

The impedance of VOS can also be reshaped by tuning its control parameters. The gain k_i can be changed to this aim. Figure 5-4 shows the impedance of the VOS with different values of k_i versus the impedance of the AC grid. It can be seen that with decreasing this coefficient the impedance of the VOS becomes close to the impedance of the AC grid. According to the design criteria presented in [26], k_i is selected from

$$k_i = 3\frac{V_{nom}}{S_{rated}}, \tag{5.1}$$

and decreasing it is equivalent to increasing the S_{rated}, which for an AC grid can be very high. Therefore, decreasing k_i would help to mimic the behavior of the AC grid.

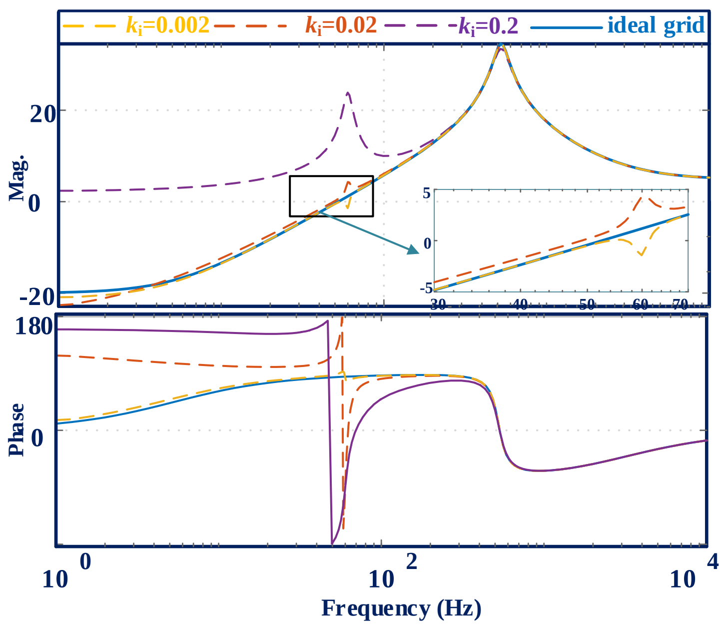

Figure 5-4. Impedances of AC grid and VOS with different values of K_i.

Ɛ is another parameter of VOS that can affect the shape of impedance. Figure 5-5 shows that with decreasing Ɛ the impedance of VOS becomes close to the impedance of the AC grid. The impedance can not be made smaller by decreasing Ɛ. Therefore, the effect of Ɛ on VOS impedance is similar to the effect of k_i, and the impedance of VOS is ultimately reshaped as the impedance of the AC grid.

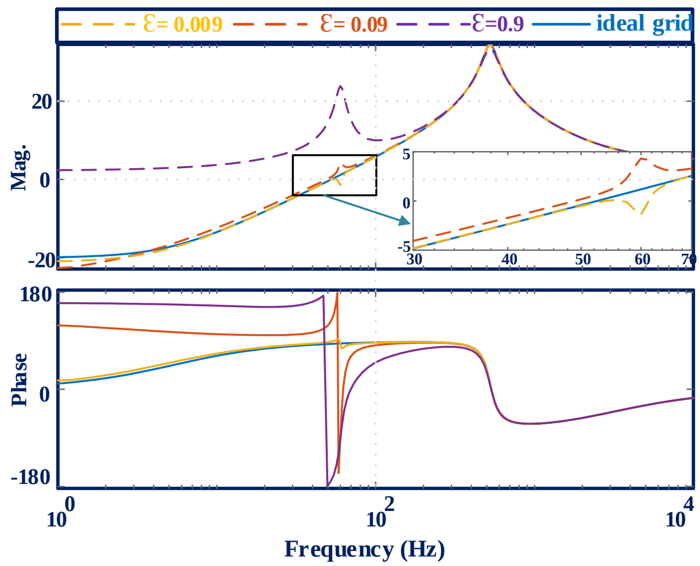

Figure 5-5. Impedances of AC grid and VOS with different values of Ɛ.

Another parameter in VOS is k_v, which can affect the steady-state output voltage. Increasing this gain, the output voltage of the VOS is increased, and when a CPL is connected to it, the CPL draws less current at a given operating point. This approach can help improve the stability of the VOS-CPL system slightly. This coefficient is then selected as the nominal voltage in [26]; however, it can be chosen as 1.05×nominal voltage as well.

5.3 Stability Analysis of GCS-CPL System with Retuned Parameters of GCS

Next, the dynamic behavior of the GCS-CPL system at three operating points defined as {P=13kW, Q=1kVar}, {P=13.5kW, Q=1kVar}, and {P=14kW, Q=1kVar} is analyzed. Figure 5-6 shows the frequency responses of eigenvalues of impedance ratio matrix **G**(s) in the GCS-CPL system with K=2. When the CPL is consuming real power of 13kW and 13.5kW, the gain margins at all candidate frequencies (as 210Hz, 108 Hz, 109Hz and -90 Hz) are positive, and therefore, the GCS-CPL system remains stable in these two operating points. However, when the CPL active power is increased to P=14kW, the gain margins at the candidate frequencies around 211Hz and -89Hz becomes negative, and the system is destabilized. Comparing Figure 5-6 and Figure 3-19, it can be observed that after the GCS's parameters have been tuned, the system's stability boundary has also been pushed to a higher power level.

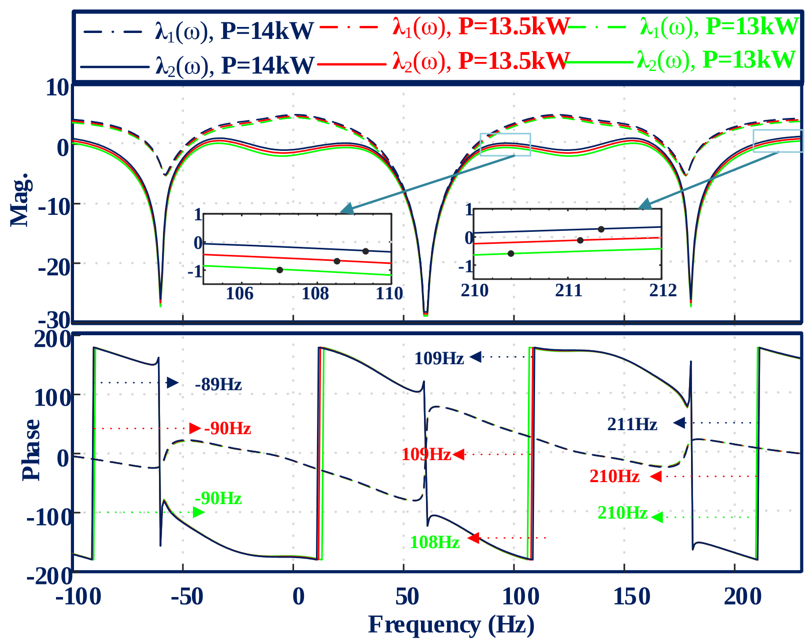

Figure 5-6 Frequency responses of eigenvalues of impedance ratio matrix G for the retuned GCS-CPL system when CPL power consumption is {P=13kW, Q=1kVar}, {P=13.5kW, Q=1kVar}, and {P=14kW, Q=1kVar}.

5.4 Stability Analysis of VOS-CPL System with Tuned Parameters of VOS

Figure 5-7 shows the frequency responses of eigenvalues of matrix **G**(s) for the VOS-CPL system with k_i=0.002, wherein three operating points are assumed: {P=9.5kW, Q=1kVar}, {P=10kW, Q=1kVar}, and {P=10.5kW, Q=1kVar}. When the CPL is consuming real power of 9.5kW and 10kW, the gain margins of eigenvalues at all candidate frequencies are positive. However, the gain margins at the candidate frequencies 311Hz and -191Hz becomes negative when the CPL active power is increased to P=10.5kW. In this case, the system is destabilized. Comparing Figure 5-7 and Figure 4-6, it can be seen that the tuned parameter k_i can successfully increase the stability boundary of the VOS-CPL system to a higher power level.

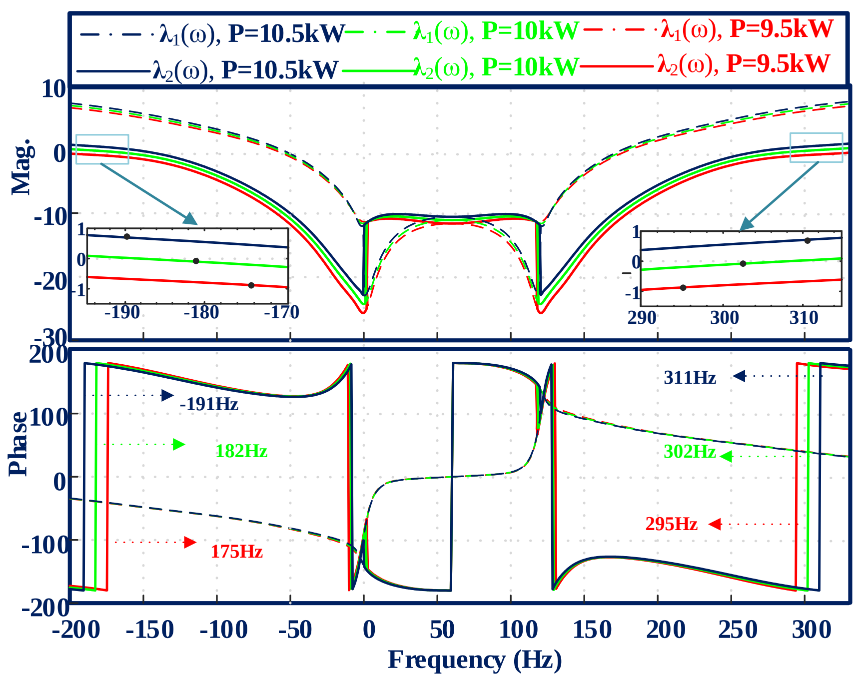

Figure 5-7. Frequency responses of eigenvalues of impedance ratio matrix G for retuned VOS-CPL system when CPL power consumption is {P=9.5kW, Q=1kVar}, {P=10kW, Q=1kVar}, and {P=10.5kW, Q=1kVar}.

5.5 Simulation Studies

5.5.1 GCS-CPL System with Retuned Parameters.

In this study, the gain K=2 is considered in the control system of GCS. Figure 5-8 shows the power profile of the CPL, and the corresponding currents and voltages are depicted in Figure 5-9. The system starts up with the CPL consuming P=7kW from the GCS. Then, at t= 0.2s and t= 0.4s, the CPL power is increased to P=10kW and P=12kW, respectively. At t= 0.6s, the CPL power is increased to P=13.5kW, and after some oscillations, the system still remains stable. However, when the CPL active power is increased further to P=14kW at t= 0.9s, the system becomes unstable following large and increasing oscillations of currents and voltages at the PCC bus where the CPL is connected. The FFT analysis of the CPL current also shows that the oscillations match the candidate frequencies as identified in Figure 5-6.

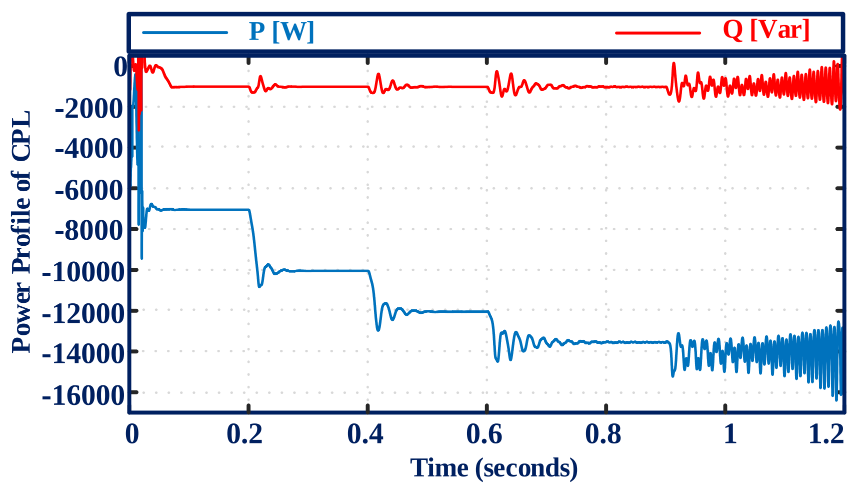

Figure 5-8. Active and reactive power consumption of CPL in GCS-CPL system with retuned parameters.

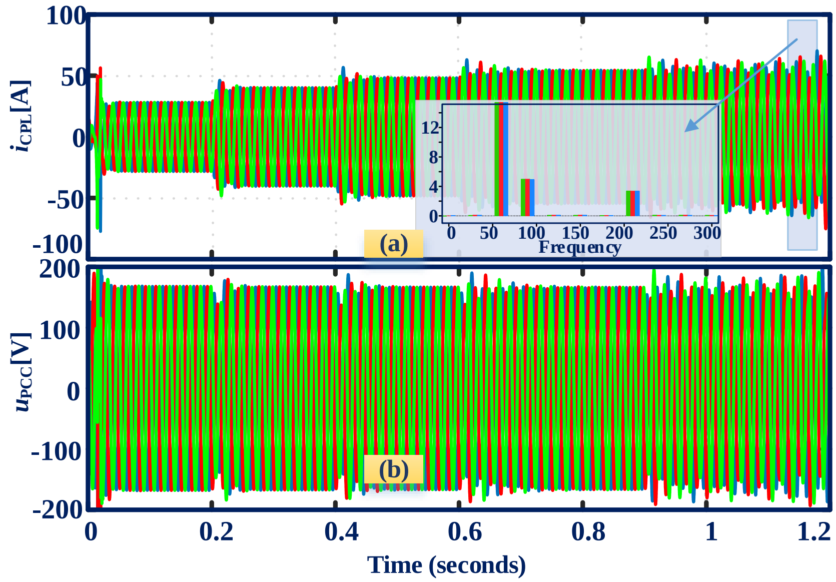

Figure 5-9. Voltage and current of CPL in GCS-CPL system with retuned parameters: (a) current of CPL; and (b) voltage of CPL.

5.5.2 VOS-CPL System with Retuned Parameters

In this study, the gain k_i=0.002 is considered in the control system of the VOS. The power profile of the CPL is depicted in Figure 5-10, and the corresponding currents and voltages are also shown in Figure 5-11. The system starts up with CPL consuming P=4.5kW from the VOS. Then, at times t= 0.2s, t= 0.4s, and t= 6s, the CPL power demand is sequentially increased. As predicted Figure 5-7, the dynamic behavior of the VOS-CPL system deteriorates with increasing the CPL power. Finally, the system becomes unstable at t= 0.9s, when the CPL power is increased to P=10.5kW. This is also consistent with the prediction made in Figure 5-7. The FFT analysis of the CPL current also verifies that the oscillation happens at the candidate frequencies predicted in Figure 5-7.

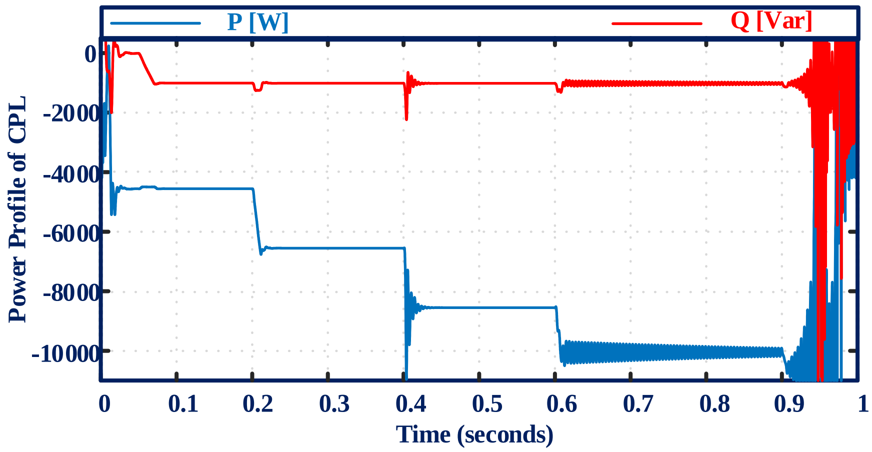

Figure 5-10. Active and reactive power consumption of CPL in VOS-CPL system with retuned parameters.

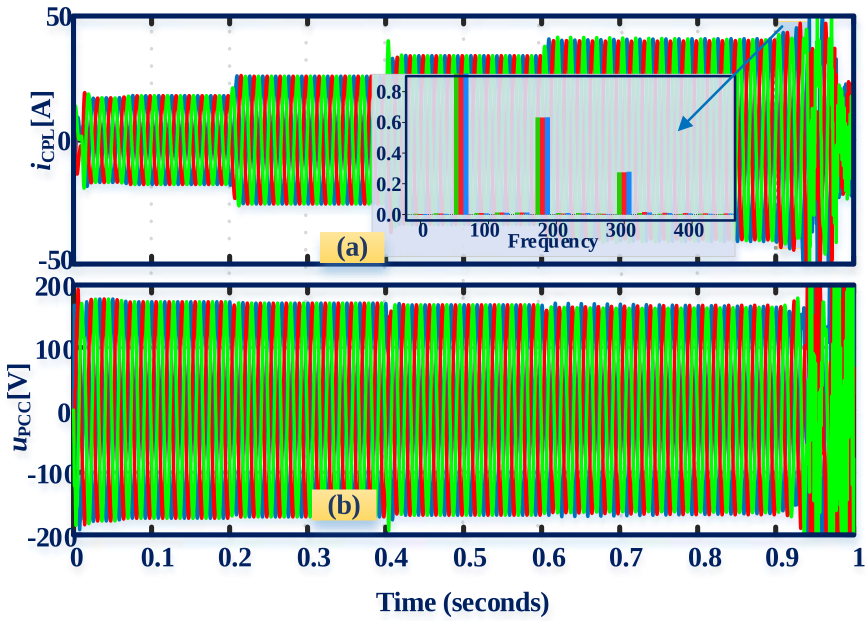

Figure 5-11. Voltage and current of CPL in VOS-CPL system with retuned parameters: (a) current of CPL; and (b) voltage of CPL.

5.6 Summary

In this chapter, the parameters in control schemes of VOS and GCS were retuned to shape their output impedance. By frequency- and time-domain analysis, it was shown that the stability boundary of GCS-CPL system and VOS-CPL system can be increased to a higher power level of CPL. The stability boundaries of these systems with first and retuned parameters are also reported in Figure 5-12.

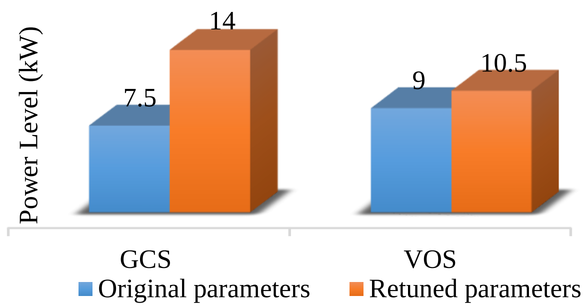

Figure 5-12. Stability boundaries of GCS-CPL and VOS-CPL systems with original and retuned parameters

Chapter 6: Summary and Future Work

6.1 Summary and contributions

This thesis is focused on improving the operation of AC microgrids, which may be composed of different energy resources and electronic loads. First, a hierarchical control scheme for the low voltage distribution system within the microgrid has been set forth, such that the distributed energy resources can be properly coordinated considering different level of time scales and economic objectives. The proposed scheme is based on solving a near real-time unit commitment problem, which represents and advantage and leads to minimization of the operational cost considering prices of different energy sources.

A broader scope of this thesis has been the dynamic stability of AC microgrids under the presence of electronically-interfaced energy resources and constant power loads. This thesis, for the first time, investigates the dynamic interactions between a virtual-oscillator controlled sources and CPL. This is achieved using small-signal models for VOS and CPL subsystems, and subsequently applying the impedance-based analysis and Nyquist criterion for determining the instability and oscillatory modes. As an alternative source, this investigation is also included an AC grid and a generic controller source (GSC). The presented methodology is demonstrated capable of precisely predicting the instability and sideband oscillations resulted from the interaction and increasing power level of the CPL. The thesis makes a contribution by providing a system-level insight into the operation of AC microgrids with VOSs and CPLs. The capability of impedance reshaping is assessed for different type of sources. The stability boundaries of AC microgrid are then extended to a higher power level of the CPL when the source impedance is taken into account for tuning the respective controllers.

It is also demonstrated that, while the VOS has a faster dynamic response compared to the GSC, their stability boundaries may be actually smaller.

6.2 Future Work

6.2.1 More accurate representation of DERs

In this thesis, for the sake of simplicity, it is assumed that the PWM process in power electronics does not have delays, the switching process does not have losses, dc-link voltage has negligible dynamics, etc. A natural continuation of the thesis can be about topics which aim to investigate the effects of non-ideal factors in power electronics on stability related issues in microgrids.

6.2.2 Microgrids with Complex Architecture

In this thesis, a simplified microgrid with one bus and balanced phases has been assumed. However, in practice, Microgrids can have fairly complicated distribution network with many busses and transformers, and can be highly imbalanced in terms of loads on individual phases. In such intricate microgrid architectures, stability problems may appear as interactions among multiple components and their fast controllers and network filters. The small-signal modeling technique and impedance-based stability analysis should be modified and extended to address the stability problems in these settings.

6.2.3 Modified Control Structure for VOSs

As demonstrated in chapter 5, VOSs with their conventional structure may be less flexible in terms of impedance tuning, and consequently, their stability boundaries can be limited when they are supplying CPLs. Therefore, it is envisioned that further modifications of the VOSs' control structure may be possible to improve their stability under the CPLs, which represents the subject for future research.

6.2.4 Online Impedance Identification and Tuning

The stability analysis based on the impedance requires a profound understanding of all components (and their parameters) within a microgrid. In practical cases, this knowledge may not be always possible since many parameters may change or be undetermined. Consequently, the stability analysis can not be performed accurately ahead of time. In such cases, methods based on machine learning algorithms as well as identification techniques may be used to accurately identify the impedance characteristics of components in real-time. Then, the identified impedances can be used to perform stability analysis, the result of which may be utilized to tune the controllers of various components on line and in real-time.

Bibliography

[1] G. M. Masters, "Renewable and efficient electric power systems, Second edition." John Wiley & Sons, Inc, 2013.

[2] J. J. Justo, F. Mwasilu, J. Lee, and J.-W. Jung, "AC-microgrids versus DC-microgrids with distributed energy resources: A review," *Renew. Sustain. Energy Rev.*, vol. 24, pp. 387–405, Aug. 2013, doi: 10.1016/j.rser.2013.03.067.

[3] M. Farrokhabadi *et al.*, "Microgrid Stability Definitions, Analysis, and Examples," *IEEE Trans. Power Syst.*, vol. 35, no. 1, pp. 13–29, 2020, doi: 10.1109/TPWRS.2019.2925703.

[4] H. Han, X. Hou, J. Yang, J. Wu, M. Su, and J. M. Guerrero, "Review of power sharing control strategies for islanding operation of AC microgrids," *IEEE Trans. Smart Grid*, vol. 7, no. 1, pp. 200–215, 2016, doi: 10.1109/TSG.2015.2434849.

[5] M. E. Kamalesh, M. Vikashini, and S. Pradeep, "Precompensated Master Slave Control of Parallel DC-DC Converter in DC-Microgrid," in *2018 International Conference on Current Trends towards Converging Technologies (ICCTCT)*, Mar. 2018, pp. 1–5, doi: 10.1109/ICCTCT.2018.8550994.

[6] T. Caldognetto and P. Tenti, "Microgrids Operation Based on Master–Slave Cooperative Control," *IEEE J. Emerg. Sel. Top. Power Electron.*, vol. 2, no. 4, pp. 1081–1088, Dec. 2014, doi: 10.1109/JESTPE.2014.2345052.

[7] S. Baek, Y. Cho, and T.-G. Koo, "Average Current Sharing Control Strategy for Parallel Operation of UPS with Low Bandwidth Communication," in *2019 IEEE Applied Power Electronics Conference and Exposition (APEC)*, Mar. 2019, pp. 2445–2451, doi: 10.1109/APEC.2019.8721793.

[8] A. M. Roslan, K. H. Ahmed, S. J. Finney, and B. W. Williams, "Improved Instantaneous Average Current-Sharing Control Scheme for Parallel-Connected Inverter Considering Line Impedance Impact in Microgrid Networks," *IEEE Trans. Power Electron.*, vol. 26, no. 3, pp. 702–716, Mar. 2011, doi: 10.1109/TPEL.2010.2102775.

[9] I. U. Nutkani, P. C. Loh, P. Wang, and F. Blaabjerg, "Linear Decentralized Power Sharing Schemes for Economic Operation of AC Microgrids," *IEEE Trans. Ind. Electron.*, vol. 63, no. 1, pp. 225–234, Jan. 2016, doi: 10.1109/TIE.2015.2472361.

[10] K. Wang, X. Huang, B. Fan, Q. Yang, G. Li, and M. L. Crow, "Decentralized Power Sharing Control for Parallel-Connected Inverters in Islanded Single-Phase Micro-Grids," *IEEE Trans. Smart Grid*, vol. 9, no. 6, pp. 6721–6730, Nov. 2018, doi: 10.1109/TSG.2017.2720683.

[11] M. Kosari and S. H. Hosseinian, “Decentralized Reactive Power Sharing and Frequency Restoration in Islanded Microgrid,” *IEEE Trans. Power Syst.*, vol. 32, no. 4, pp. 2901–2912, Jul. 2017, doi: 10.1109/TPWRS.2016.2621033.

[12] Y. Han, H. Li, P. Shen, E. A. A. Coelho, and J. M. Guerrero, “Review of Active and Reactive Power Sharing Strategies in Hierarchical Controlled Microgrids,” *IEEE Trans. Power Electron.*, vol. 32, no. 3, pp. 2427–2451, Mar. 2017, doi: 10.1109/TPEL.2016.2569597.

[13] R. Majumder, B. Chaudhuri, A. Ghosh, R. Majumder, G. Ledwich, and F. Zare, “Improvement of Stability and Load Sharing in an Autonomous Microgrid Using Supplementary Droop Control Loop,” *IEEE Trans. Power Syst.*, vol. 25, no. 2, pp. 796–808, May 2010, doi: 10.1109/TPWRS.2009.2032049.

[14] H. Han, Y. Liu, Y. Sun, M. Su, and J. M. Guerrero, “An Improved Droop Control Strategy for Reactive Power Sharing in Islanded Microgrid,” *IEEE Trans. Power Electron.*, vol. 30, no. 6, pp. 3133–3141, Jun. 2015, doi: 10.1109/TPEL.2014.2332181.

[15] M. H. Andishgar, E. Gholipour, and R. allah Hooshmand, “An overview of control approaches of inverter-based microgrids in islanding mode of operation,” *Renew. Sustain. Energy Rev.*, vol. 80, no. May, pp. 1043–1060, 2017, doi: 10.1016/j.rser.2017.05.267.

[16] P. Sreekumar and V. Khadkikar, “Nonlinear load sharing in low voltage microgrid using negative virtual harmonic impedance,” in *IECON 2015 - 41st Annual Conference of the IEEE Industrial Electronics Society*, Nov. 2015, pp. 003353–003358, doi: 10.1109/IECON.2015.7392617.

[17] P. Sreekumar and V. Khadkikar, “A New Virtual Harmonic Impedance Scheme for Harmonic Power Sharing in an Islanded Microgrid,” *IEEE Trans. Power Deliv.*, vol. 31, no. 3, pp. 936–945, Jun. 2016, doi: 10.1109/TPWRD.2015.2402434.

[18] K. De Brabandere, B. Bolsens, J. Van den Keybus, A. Woyte, J. Driesen, and R. Belmans, “A Voltage and Frequency Droop Control Method for Parallel Inverters,” *IEEE Trans. Power Electron.*, vol. 22, no. 4, pp. 1107–1115, Jul. 2007, doi: 10.1109/TPEL.2007.900456.

[19] S. Golestan, J. M. Guerrero, and J. C. Vasquez, “Three-Phase PLLs: A Review of Recent Advances,” *IEEE Trans. Power Electron.*, vol. 32, no. 3, pp. 1894–1907, Mar. 2017, doi: 10.1109/TPEL.2016.2565642.

[20] H. Yi, X. Wang, F. Blaabjerg, and F. Zhuo, “Impedance Analysis of SOGI-FLL-Based Grid Synchronization,” *IEEE Trans. Power Electron.*, vol. 32, no. 10, pp. 7409–7413, 2017, doi: 10.1109/TPEL.2017.2673866.

[21] S. V Dhople, B. B. Johnson, F. Dörfler, and A. O. Hamadeh, “Synchronization of Nonlinear Circuits in Dynamic Electrical Networks With General Topologies,” *IEEE Trans. Circuits*

Syst. I Regul. Pap., vol. 61, no. 9, pp. 2677–2690, 2014, doi: 10.1109/TCSI.2014.2332250.

[22] G. S. Seo, M. Colombino, I. Subotic, B. Johnson, D. Gros, and F. Dorfler, “Dispatchable virtual oscillator control for decentralized inverter-dominated power systems: Analysis and experiments,” in *Conference Proceedings - IEEE Applied Power Electronics Conference and Exposition - APEC*, 2019, vol. 2019-March, pp. 561–566, doi: 10.1109/APEC.2019.8722028.

[23] B. B. Johnson, S. V. Dhople, J. L. Cale, A. O. Hamadeh, and P. T. Krein, “Oscillator-based inverter control for islanded three-phase microgrids,” *IEEE J. Photovoltaics*, vol. 4, no. 1, pp. 387–395, 2014, doi: 10.1109/JPHOTOV.2013.2280953.

[24] B. B. Johnson, S. V. Dhople, A. O. Hamadeh, and P. T. Krein, “Synchronization of parallel single-phase inverters with virtual oscillator control,” *IEEE Trans. Power Electron.*, vol. 29, no. 11, pp. 6124–6138, 2014, doi: 10.1109/TPEL.2013.2296292.

[25] M. Lu, S. Dutta, V. Purba, S. Dhople, and B. Johnson, “A grid-compatible virtual oscillator controller: Analysis and design,” *2019 IEEE Energy Convers. Congr. Expo. ECCE 2019*, pp. 2643–2649, 2019, doi: 10.1109/ECCE.2019.8913128.

[26] J. M. Guerrero, J. C. Vasquez, J. Matas, L. G. De Vicuña, and M. Castilla, “Hierarchical control of droop-controlled AC and DC microgrids - A general approach toward standardization,” *IEEE Trans. Ind. Electron.*, vol. 58, no. 1, pp. 158–172, 2011, doi: 10.1109/TIE.2010.2066534.

[27] M. Hatti, A. Meharrar, and M. Tioursi, “Power management strategy in the alternative energy photovoltaic/PEM Fuel Cell hybrid system,” *Renew. Sustain. Energy Rev.*, vol. 15, no. 9, pp. 5104–5110, 2011, doi: https://doi.org/10.1016/j.rser.2011.07.046.

[28] J. A. P. Lopes, C. L. Moreira, and A. G. Madureira, “Defining Control Strategies for MicroGrids Islanded Operation,” *IEEE Trans. Power Syst.*, vol. 21, no. 2, pp. 916–924, May 2006, doi: 10.1109/TPWRS.2006.873018.

[29] M. Lu, Y. Yang, B. Johnson, and F. Blaabjerg, “An Interaction-Admittance Model for Multi-Inverter Grid-Connected Systems,” *IEEE Trans. Power Electron.*, vol. 34, no. 8, pp. 7542–7557, 2019, doi: 10.1109/TPEL.2018.2881139.

[30] Y. Liao and X. Wang, “Impedance-Based Stability Analysis for Interconnected Converter Systems with Open-Loop RHP Poles,” *IEEE Trans. Power Electron.*, vol. 35, no. 4, pp. 4388–4397, 2020, doi: 10.1109/TPEL.2019.2939636.

[31] X. Wang and F. Blaabjerg, “Harmonic Stability in Power Electronic-Based Power Systems: Concept, Modeling, and Analysis,” *IEEE Trans. Smart Grid*, vol. 10, no. 3, pp. 2858–2870, 2019, doi: 10.1109/TSG.2018.2812712.

[32] J. Sun, G. Wang, X. Du, and H. Wang, “A Theory for Harmonics Created by Resonance in Converter-Grid Systems,” *IEEE Trans. Power Electron.*, vol. 34, no. 4, pp. 3025–3029, 2019, doi: 10.1109/TPEL.2018.2869781.

[33] Z. Xin, P. C. Loh, X. Wang, F. Blaabjerg, and Y. Tang, “Highly Accurate Derivatives for LCL-Filtered Grid Converter with Capacitor Voltage Active Damping,” *IEEE Trans. Power Electron.*, vol. 31, no. 5, pp. 3612–3625, 2016, doi: 10.1109/TPEL.2015.2467313.

[34] X. Wang, F. Blaabjerg, and P. C. Loh, “Grid-current-feedback active damping for LCL resonance in grid-connected voltage-source converters,” *IEEE Trans. Power Electron.*, vol. 31, no. 1, pp. 213–223, 2016, doi: 10.1109/TPEL.2015.2411851.

[35] M. Lu, X. Wang, F. Blaabjerg, and P. C. Loh, “An analysis method for harmonic resonance and stability of multi-paralleled LCL-filtered inverters,” *2015 IEEE 6th Int. Symp. Power Electron. Distrib. Gener. Syst. PEDG 2015*, vol. 00, no. c, pp. 1–6, 2015, doi: 10.1109/PEDG.2015.7223086.

[36] L. Harnefors, R. Finger, X. Wang, H. Bai, and F. Blaabjerg, “VSC Input-Admittance Modeling and Analysis above the Nyquist Frequency for Passivity-Based Stability Assessment,” *IEEE Trans. Ind. Electron.*, vol. 64, no. 8, pp. 6362–6370, 2017, doi: 10.1109/TIE.2017.2677353.

[37] M. B. Delghavi and A. Yazdani, “An Adaptive Feedforward Compensation for Stability Enhancement in Droop-Controlled Inverter-Based Microgrids,” *IEEE Trans. Power Deliv.*, vol. 26, no. 3, pp. 1764–1773, Jul. 2011, doi: 10.1109/TPWRD.2011.2119497.

[38] J. Hu, Y. Huang, D. Wang, H. Yuan, and X. Yuan, “Modeling of Grid-Connected DFIG-Based Wind Turbines for DC-Link Voltage Stability Analysis,” *IEEE Trans. Sustain. Energy*, vol. 6, no. 4, pp. 1325–1336, Oct. 2015, doi: 10.1109/TSTE.2015.2432062.

[39] Y. Huang, X. Zhai, J. Hu, D. Liu, and C. Lin, “Modeling and Stability Analysis of VSC Internal Voltage in DC-Link Voltage Control Timescale,” *IEEE J. Emerg. Sel. Top. Power Electron.*, vol. 6, no. 1, pp. 16–28, Mar. 2018, doi: 10.1109/JESTPE.2017.2715224.

[40] H. Wu and X. Wang, “Design-Oriented Transient Stability Analysis of PLL-Synchronized Voltage-Source Converters,” *IEEE Trans. Power Electron.*, vol. 35, no. 4, pp. 3573–3589, 2020, doi: 10.1109/TPEL.2019.2937942.

[41] X. Wang, L. Harnefors, and F. Blaabjerg, “Unified Impedance Model of Grid-Connected Voltage-Source Converters,” *IEEE Trans. Power Electron.*, vol. 33, no. 2, pp. 1775–1787, 2018, doi: 10.1109/TPEL.2017.2684906.

[42] M. Cespedes, L. Xing, and J. Sun, “Constant-power load system stabilization by passive damping,” *IEEE Trans. Power Electron.*, vol. 26, no. 7, pp. 1832–1836, 2011, doi: 10.1109/TPEL.2011.2151880.

[43] K. Areerak, T. Sopapirm, S. Bozhko, C. I. Hill, A. Suyapan, and K. Areerak, “Adaptive Stabilization of Uncontrolled Rectifier Based AC–DC Power Systems Feeding Constant Power Loads,” *IEEE Trans. Power Electron.*, vol. 33, no. 10, pp. 8927–8935, Oct. 2018, doi: 10.1109/TPEL.2017.2779541.

[44] D. Yang, X. Wang, and F. Blaabjerg, “Sideband Harmonic Instability of Paralleled Inverters with Asynchronous Carriers,” *IEEE Trans. Power Electron.*, vol. 33, no. 6, pp. 4571–4577, 2018, doi: 10.1109/TPEL.2017.2731313.

[45] H. Wu, X. Wang, and L. Kocewiak, “Impedance-Based Stability Analysis of Voltage-Controlled MMCs Feeding Linear AC Systems,” *IEEE J. Emerg. Sel. Top. Power Electron.*, vol. 6777, no. c, pp. 1–1, 2020, doi: 10.1109/JESTPE.2019.2911654.

[46] H. Tao, H. Hu, X. Wang, F. Blaabjerg, and Z. He, “Impedance-Based Harmonic Instability Assessment in a Multiple Electric Trains and Traction Network Interaction System,” *IEEE Trans. Ind. Appl.*, vol. 54, no. 5, pp. 5083–5096, 2018, doi: 10.1109/TIA.2018.2793843.

[47] Y. A. R. I. Mohamed and A. A. Radwan, “Hierarchical control system for robust microgrid operation and seamless mode transfer in active distribution systems,” *IEEE Trans. Smart Grid*, vol. 2, no. 2, pp. 352–362, 2011, doi: 10.1109/TSG.2011.2136362.

[48] J. M. Guerrero, M. Chandorkar, T.-L. Lee, and P. C. Loh, “Advanced Control Architectures for Intelligent Microgrids—Part I: Decentralized and Hierarchical Control,” *IEEE Trans. Ind. Electron.*, vol. 60, no. 4, pp. 1254–1262, Apr. 2013, doi: 10.1109/TIE.2012.2194969.

[49] A. Bidram and A. Davoudi, “Hierarchical structure of microgrids control system,” *IEEE Trans. Smart Grid*, vol. 3, no. 4, pp. 1963–1976, 2012, doi: 10.1109/TSG.2012.2197425.

[50] Z. Li, C. Zang, P. Zeng, H. Yu, and S. Li, “Fully Distributed Hierarchical Control of Parallel Grid-Supporting Inverters in Islanded AC Microgrids,” *IEEE Trans. Ind. Informatics*, vol. 14, no. 2, pp. 679–690, Feb. 2018, doi: 10.1109/TII.2017.2749424.

[51] A. Emadi, A. Khaligh, C. H. Rivetta, and G. A. Williamson, “Constant Power Loads and Negative Impedance Instability in Automotive Systems: Definition, Modeling, Stability, and Control of Power Electronic Converters and Motor Drives,” *IEEE Trans. Veh. Technol.*, vol. 55, no. 4, pp. 1112–1125, Jul. 2006, doi: 10.1109/TVT.2006.877483.

[52] M. Jaksic *et al.*, “Nonlinear sideband effects in small-signal input dq admittance of six-pulse diode rectifiers,” in *2013 Twenty-Eighth Annual IEEE Applied Power Electronics Conference and Exposition (APEC)*, Mar. 2013, pp. 2761–2768, doi: 10.1109/APEC.2013.6520687.

[53] N. Bottrell, M. Prodanovic, and T. C. Green, “Dynamic Stability of a Microgrid With an Active Load,” *IEEE Trans. Power Electron.*, vol. 28, no. 11, pp. 5107–5119, Nov. 2013, doi: 10.1109/TPEL.2013.2241455.

[54] B. Wen, D. Boroyevich, R. Burgos, P. Mattavelli, and Z. Shen, “Small-Signal Stability Analysis of Three-Phase AC Systems in the Presence of Constant Power Loads Based on Measured d-q Frame Impedances,” *IEEE Trans. Power Electron.*, vol. 30, no. 10, pp. 5952–5963, Oct. 2015, doi: 10.1109/TPEL.2014.2378731.

[55] R. R. Karasani, V. B. Borghate, P. M. Meshram, H. M. Suryawanshi, and S. Sabyasachi, “A Three-Phase Hybrid Cascaded Modular Multilevel Inverter for Renewable Energy Environment,” *IEEE Trans. Power Electron.*, vol. 32, no. 2, pp. 1070–1087, Feb. 2017, doi: 10.1109/TPEL.2016.2542519.

[56] D. Vinnikov, A. Chub, E. Liivik, and I. Roasto, “High-Performance Quasi-Z-Source Series Resonant DC–DC Converter for Photovoltaic Module-Level Power Electronics Applications,” *IEEE Trans. Power Electron.*, vol. 32, no. 5, pp. 3634–3650, May 2017, doi: 10.1109/TPEL.2016.2591726.

[57] A. Reznik, M. G. Simoes, A. Al-Durra, and S. M. Muyeen, “LCL Filter Design and Performance Analysis for Grid-Interconnected Systems,” *IEEE Trans. Ind. Appl.*, vol. 50, no. 2, pp. 1225–1232, Mar. 2014, doi: 10.1109/TIA.2013.2274612.

[58] Hyeon-gyu Choi and Jung-Ik Ha, “Design technique of coupled inductor filter for suppressing switching ripples in PWM converters,” in *2015 6th International Conference on Power Electronics Systems and Applications (PESA)*, Dec. 2015, pp. 1–4, doi: 10.1109/PESA.2015.7398890.

[59] Jixuan Zheng, D. W. Gao, and Li Lin, “Smart Meters in Smart Grid: An Overview,” in *2013 IEEE Green Technologies Conference (GreenTech)*, Apr. 2013, pp. 57–64, doi: 10.1109/GreenTech.2013.17.

[60] R. C. D. and R. H. Bishop, *Modern control systems(12)*. 2001.

[61] S. Silwal and M. Karimi-Ghartemani, “On the design of proportional resonant controllers for single-phase grid-connected inverters,” *IEEE Int. Conf. Control Autom. ICCA*, vol. 2016-July, pp. 797–803, 2016, doi: 10.1109/ICCA.2016.7505376.

[62] R. Teodorescu, F. Blaabjerg, M. Liserre, and P. C. Loh, “Proportional-resonant controllers and filters for grid-connected voltage-source converters,” *IEE Proc. - Electr. Power Appl.*, vol. 153, no. 5, p. 750, 2006, doi: 10.1049/ip-epa:20060008.

[63] X. Wang, Y. W. Li, F. Blaabjerg, and P. C. Loh, “Virtual-Impedance-Based Control for Voltage-Source and Current-Source Converters,” *IEEE Trans. Power Electron.*, vol. 30, no. 12, pp. 7019–7037, 2015, doi: 10.1109/TPEL.2014.2382565.

[64] X. Wang, F. Blaabjerg, and P. C. Loh, “Passivity-Based Stability Analysis and Damping Injection for Multiparalleled VSCs with LCL Filters,” *IEEE Trans. Power Electron.*, vol. 32, no. 11, pp. 8922–8935, 2017, doi: 10.1109/TPEL.2017.2651948.

[65] A. M. Rahimi, G. A. Williamson, and A. Emadi, “Loop-Cancellation Technique: A Novel Nonlinear Feedback to Overcome the Destabilizing Effect of Constant-Power Loads,” *IEEE Trans. Veh. Technol.*, vol. 59, no. 2, pp. 650–661, Feb. 2010, doi: 10.1109/TVT.2009.2037429.

[66] J. Sun, “Impedance-based stability criterion for grid-connected inverters,” *IEEE Trans. Power Electron.*, 2011, doi: 10.1109/TPEL.2011.2136439.